博士論文

Reliable GPS-Free Vehicle Localization for V2X Systems

— A Study across Blockage, High-Mobility, and Multi-User Conditions

(V2X システムにおける GPS 非依存型の信頼性の高い車両測位— 遮蔽環境・高速移動・多ユーザ条件における検討)

Hu Dou

Abstract

Accurate vehicle localization and velocity estimation is a fundamental requirement for intelligent transportation systems, autonomous mobility, and safety-critical Vehicle to Everything (V2X) communication. However, achieving reliable positioning in realistic vehicular environments remains challenging, as signal propagation continuously transitions between line-of-sight (LoS) and non-line-of-sight (NLoS) conditions, while Doppler dynamics, fast mobility, and multipath fading disrupt classical localization strategies. To address these challenges, this dissertation presents a unified and channel-adaptive localization framework that maintains reliable positioning performance across heterogeneous V2X scenarios.

For LoS environments, a low-complexity 2D MUltiple SIgnal Classification (MUSIC)-based direction-of-arrival estimator is developed to extract azimuth and elevation information from mmWave antenna arrays. The estimated angles are fused with kinematic motion states using an Unscented Kalman Filter (UKF), enabling continuous trajectory estimation with high temporal stability and robustness against measurement noise. This module demonstrates centimeter-level accuracy while significantly reducing computational overhead compared with exhaustive spectral search-based approaches.

When LoS paths disappear and angle-based localization becomes unreliable, the framework transitions to a sensing strategy built on Orthogonal Time-Frequency Space (OTFS) modulation. A reconfigurable intelligent surface (RIS) is incorporated to reconstruct controllable propagation paths and enhance channel observability in NLoS conditions. A structured delay-Doppler processing and velocity estimation method are further designed to ensure delay, Doppler, and channel coefficient resolvability under high mobility and sparse multipath conditions.

The final stage extends the methodology to multi-user environments. An interference-aware iterative SIC-based page-style method is introduced to separate overlapping user signals. Furthermore, we also give the idea for adopting different MUSIC algorithms under different Signal-Noise Ratio (SNR) between an adaptive Forward–Backward Spatial Smoothing （FBSS） and Root-MUSIC-enhanced estimator, the method dynamically selects processing modes based on

interference level and snapshot quality. This enables scalable localization without sacrificing precision under dense vehicular access.

Comprehensive simulations confirm the effectiveness of the proposed system under different mobility levels, SNR conditions, antenna geometries, waveform configurations, and user densities. Results demonstrate that the framework achieves sub-degree (Degree of arrvival) DoA estimation accuracy in LoS conditions, maintains reliable localization performance under severe NLoS environments with RIS assistance, and supports multi-user coexistence with predictable computational complexity.

Overall, this dissertation presents a scalable, robust, and environment-adaptive localization framework that bridges classical array-signal processing, OTFS waveform design, and RIS-assisted channel engineering. The proposed methodology serves as a promising foundation for next-generation autonomous mobility, cooperative perception, and future V2X communication systems.

Keywords: Vehicle localization; MUSIC; RIS; OTFS; DoA estimation; UKF

Contents

Chapter 1 Introduction 1
1.1 Research Background 1
1.2 Objectives of This Research 3
1.3 Assumed System and Deployment Scenario 4
1.4 Organization of This Thesis 5

Chapter 2 Background and Related Work 7
2.1 Channel Angle Estimation Adoption 7
2.2 Kalman filter Application 9
2.3 Reconfigurable Intelligent Surface（RIS）and Orthogonal Time Frequency Space （OTFS） 10
2.4 Related Studies for Multiple vehicles Scenario and Peak-Average-Power-Ratio (PAPR) Analysis 11
2.5 Adaptive MUSIC Algorithm 13

Chapter 3 LoS-Based DoA Estimation and Vehicle Tracking 15
3.1 Overview of the Proposed LoS Localization Framework 15
3.2 Reference Signal Design and System Workflow 18
3.3 MIMO Channel Modeling and Spatial Covariance Construction 19
3.4 ALC2D-MUSIC Algorithm-based DoA Estimation 21
3.5 Proposed UKF-Based Vehicle State Estimation 25
3.5.1 Unscented Kalman filter Method 25
3.6 Numerical Results for LoS Scenario 28
3.6.1 MUSIC Algorithm Part Analysis 29
3.6.2 Unscented Kalman Filter Simulation 34
3.6.3 Complexity Analysis 38

Chapter 4 RIS-Assisted OTFS-Based Robust Localization in NLoS Environments 39
4.1 Overview of the Proposed NLoS Localization Framework 39
4.1.1 Contributions 40
4.2 System and Channel Model 42
4.2.1 System Description 42
4.2.2 General Process Model in OTFS under RIS 44
4.2.3 RIS Configuration 47
4.3 Channel Estimation Method 48
4.3.1 OTFS Variant Design 48
4.3.2 Initial Channel Angle Estimation 49
4.3.3 Reduced-PAPR Channel Estimation 51
4.3.4 UKF-Based Velocity Position Estimation and Beam Tracking 54
4.3.5 Robust Velocity Estimation Method 57
4.4 Evaluation of the Proposed Method 2: RIS-Assisted OTFS under NLoS 59
4.4.1 OTFS Performance 61
4.4.2 Result in MUSIC Algorithm 63
4.4.3 Result in low PAPR Estimation Method 63
4.4.4 Result in UKF Tracking 66
4.4.5 Robust Velocity Estimation Method Reliability 70
4.4.6 Complexity Analysis of Channel Estimation 70

Chapter 5 Multi-User Scenario Extension and System Unification 73
5.1 Multi-User OTFS Channel Modeling 73
5.1.1 Main Introduction 73
5.1.2 Methods 74
5.1.3 Basic Assumptions 74
5.1.4 Channel Estimation Model 75
5.1.5 Iterative Successive Interference Cancellation Detection 77
5.2 Adaptive DoA Estimation Based on FBSS/Root-MUSIC 78
5.3 System Model 78
5.3.1 Description 78
5.3.2 Vehicle Acceleration Model 78
5.3.3 Array Signal Model with Interference 79
5.3.4 Tracking with Unscented Kalman Filter (UKF) 81
5.4 Results for Page-style 84

5.4.1 Complexity 85
5.5 Results for Adaptive MUSIC Framework 90

Chapter 6 Conclusion and Future Work 95
6.1 Conclusion 95
6.2 Future Work 96

Publications 99

Acknowledgment 101

References 103

List of Figures

1.1 Motivation of the scenarios. 2

3.1 The LoS System overview. 16
3.2 Overview of the proposed method in LoS environment. 19
3.3 Illustration of the reference signal transmission. 21
3.4 The conventional MUSIC algorithm in a 2D searching mode. 22
3.5 Azimuth estimation analysis using MUSIC and the compressive sensing algorithm under different antenna configurations. 30
3.6 Elevation estimation analysis using MUSIC and the compressive sensing algorithm under different antenna configurations. 30
3.7 Azimuth estimation under different SNRs and searching scales using the MUSIC and compressive sensing algorithms. 31
3.8 Elevation estimation under different SNRs and searching scales using the MUSIC and compressive sensing algorithms. 31
3.9 Illustration of the vehicle movement scenario. 32
3.10 Position estimation under acceleration and curved trajectory during 200 time slots. 32
3.11 Position estimation error of the proposed method. 33
3.12 Vehicle trajectory under different channel propagation scenarios. 33
3.13 Position estimation error under different channel propagation scenarios. 34
3.14 Elevation estimation performance under different antenna array sizes. 34
3.15 Boxplot of estimation error under different Kalman filter iteration numbers. . . . 35
3.16 Estimation sensitivity under different UKF parameters α and β. 35
3.17 Positioning performance under different noise levels. 36
3.18 Computational complexity of the proposed algorithm compared with benchmark schemes. 36

4.1 Framework of the NLoS scenario. 43

4.2 Flowchart of the NLoS process. 44
4.3 Different OTFS variant design (ZP, CP, RZP, RCP). 50
4.4 BER performance under different variant. 60
4.5 BER performance for different padding lengths using several variant methods (SNR = 15 dB). 60
4.6 BER performance for different padding lengths using several variant methods (SNR = 10 dB). 61
4.7 The BER comparison with FULL matrix OFDM and ZP-OTFS when the velocity is 200 km/h. 61
4.8 The MUSIC algorithm to get the elevation and azimuth in different paths from the vehicle. 63
4.9 BER performance for different SNR among different OTFS modulation. 64
4.10 NMSE under different SNR among different OTFS modulation. 64
4.11 Spectral efficiency for different SNR among different OTFS modulation. 65
4.12 Cumulative probability of the PAPR for different OTFS schemes. 65
4.13 Localization performance in the straight driving scenario. (a) estimation error, (b) reconstructed trajectory. 66
4.14 The AoA estimation in a straight scenario. 66
4.15 Localization performance in the curved driving scenario. (a) estimation error, (b) reconstructed trajectory. 67
4.16 The AoA estimation in curve scenario. 67
4.17 The error in different antenna scale of RIS. 67
4.18 The trajectory in different antenna scale of RIS. 68
4.19 The CRLB analysis of the position and AoAs. 68
4.20 System accuracy. 69

5.1 The framework of the page-style system 74
5.2 The adaptive music framework. 78
5.3 BER performance under different values of β for different users. 85
5.4 BER performance under different vehicle velocities. 85
5.5 PAPR comparison between the proposed method and benchmark scheme EP. . . 86
5.6 Spectral efficiency comparison with benchmark schemes. 86
5.7 BER simulation result for the 4-user scenario. 87
5.8 LAdd parameter comparison. 87

5.9 Theoretical runtime under different numbers of users K and guard interval lengths l_{add}. 89
5.10 Measured computational complexity under different numbers of users K and guard interval lengths l_{add}. 89
5.11 MUSIC RMSE without noise under different SNR. 91
5.12 BSS-MUSIC DoA RMSE vs. SNR for Different Array Sizes. 92
5.13 MUSIC NMSE without (0-T/2) and with noise (T/2-T). 92
5.14 The trajectory under different scheme. 93
5.15 The trajectory error under different scheme. 93

List of Tables

1.1 List of Acronyms and Abbreviations 5

3.1 Summary of Notations for the LoS model. 17
3.2 Simulation parameters. 29
3.3 The 9 kinds of Noise level 37
3.4 The complexity of the MUSIC algorithm. 38

4.1 Summary of Notations in NLoS scenario. 41
4.2 List of abbreviations used in the NLoS part 42
4.3 Simulation parameters for NLoS Scenario. 62

5.1 The Page style Simulation parameters. 84
5.2 Simulation parameters for adaptive MUSIC scenario. 90

Chapter 1

Introduction

1.1 Research Background

With the rapid evolution of smart mobility and intelligent transportation systems (ITS), Vehicle-to-Everything (V2X) communication has become a fundamental enabler for autonomous driving and cooperative transportation. Emerging V2X applications—including cooperative perception, high-definition map sharing, sensor data exchange, collective decision-making, and coordinated maneuvering—require not only ultra-reliable connectivity but also very high data rates to support the real-time transmission of rich sensing information such as LiDAR point clouds, camera streams, and multi-vehicle state information. These stringent data-rate demands go far beyond the capabilities of legacy vehicular communication systems and motivate the adoption of advanced wireless technologies [1].

Fig. 1.1 illustrates the motivation of this work. In GPS-denied V2X scenarios, conventional localization methods such as vision/LiDAR and dead reckoning either suffer from high cost and fragility or accumulate errors over time. In contrast, wireless communication channels inherently contain spatial and temporal information, including angle, delay, and Doppler, which are directly related to vehicle position and velocity. Motivated by this insight, this work investigates a GPS-free vehicular localization framework that reuses communication signals as localization sensors, enabling robust positioning under blockage and high mobility.

To meet these requirements, millimeter-wave (mmWave) communication has emerged as a key enabling technology for next-generation V2X systems. By exploiting large bandwidths available at mmWave frequencies, V2X links can achieve gigabit-per-second data rates, supporting bandwidth-intensive applications and low-latency information exchange. In addition, the use of large antenna arrays at mmWave frequencies enables highly directional beamforming, which improves spectral efficiency and interference management in dense vehicular environments. As a

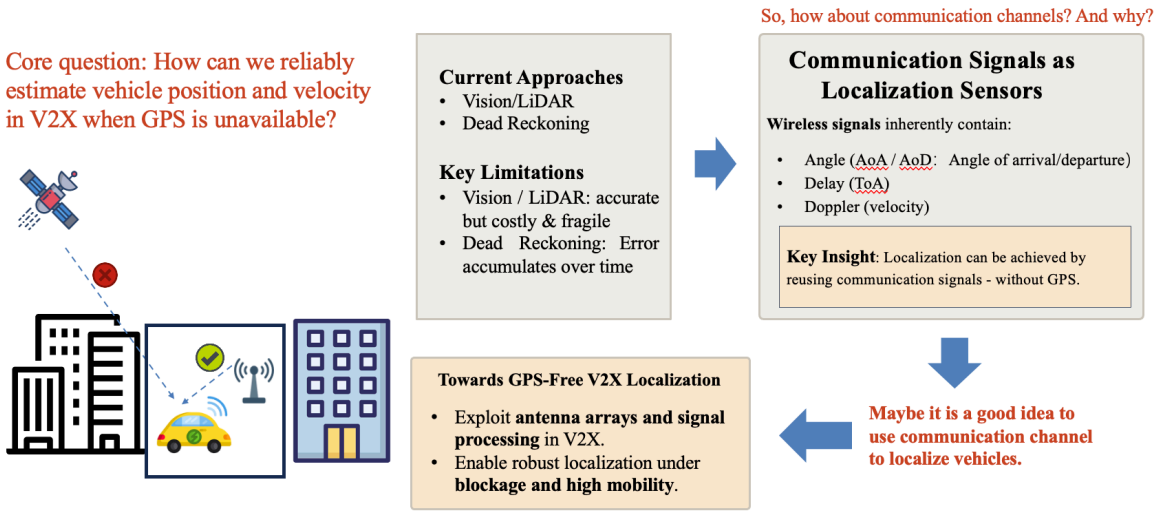


Fig.1.1: Motivation of the scenarios.

result, mmWave communication is widely regarded as a cornerstone of future V2X and Internet of Vehicles (IoV) architectures [2].

However, the adoption of mmWave communication also introduces a new set of challenges that fundamentally differentiate it from conventional sub-6 GHz systems. mmWave links are highly sensitive to blockage, beam misalignment, and rapid channel variations caused by vehicle mobility. Maintaining reliable connectivity therefore requires precise beam alignment and frequent beam tracking, both of which critically depend on accurate knowledge of vehicle position and motion. Consequently, accurate and robust positioning becomes not merely an auxiliary function, but a key enabler for sustaining high-rate mmWave V2X communication.

In this context, localization and communication become deeply intertwined. Conventional Global Positioning System (GPS)–based solutions, which typically provide meter-level accuracy, are insufficient for mmWave beam management and fail to meet the stringent reliability requirements in urban canyons, tunnels, or densely built environments. Sensor-based localization methods relying on LiDAR, radar, or vision can offer high accuracy, but they incur high deployment costs, substantial computational overhead, and sensitivity to adverse weather and environmental changes. These limitations motivate the exploration of communication-driven positioning, where localization information is extracted directly from wireless signals.

From a physical-layer perspective, mmWave communication channels inherently carry rich spatial and temporal information, including Angle of Arrival (AoA), Angle of Departure (AoD), delay, and Doppler shifts. These parameters are closely related to vehicle geometry and motion, making mmWave systems naturally suitable for integrated sensing and communication (ISAC).

By reusing communication signals for positioning and tracking, ISAC-based approaches can provide scalable and infrastructure-assisted localization without requiring additional on-board sensing hardware. [3]

Despite this potential, communication-based vehicular localization faces several unresolved challenges. High mobility induces severe Doppler spread and channel non-stationarity, which limits the effectiveness of conventional orthogonal frequency-division multiplexing (OFDM) waveforms. Non-Line-of-Sight (NLoS) propagation further degrades angular observability, while multi-user interference becomes inevitable in dense V2X deployments. These factors significantly complicate reliable position estimation based solely on instantaneous channel measurements.

To address these challenges, reconfigurable intelligent surfaces (RIS) and Orthogonal Time Frequency Space (OTFS) modulation have recently attracted increasing attention. RIS can actively reshape the propagation environment by creating controllable reflection paths, effectively reconstructing virtual Line-of-Sight (LoS) components in blocked scenarios. OTFS modulation, on the other hand, operates in the delay–Doppler domain and preserves channel structure under high mobility, enabling robust sensing and parameter extraction in rapidly time-varying channels. Together, RIS-assisted OTFS provides a promising foundation for robust vehicular localization in challenging propagation environments.

Building upon these observations, this dissertation investigates a channel-driven, GPS-free vehicular localization framework designed to operate reliably across Line-of-Sight (LoS), NLoS, and multi-user V2X scenarios. The proposed approach leverages mmWave antenna arrays for spatial sensing, adopts MUSIC-based angle estimation as the core measurement mechanism, integrates Unscented Kalman Filtering (UKF) for motion-aware state tracking, and extends naturally to RIS-assisted OTFS-based sensing under NLoS conditions. Through this unified design, the thesis aims to demonstrate how accurate positioning can be achieved as an integral component of future high-rate mmWave V2X and ISAC systems, rather than as an isolated subsystem. [4]

1.2 Objectives of This Research

The objective of this research is to establish an intelligent and scalable vehicular localization framework that integrates antenna-array signal processing, Reconfigurable Intelligent Surfaces (RIS), and Orthogonal Time Frequency Space (OTFS) modulation. To accomplish this, the thesis focuses on three complementary aspects:

- **LoS baseline:** Establish the core localization framework by employing a low-complexity

2D MUSIC algorithm to obtain high-precision DoA estimates, and fuse them with vehicle motion dynamics using an Unscented Kalman Filter (UKF) to enable stable and continuous trajectory tracking. Through these studies, the thesis aims to provide a reliable, low-cost, and communication-integrated localization solution applicable to future large-scale V2X networks. [5]

- **NLoS enhancement:** Extend the MUSIC+UKF framework to blockage environments by integrating RIS-assisted OTFS modulation and a low-PAPR pilot structure, enabling reliable delay–Doppler feature extraction and reconfigurable propagation paths for robust positioning under high mobility. Also propose a new algorithm to fuse two source of velocities to get more accurate results[6].
- **Extension:** Further generalize the framework for dense V2X deployment by introducing iterative interference cancellation and an adaptive MUSIC configuration. And also propose an idea that dynamically switches between conventional MUSIC, FBSS, and Root-MUSIC according to the SNR and interference level, while preserving UKF-based state estimation[7].

1.3 Assumed System and Deployment Scenario

To maintain consistency across modeling, algorithm design, and performance evaluation, this thesis adopts the following unified deployment assumptions:

1. **Intersection-Based Road Model:**
   The target environment is a vehicular communication hotspot centered around a road intersection. This scenario captures realistic vehicle motion patterns and dynamic geometry changes common in V2X deployments.
2. **NLoS Blockage and RIS-Assisted Propagation:**
   In NLoS conditions, surrounding buildings obstruct the direct propagation path between the vehicle and the base station (BS). To compensate for the blocked LoS link, a reconfigurable intelligent surface (RIS) is strategically placed to reconstruct a controllable reflective path and ensure reliable signal sensing under OTFS modulation.
3. **Antenna-Enabled Infrastructure and Vehicles:**
   Both the vehicle and the BS are assumed to be equipped with antenna arrays. This configuration enables high-resolution signal processing, including MUSIC-based direction estimation and communication-assisted localization leveraging channel features such as angle, delay, and Doppler.

Table1.1: List of Acronyms and Abbreviations

Acronym	Full Name	Acronym	Full Name
AoA	Angle of Arrival	MMSE	Minimum Mean Square Error
AoD	Angle of Departure	MUSIC	Multiple Signal Classification
AWGN	Additive White Gaussian Noise	NLoS	Non-Line-of-Sight
BER	Bit Error Rate	OFDM	Orthogonal Frequency Division Multiplexing
BS	Base Station	OTFS	Orthogonal Time Frequency Space
CE	Channel Estimation	PAPR	Peak-to-Average Power Ratio
CP	Cyclic Prefix	QAM	Quadrature Amplitude Modulation
CRLB	Cramér–Rao Lower Bound	RIS	Reconfigurable Intelligent Surface
CSI	Channel State Information	SE	Spectral Efficiency
DD	Delay–Doppler	SINR	Signal-to-Interference-plus-Noise Ratio
DFT	Discrete Fourier Transform	SNR	Signal-to-Noise Ratio
DoA	Direction of Arrival	UKF	Unscented Kalman Filter
EKF	Extended Kalman Filter	UE	User Equipment
FFT	Fast Fourier Transform	V2I	Vehicle-to-Infrastructure
ICI	Inter-Carrier Interference	V2V	Vehicle-to-Vehicle
IRS	Intelligent Reflecting Surface	V2X	Vehicle-to-Everything
KF	Kalman Filter	ZF	Zero Forcing
LoS	Line-of-Sight	ZP	Zero Padding

These scenario assumptions provide a realistic and scalable foundation for evaluating the proposed localization framework across LoS, NLoS, and multi-user communication conditions.

1.4 Organization of This Thesis

This thesis consists of seven chapters and two appendices, including the present chapter. The structure is as follows:

- **Chapter 1** describes the position and motivation of this thesis.
- **Chapter 2** provides an overview of the related research and the technical background of this work.
- **Chapter 3** presents the proposed localization and tracking architecture in LoS scenarios based on 2D-MUSIC and UKF.
- **Chapter 4** introduces the RIS-assisted OTFS-based localization method designed for NLoS high-mobility environments.
- **Chapter 5** extends the proposed framework to multi-user scenarios and evaluates the scalability and robustness of the system.
- **Chapter 6** summarizes the conclusions of the thesis and future research directions.

For ease of reading, a list of acronyms and abbreviations used throughout this paper is summarized in Table 1.1.

Chapter 2

Background and Related Work

This chapter reviews prior studies that are closely related to the key components of the proposed localization framework. Since this work builds upon angle-domain sensing, mobility-aware filtering, and delay–Doppler domain signal design, the related literature is organized into three main categories: MUSIC-based angle estimation and channel sensing, Kalman filter-based tracking and state estimation, and OTFS-based modulation and sensing techniques.

First, representative studies on direction or angle estimation are reviewed, with an emphasis on their applicability to vehicular and mmWave communication scenarios. Second, existing works employing Kalman filtering techniques for motion tracking, localization, and state estimation are discussed, highlighting their role in fusing noisy measurements with vehicle dynamics. next, recent advances in OTFS modulation and its extensions for high-mobility communication and sensing are summarized, providing the background for the RIS-assisted OTFS-based localization framework developed in this dissertation. And finally we also give some comparison in some extended aspects.

2.1 Channel Angle Estimation Adoption

Before reviewing channel and angle estimation techniques, it is important to clarify the rationale for adopting angle-domain estimation as the starting point of the proposed localization framework, rather than performing explicit position estimation directly.

Although direct positioning methods appear to provide a more straightforward solution, they typically require either dense infrastructure deployment, accurate synchronization among multiple anchors, or detailed environmental knowledge such as digital maps. In contrast, angle-of-arrival (AoA) and direction-of-arrival (DoA) estimation can be obtained from a single base station or roadside unit equipped with antenna arrays, making them more suitable for mmWave V2X sce-

narios with limited infrastructure support.

Moreover, angle-domain information provides a geometry-aware and measurement-level representation that can be naturally fused with vehicle motion models through sequential filtering techniques such as the Kalman filter. By first estimating AoA/DoA and then performing state estimation, the localization problem is decomposed into a sensing stage and a tracking stage, which improves robustness against noise, multipath effects, and intermittent observations.

Finally, beamforming-based MUSIC methods offer a favorable trade-off between angular resolution and computational complexity, and they form a common foundation for both LoS-based localization and more advanced extensions, such as RIS-assisted and multi-user scenarios. For these reasons, this dissertation begins with beamforming-based DoA/AoA estimation as the fundamental building block for the subsequent localization framework.

Dong-Jin et al. [8] proposed a beam-space MUSIC method, and in the method, the architecture is thoroughly studied by applying to outputs of the beams which are formed in different angles. Li et al. [9] proposed a 2D BMODE algorithm that calculates the desired angles armed with an iteration process. In addition, Vasanthan et al. [10] proposed a fair comparison between different strategies including MUSIC and other DoA estimation methods. Goto et al. [11] proposed a low-complexity 2D MUSIC algorithm, which greatly decreases the calculation time by separating the estimation process of azimuth and elevation DoAs. In [12], Ziyu et al. proposed an idea about a new mmWave channel estimation scheme that demonstrates mmWave networks armed with the beamspace MUSIC algorithm. In [13], Huan-Tang et al. proposed a Blind AoA estimation with the assistance of the MUSIC algorithm. In our work, we propose a low-complexity MUSIC algorithm under MIMO scenario and use it for the subsequent positional tracking process in Kalman filter. These existing studies have laid the foundation for our algorithm design, especially in terms of complexity reduction, mmWave channel applicability, and integration with positioning systems, and have directly inspired the formulation of our proposed MUSIC+UKF framework.

Many research studies focus on adoption based on channel estimation. The work in [14, 15, 16] proposed a compressed sensing (CS) method in channel parameter estimation. The authors in [17, 18, 19] used beam tracking to detect the position of objects. Jussi et al. [16] used a realistic state space method to track path parameters, and the extended Kalman filter was applied for better computation. Mike Koivisto et al. [17] showed a method to position a mobile device like a smartphone. Arash et al. [18] proposed a tracking position and orientation method under a heuristic beam selection framework. Additionally, the authors in [20], Anna et al. gave the idea of a localization and communication framework. Under the analysis of cramer-rao bounds in MIMO and direct localization, they get the position accurately. Arash et al. [1] derived a two-state algorithm for positioning under the line-of-sight and non-line-of-sight. On the other hand, they

also analyzed the Cramer-Rao bound. Elizaveta et al. [21] consider Kalman filter-based beam selection and positioning framework. In [22], Sanjay et al. propose an idea in channel estimation based on an UKF and federated learning. Xu et al. combined computer vision and beamforming to complete the beam alignment and inter-vehicle communication [23]. In [24], Li et al. used a deep-learning-based Kalman filter method to construct an unmanned aerial vehicle network to detect the velocity of the trains. Du et al.in [25] showed a framework of a longer pilot signal for better vehicle detection. In [26], Muddassar et al. proposed a beam tracking method based on deep recurrent variational autoencoders. These works collectively inspired the design of our proposed framework by demonstrating the feasibility and effectiveness of beam tracking, channel-aware positioning, and learning-based signal processing. Our approach builds upon these foundations by integrating low-complexity DoA estimation with a UKF-based tracking system, aiming for accurate, real-time vehicular localization under mmWave conditions.

2.2 Kalman filter Application

The Kalman filter in beam tracking is also widely applied in many aspects. As one of the mainstream technologies in beam tracking, Kalman filter is widely used for positioning and velocity detection in beam tracking. There are multitudinous technique methods to aid the detection such as channel parameter estimation, unmanned aerial vehicle (UAV)-aided and directly use Kalman filter. The authors in [27, 28, 29] adopt UAV to support the beam tracking technology, Seungseok et al. [27] adapted an UKF to construct the NR MIMO system, and use UAV to improve the data capacity. Dohyun et al. [28] proposed beam management using an extended Kalman filter (EKF) under UAV-assisted communication. Ha et al. [29], used an EKF idea under a UAV network to complete the beam tracking. In [30], the authors use channel estimation to boost the positioning, Mike et al. propose a 2-state Kalman filter to complete the velocity detection and positioning, however, how to match multiple vehicles to their corresponding signals and the velocity variation are not considered. Besides, there is also some research [3, 31, 32, 33, 34, 35, 36, 37] directly making use of the Kalman filter to help the beam tracking. In [3], Fan Liu et al. use an extended Kalman filter to predict the velocities and locations in a particular segment of roads, which is a little difficult to extend to another road scenario. The authors, Kun et al. proposed a Compressed Sensing Aided-Kalman filter method [31] to find a balance in the accuracy of estimation and alignment overhead. In [32], Seong et al. show an idea for vehicle tracking with an extended Kalman filter under state and acceleration models for the vehicles. Stephen G. Larew et al. [33], and Zhu et al. [34] constructed a beam tracking method armed with an UKF under mmWave networks. Liu et al. [35] and Li Chen et al. in [36] show an extended Kalman filter-based beam tracking

in millimeter wave MIMO systems, considering AoA, AoD and spatial information. Suhanya et al. [37] showed an architecture of robust beamforming also armed with extended Kalman filter. These studies demonstrate the wide applicability of Kalman filtering in beam tracking and vehicular positioning. Inspired by these works, our study adopts a UKF-based framework and introduces a MUSIC-assisted DoA estimation idea, aiming to improve robustness and estimation accuracy under high-mobility and multipath scenarios. The integration of low-complexity DoA estimation with UKF sets our approach apart from prior work, particularly in scenarios with rapidly changing dynamics and real-time constraints.

2.3 Reconfigurable Intelligent Surface（RIS）and Orthogonal Time Frequency Space（OTFS）

Firstly, OTFS-based RIS techniques were proposed with different objectives and metrics. Dinan et al. [38] proposed an OTFS-assisted RIS system for the downlink signal, and they also used a phase shift method to maximize the received signal. Bhat et al. [39] proposed an end-to-end method for the input-output relationship of an OTFS-based RIS architecture, which led to improved performance under the assistance of RIS. Bora et al. [40] presented an idea for RIS-assisted high mobility communication armed with OTFS, from which a MIMO RIS system with a lower BER than RIS could be observed. Li et al. [41] proposed a framework for both channel estimation and signal detection armed with an expectation-maximization algorithm under the OTFS method for millimeter wave communication. Xu et al.[42] provided a method for handling doubly selective fading channels in RIS-assisted networks, applicable in both the time-frequency (TF) and delay-doppler (DD) domains. At the same time, satellites were also considered in the framework. Abid et al. [43] proposed a deep learning approach using a deep neural network to compute the parameters of RIS-assisted OTFS systems for communication over high-speed channels. Li et al. [44] introduced a Kalman filter (KF) approach for channel estimation under RIS-assisted OTFS systems, while Abid et al. [45] proposed a wavelet-based OTFS method for channel estimation, and Zhao et al. [46] present a fast, programmable RIS enabling complex beamforming for enhanced wireless communication in diverse scenarios.

There are also many works for localization under NLoS conditions just armed with RIS. Ozturk et al. [47] provided a framework using Jacobi-Anger expansion and a maximum likelihood estimator to achieve near-field localization under the condition of amplitude variations. Pan et al. [2] gave an overview of localization in the RIS scenario, including some classical algorithms such as the MUSIC algorithm. Liu et al. [48] analyzed the Cramér-Rao lower bound for a multiple RIS-

assisted scenario. Famili et al. [49] proposed an indoor positioning system called OFDRA, where RIS is used to position drones, and provided very detailed analyses. Emenonye et al. [50] analyzed localization under far-field and near-field scenarios, respectively, and provided a Bayesian analysis of signal information. Gao et al. [51] analyzed the wireless conditions in the mmWave environment and aimed to optimize localization performance by position error bounds. Zheng et al. [52] proposed a joint RIS calibration system and presented a tensor ESPRIT algorithm to demonstrate the performance and solve positioning problems. Jiang et al. [53] introduced the idea of a two-timescale transmission design for a RIS-based positioning scheme. Zhao et al. [54] introduces a novel OAM-based LoS-MIMO architecture using directional beams without central voids, enhancing channel capacity and reducing correlation by leveraging wavefront phase variations as a new degree of freedom in wireless communication and [55] proposes a holography-inspired metasurface communication scheme using vortex beams to enable low-interference, multipair IoT transmissions under LoS conditions, demonstrating over 21 dB channel isolation in a 10 GHz prototype.

However, these previous works rarely pay attention to the PAPR analysis and the frame structure when the aim is to give the localization, or some work analysis the PAPR in other perspective [56]. So we would like to give some extension on this part. The high nonlinearity makes the extended Kalman filter (EKF) not always work so well, so we propose the robust velocity estimation method in our system. The system is RIS-assisted in order to complete the vehicle positioning and tracking in the V2X scenario armed with the MUSIC algorithm and UKF. This paper aims to detect the position of a high-speed vehicle when the GPS is not reliable due to some obstacles or buildings. In addition, the LoS path from the BS to the vehicle is blocked due to obstacles.

2.4 Related Studies for Multiple vehicles Scenario and Peak-Average-Power-Ratio (PAPR) Analysis

Chong et al. [57] analyzed the upper achievable rate limits of MU OTFS uplink transmissions using delay division multiple access (DDMA) and Doppler division multiple access (DoDMA), demonstrating superior robustness and performance compared with traditional OFDMA. Shahani et al. [58] proposed an enhanced data detection scheme for multi-antenna OTFS that improves the data rate, reliability, and robustness in dynamic and noisy environments. Sun et al. [59] developed an iterative detection algorithm that combines matched filtering and interference cancellation to enhance MU detection and mitigate interference in OTFS-NOMA satellite networks. Similarly, Augustine et al. [60] and Zhang et al. [61] introduced an iterative SIC-based MU detection algo-

rithm for uplink heterogeneous NOMA systems, achieving superior performance and fast convergence under both high and low mobility conditions. Deng et al. [62] proposed a resource hopping scheme to mitigate jamming effects in high-mobility OTFS-SCMA systems, significantly improving BER performance, while Yang et al. [63] designed a joint precoding scheme using interference alignment and singular value decomposition to effectively suppress inter-user interference in MU-MIMO OTFS systems. Ge et al. [64] introduced an OTFS-based NOMA framework with an iterative SIC turbo receiver, achieving robust detection and interference mitigation in heterogeneous mobility environments. Liu et al. [65] compared OTFS and OFDM in MU LEO satellite communications, highlighting OTFS' s superiority in interference management, sum-rate performance, and resource allocation. Ding et al. [66] further proposed an efficient OTFS-NOMA protocol that enhances spectral efficiency and communication reliability through optimized resource allocation and interference management. Chong et al. [67] analyzed the outage performance of single- and MU OTFS systems, confirming significant robustness gains over OFDM in high-mobility channels. Feng et al. [68] studied rectangular pulse-shaped OTFS for MU-MIMO with fractional delay and Doppler, proposing practical pulse designs for robust performance. Farhang et al. [69] established the equivalence between OTFS and SC-FDMA in delay-Doppler multiplexing, offering insights into MU resource allocation and standard compatibility. Rasheed et al. [70] developed a compressive sensing-based sparse channel estimation algorithm for uplink MU-OTFS, achieving superior performance under rapidly time-varying conditions. Although these studies have advanced OTFS-based MU communication by improving spectral efficiency, reliability, and robustness in high-mobility environments, pilot signal design remains underexplored, with most studies, such as in [70] only briefly addressing it, limiting practical implementation in dynamic MU networks. Moreover, relatively few studies have focused on the PAPR problem, which is crucial for a power-efficient transmission. For instance, [60] proposed an interleaved time-frequency multiple access (ITFMA) scheme that achieves better BER and PAPR through interleaved time-frequency allocation. Zhao et al. [71] introduced an iterative phase pre-distortion approach that achieved a 3.6 dB PAPR reduction with minimal BER degradation, whereas He et al. [72] proposed a clipping and logarithmic rooting companding method for DZT-OTFS, balancing low complexity and PAPR reduction. Mehrotra et al. addressed high PAPR in Zak-OTFS using spread carrier waveforms, reducing PAPR to around 6.58 dB while preserving robustness. Ma et al. [73] utilized Zadoff–Chu sequences for low-PAPR pilot design, achieving accurate channel estimation under Doppler shifts. Hegazy et al. [74] proposed a super-resolution deep learning-based OTFS-ISAC framework to mitigate the high PAPR and Doppler effects in THz systems, whereas Liu et al. [75] optimized waveforms under PAPR and energy constraints for ISAC-OTFS to enhance the sensing SNR. Ahsan et al. [76] developed a semi-supervised vectored delay-sequence selective mapping

technique that achieved effective PAPR reduction while maintaining the BER and spectral efficiency under 3GPP doubly dispersive channels.

2.5 Adaptive MUSIC Algorithm

Accurate and reliable vehicle localization is essential for intelligent transportation systems (ITS), autonomous driving, and vehicular communication networks. Traditional localization methods rely on GPS, which suffers from severe degradation in dense urban areas, tunnels, and non-line-of-sight (NLoS) scenarios. To overcome these limitations, radio-based direction-of-arrival (DOA) estimation has attracted significant attention due to its potential to achieve high-resolution localization without additional infrastructure.

Among DOA estimation methods, MUSIC and Root-MUSIC are well-known for their ability to resolve multiple incident signals with fine resolution. Root-MUSIC, in particular, exhibits high accuracy in interference-free or low-noise conditions. However, in practical vehicular scenarios, signals often encounter multipath propagation and strong interference, which can cause Root-MUSIC to fail. In contrast, Forward-Backward Spatial Smoothing (FBSS) techniques can effectively mitigate coherent interference by decorrelating the received signals, thus enhancing robustness under harsh conditions.

Direction-of-arrival (DoA) estimation has been a long-standing research focus, where subspace-based algorithms such as MUSIC and its variants play a central role.

In [77], Paaso et al. proposed a forward-backward spatial smoothing (FBSS) enhanced MUSIC algorithm to improve angular resolution in multi-radar systems, demonstrating robustness against coherent interference in vehicular localization scenarios. Similarly, Liu, et al. [78] developed an enhanced root-MUSIC method based on multi-resolution composite arrays (MRCAs), which reduces computational complexity and alleviates spatial aliasing when the array aperture is limited. Extending these ideas to intelligent reflecting surface (IRS)-aided MIMO systems, Masood et al. [79] combined inductive matrix completion (IMC) with root-MUSIC and FBSS, enabling efficient cascaded channel estimation with reduced training overhead. In the context of smart antennas, Chen et al. [80] integrated MUSIC with FBSS for blind uplink signal identification in multibeam arrays, validating its feasibility under diverse signal conditions. Meanwhile, Cha et al. [81] introduced novel signal processing schemes for homodyne FMCW radar, experimentally comparing conventional MUSIC, FBSS-MUSIC, and beamspace-MUSIC to enhance angular resolution. A related contribution by Wang et al. [82] introduced two-dimensional spatial smoothing (SS) and FBSS to effectively separate multipath coherent signals, thereby improving the accuracy of both MUSIC and ESPRIT in mobile communications. To further address coherent source

challenges, Kaneko et al. [83] proposed an iterative angle-of-arrival (AoA) estimation algorithm that avoids spatial smoothing, achieving higher resolution than FBSS-based MUSIC. Likewise, Yan et al. [84] designed a cyclostationarity-based wideband DOA estimation method using a conjugate MRLA with FBSS, showing improved detection compared to cyclic MUSIC. In addition, Dihua et al. [85] presented the FB-SED algorithm, which combines forward-backward averaging with eigendecomposition to outperform FBSS-MUSIC in coherent signal environments. Comprehensive evaluations of smoothing techniques were reported by Thompson et al. [86], who analyzed SS and FBSS for correlated and coherent sources, confirming the robustness of FBSS under various phase conditions. To exploit new array structures, Li et al. [87] proposed a moving coprime array scheme that integrates interpolation, matrix completion, FBSS, and root-MUSIC, thereby improving robustness and resolution. Along similar lines, Liu et al. [88] introduced a joint DOA–range estimation algorithm for coherent signals using a moving time-modulated frequency diverse coprime array (MTFDCA), restoring covariance rank and enabling high-precision 2D-MUSIC estimation. Finally, Sorkhabi et al. [89] developed a practical approach for multi-target DOA estimation in mmWave MIMO radar with limited sensors by combining 2D-MUSIC and FBSS, validating its effectiveness through both simulation and real-world experiments.

Chapter 3

LoS-Based DoA Estimation and Vehicle Tracking

3.1 Overview of the Proposed LoS Localization Framework

With the advancement of Beyond 5G/6G technologies, accurate positioning and velocity estimation in Internet of Vehicles (IoV) systems has become increasingly critical. Although GPS can provide real-time location information, its performance degrades significantly in environments with heavy obstructions, such as urban areas surrounded by skyscrapers. To address this limitation, this study proposes a positioning framework that relies on channel parameter estimation derived from multi-antenna signal processing. Specifically, we adopt an adaptive low-complexity 2D MUSIC (ALC2D-MUSIC) algorithm to estimate signal directions, and further apply an unscented Kalman filter (UKF) using extracted Direction of Arrival (DoA) and Time of Arrival (ToA) information to estimate vehicle positions and velocities. The proposed system is robust to variations in road geometry, making it suitable for deployment in diverse traffic environments. Simulation results demonstrate that our method achieves high estimation accuracy and outperforms a compressive sensing-based approach across different SNR levels, angular search resolutions, and antenna array sizes. Furthermore, the UKF-based tracking algorithm shows superior performance in curved road scenarios, validating its effectiveness under realistic mobility conditions.

With the development of Beyond 5G/6G, accurate detection of vehicle position and velocity in the Internet of Vehicles (IoV) has become increasingly important. Considerable research has been devoted to improving vehicle positioning accuracy [12]. Although the Global Positioning System (GPS) provides accurate and real-time location information, its performance degrades significantly in environments with severe signal obstructions, such as intersections surrounded by skyscrapers, large buildings, or other urban structures. Under such conditions, GPS may fail to

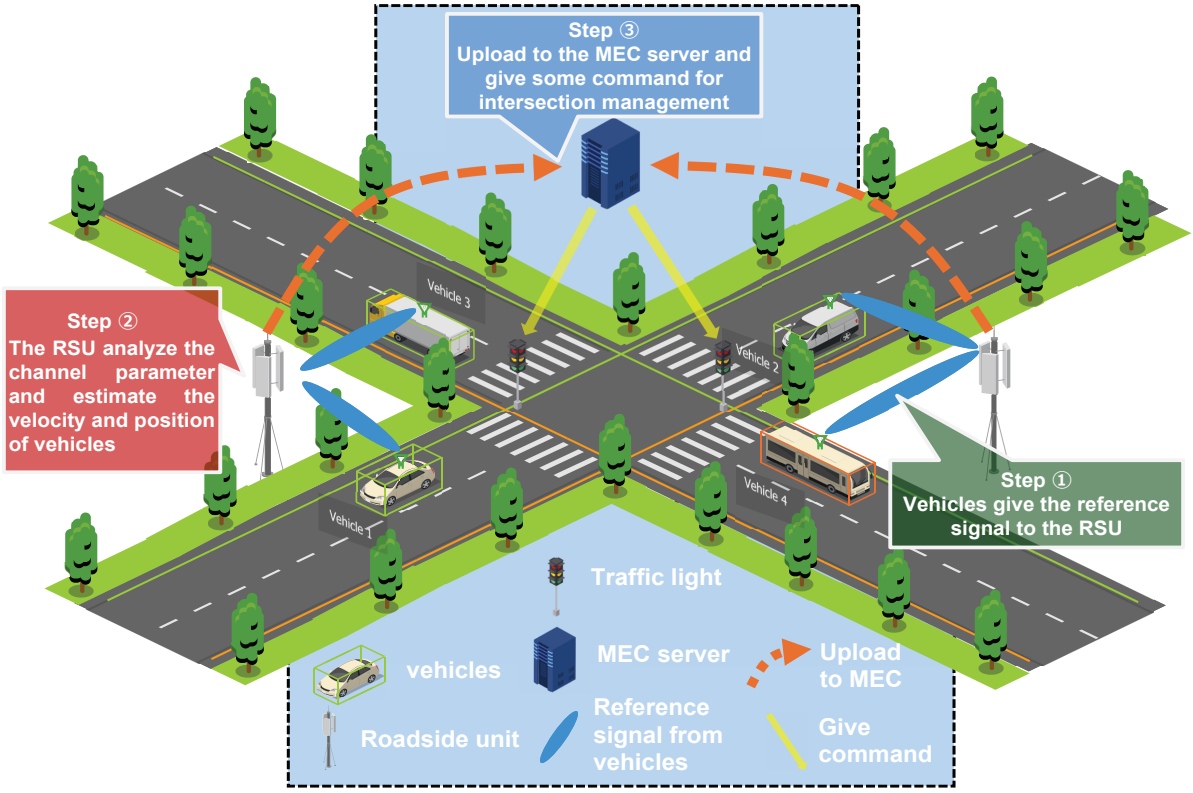


Fig.3.1: The LoS System overview.

deliver reliable positioning, prompting the exploration of alternative approaches, such as LiDAR or channel-parameter-based estimation methods [18].

While LiDAR can offer high-precision positioning, it requires expensive hardware and detailed 3D maps, making it impractical for large-scale deployment. In contrast, channel estimation emerges as a cost-effective and scalable alternative for vehicle positioning in real-world environments. In recent years, millimeter-wave (mmWave) communication [4] has attracted significant attention in vehicular networks due to its ability to provide high bandwidth and low latency. The directional nature of mmWave signals also makes them well-suited for precise localization. However, because mmWave propagation is limited to narrow beams with high path loss, it is essential to continuously track beam directions, especially for high-speed vehicles [90]. This paper proposes a vehicle tracking framework based on multi-antenna mmWave systems. To overcome the high path loss of mmWave signals, base stations (BSs) are equipped with large antenna arrays, enabling accurate estimation of signal arrival directions. We apply a low-complexity two-dimensional Multiple Signal Classification (2D-MUSIC) algorithm to extract channel parameters such as the Direction of Arrival (DoA) and Time of Arrival (ToA). These parameters are then used

as inputs to an Unscented Kalman Filter (UKF), which refines the estimation of vehicle positions and velocities over time. Traditional Kalman filter-based tracking methods often assume fixed or straight road structures, limiting their effectiveness in more complex scenarios such as curved roads or intersections. By incorporating channel parameters into the UKF estimation process, the proposed system achieves improved scalability and adaptability. This design enables accurate tracking of vehicle states independent of road geometry, making it suitable for a wide range of urban traffic environments.

Table3.1: Summary of Notations for the LoS model.

Parameter	Explanation	Parameter	Explanation
— MUSIC Parameters —			
$PO_j^{RSU} = [x_j, y_j, z_j]$	Position of the j-th RSU	$PO_i^V = [p_{x_i}, p_{y_i}, p_{z_i}]$	Position of the i-th vehicle
$\mathbf{H}[t]$	Channel matrix	$\mathbf{A}_{R,v}(\varphi_v, \vartheta_v)$	Steering vector for elevation angle
$\mathbf{\Gamma}_v$	Complex path gain for vehicle v	$\mathbf{A}_T^H(\psi_{T,v})$	Transmitter steering vector
$\mathbf{a}_{R,v}(\varphi_{R,v})$	Steering vector for elevation DoA	$\mathbf{a}_{R,v}(\theta_{R,v})$	Steering vector for azimuth DoA
$\mathbf{A}1_T(\psi_v)$	Tx steering matrix for all vehicles	$\mathbf{A}1_R(\varphi_{R,v}, \theta_{R,v})$	Rx steering matrix for all vehicles
$\mathbf{s}(t)$	Reference signal	$\mathbf{y}(t)$	Received signal
t	Time slot	$\psi_{T,v}$	Tx angle of vehicle v
$\varphi_{R,v}$	Elevation DoA for vehicle v	$\theta_{R,v}$	Azimuth DoA for vehicle v
— Kalman Filter Parameters —			
$\mathbf{A}$	Transition matrix	$\mathbf{x}[n]$	State vector at time n
$\mathbf{u}$	Process covariance	$\mathbf{K}(n+1)$	Kalman gain
α	UKF scaling parameter 1	β	UKF scaling parameter 2
$(p_{x_i}, p_{y_i}, p_{z_i})$	Position of vehicle i in 3D	$(v_{x_i}, v_{y_i}, v_{z_i})$	Velocity of vehicle i in 3D
$(a_{x_i}, a_{y_i}, a_{z_i})$	Acceleration of vehicle i in 3D	$\omega[n]$	UKF sigma point weight
$\lambda[n]$	UKF scaling factor		

By leveraging mmWave communication technologies, our proposed scheme enhances both the accuracy of vehicle positioning and the reliability of data transmission. This capability is especially critical in the context of Beyond 5G/6G networks, where demands for high data rates and precise localization continue to increase. Ultimately, our approach aims to provide a robust and scalable solution to the challenges faced in IoV systems, paving the way for safer and more efficient vehicular networks.

The main contributions of this work are summarized as follows:

- We construct an adaptive low-complexity 2D MUSIC estimation architecture to detect the channel parameters (DoAs, ToAs) and then use them to estimate the velocities and positions of each vehicle in the intersection even under some variations of the transmitting signals.
- We propose an UKF method to analyze the position and velocity of the vehicles based on the channel parameters obtained in the last step and give some relatively difficult curve for

the route.

- We complete the simulation in a software way and get the metrics and performance of our framework.

3.2 Reference Signal Design and System Workflow

In this section, we will briefly introduce the architecture in our framework. As illustrated in Figure 3.1, we consider an Intersection scenario when the GPS is in bad condition. There are 3 roles in this proposed framework. i.e., the vehicle, the roadside unit (RSU), and the multi-access edge computing (MEC) node. Their respective roles are as follows.

Vehicle: The primary objective of this framework is to estimate position and velocity with greater accuracy. In our system architecture, every vehicle is equipped with antennas that transmit reference signals in a sweeping beam manner. Then, the RSU will receive the reference signal and then use it to estimate the velocity and position of each vehicle.

RSU: RSUs are constructed along the road, and they will receive the signal from all vehicles and then analyze them for the velocity and position estimation. They can obtain DoAs of the azimuth and elevation as the channel parameters. Although this information is used for velocity estimation, combined with the ToA from the time of flight also as one of the inputs, the RSU will calculate the velocities and positions armed with an UKF.

MEC node: The MEC node is a central node served like a manager in an intersection. We use them to control the information interaction in multiple intersections. The RSUs send the velocity and location data they collected to the MEC node, and then the MEC node will send the planning decision to all vehicles and traffic lights to complete the intersection management.

The reference signal is a kind of signal used to help estimate the parameters of the current channel. Also, the reference signal is a known signal by all users, including the vehicles and the RSUs. It has various forms for its formation, for example, some reference signals will have the identification of the transmitting vehicle, whereas the overhead of the signal will become larger; there is also a kind of reference signal that does not have the identification, whose overhead will become extremely light. In our architecture, without loss of generality, we assume that each reference signal has the identifier of the corresponding vehicle.

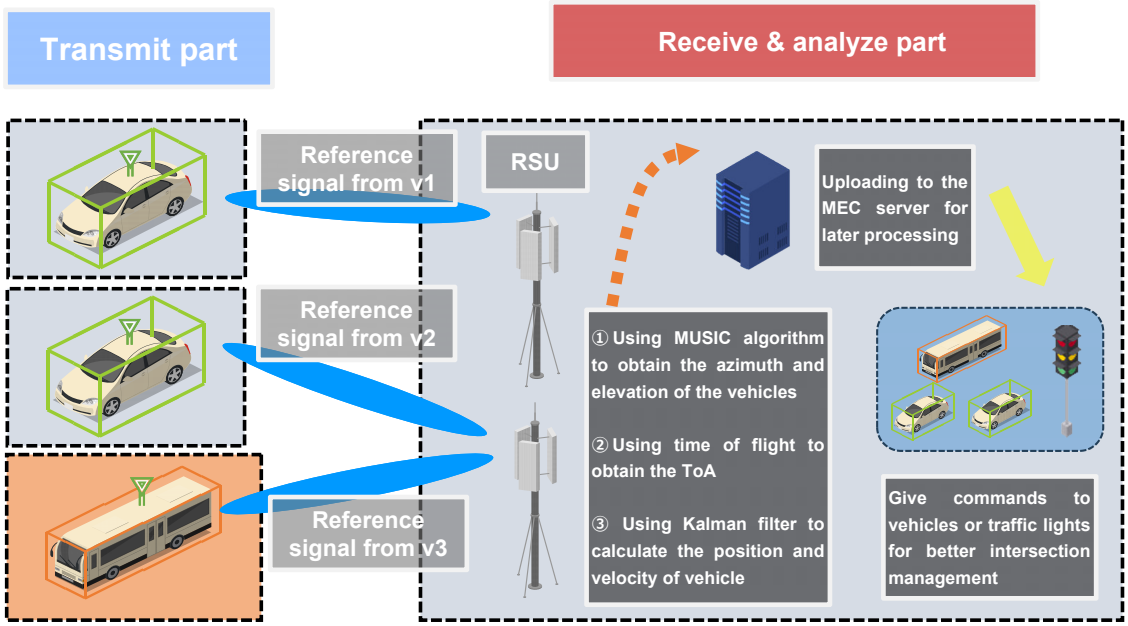


Fig.3.2: Overview of the proposed method in LoS environment.

3.3 MIMO Channel Modeling and Spatial Covariance Construction

Our system model has many vehicles, several RSUs, and MEC nodes in an intersection depicted in Figure 3.1. We assume the vehicle periodically transmits the reference signal in a sweep beam manner to the surrounding environment. Additionally, the j-th RSU is assumed to know its position accurately as,

$$PO_j^{RSU} = [x_j, y_j, z_j], \tag{3.1}$$

Similarly, the position of the i-th vehicle in the intersection (not known by RSUs) can be denoted as,

$$PO_i^{V} = [p_{x_i}, p_{y_i}, p_{z_i}], \tag{3.2}$$

We define the process as an uplink process, which means that the vehicles will send their reference signal periodically to the environment when the GPS is out of work. Then, we consider our channel scenario. The first is for the transmitter part, i.e., the vehicles. Each vehicle has a transmitting antenna system who have E_T antenna elements as a form of ULA of $E_T \times 1$, which transmits the reference signal. Then, the receiving part, i.e. the RSUs. They will receive the

reference signals from vehicles and then estimate the DoA of each vehicle. Similarly, we define that each RSU has an antenna system with E_R antenna elements as a uniform rectangular array (URA), which has the form of $E_R = L_R \times W_R$. Hence, under the system, we have the transmitting and receiving MIMO system. The channel can be described as,

$$\mathbf{H}[t] = \sum_{v=0}^{V} \mathbf{A}_{R,v}(\varphi_v, \theta_v)\Lambda_v(t)\,\mathbf{A}_{T,v}^{\mathrm{H}}(\psi_v)\,e^{-j2\pi f_0 \tau_v}, \tag{3.3}$$

where t is the time slot when the channel parameter can be seen as invariant and extreme enough to transmit a group of reference signals. $\mathbf{\Lambda}_v(t)$ denotes the complex gain on the v-th vehicle in the t-th time slot. $e^{-j2\pi f_0 \tau_v}$ stands for the phase-shifted when the propagation is τ_v and the transmitting frequency is f_0. For the antenna arrays part, without loss of generality, we assume the interval of each antenna is 0.5 of the wavelengths. Thus, we can denote the vector response as,

$$\begin{aligned}
\mathbf{A}_{T,v}(\psi_v) &= \left[1, \mathrm{e}^{j\pi\cos(\psi_v)}, \ldots, \mathrm{e}^{j\pi(E_T-1)\cos(\psi_v)}\right]^{\mathrm{T}} \in \mathbb{C}^{1\times E_T}, \\
\mathbf{a}_{R,v}(\varphi_v, \theta_v) &= \begin{bmatrix} 1, \mathrm{e}^{j\pi\cos(\varphi_v)\sin(\theta_v)}, \ldots \\ , \mathrm{e}^{j\pi(L_R-1)\cos(\varphi_v)\sin(\theta_v)} \end{bmatrix}^{\mathrm{T}} \in \mathbb{C}^{1\times L_R}, \\
\mathbf{a}_{R,v}(\theta_v) &= \left[1, \mathrm{e}^{j\pi\cos(\theta_v)}, \ldots, \mathrm{e}^{j\pi(W_R-1)\cos(\theta_v)}\right]^{\mathrm{T}} \in \mathbb{C}^{1\times W_R},
\end{aligned} \tag{3.4}$$

Based on the above definition, we can have the ψ_v, φ_v and θ_v as the transmitting angles, the elevation angle of direction of arrival and azimuth angle of direction of arrival for v-th vehicle respectively. Furthermore, $\mathbf{A}_{\mathrm{t}}(\varphi_{\mathrm{t},v}, \theta_{\mathrm{t},v})$ are the antenna array responses for the transmitting part and the receiving part. Also, the $\mathbf{A}_{R,v}(\varphi_v, \theta_v)$ can be expressed as,

$$\mathbf{A}_{R,v}(\varphi_v, \theta_v) = \mathbf{a}_{R,v}(\theta_v) \otimes \mathbf{a}_{R,v}(\varphi_v, \theta_v) \in \mathbb{C}^{L_R W_R \times 1}, \tag{3.5}$$

where the mark $\otimes$ means the Kronecker product. Based on the vector mentioned above, we give the matrix of the steering vector overall v-th vehicle as follows:

$$\begin{aligned}
\mathbf{A}1_T(\psi_v) &= [\mathbf{A}_{T,1}(\psi_1), \cdots, \mathbf{A}_{T,v}(\psi_v)] \in \mathbb{C}^{E_T\times V}, \\
\mathbf{A}1_R(\varphi_v, \theta_v) &= [\mathbf{A}_{R,1}(\varphi_1, \theta_1), \cdots, \mathbf{A}_{R,v}(\varphi_v, \theta_v)] \in \mathbb{C}^{L_R W_R \times V},
\end{aligned} \tag{3.6}$$

As for the reference signal, a kind of already known signal is used to estimate the channel and DoA parameters. It can be uplink or downlink. Reference signals are transmitted by each vehicle and we suppose the use of orthogonal sequences such as the Zadoff-Chu sequences which can be separated in the code domain from multiple sources in the shared spectral resources [91]. RSUs will receive them and then estimate the channel parameters between them and the vehicles. In order to describe it more directly, we use the illustration to help comprehension shown in Figure 3.2.

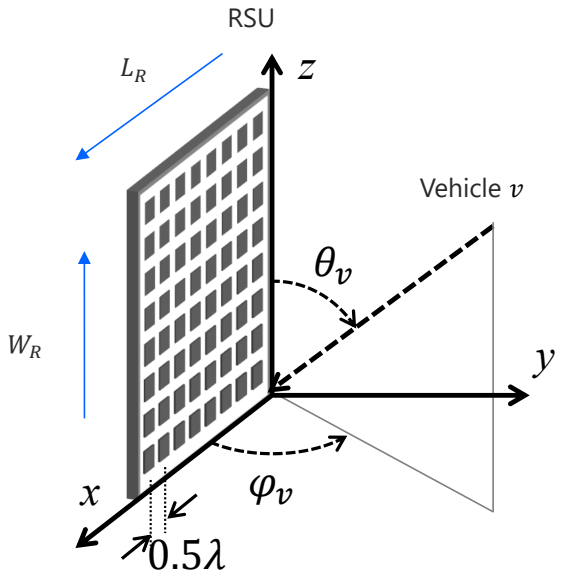


Fig.3.3: Illustration of the reference signal transmission.

3.4 ALC2D-MUSIC Algorithm-based DoA Estimation

In this section, we will describe the adaptive low-complexity 2D MUSIC model. As for the conventional MUSIC algorithm, it searches the angles in a 2D form, which will make the complexity extremely large, as shown in Figure 3.3 We assume that the vehicle antenna system will transmit one signal symbol from each antenna element within the time duration, and we denote the transmission signal as,

$$\mathbf{s}_v(t) = [s_v(1,t), \ldots, s_v(E_T,t)]^{\mathrm{T}} \in \mathbb{C}^{E_T \times 1} \tag{3.7}$$

where $s_v(E_T,t)$ is the reference signal transmitted at the E_T-th element antenna of the v-th vehicle in the time window t, assuming that the channel parameter can be assumed to be constant when estimating the azimuth and elevation during the time window. Thus, the signal from different vehicles can be summarized as follows:

$$\mathbf{s}(t) = [\mathbf{s}_1(t), \cdots \mathbf{s}_V(t)] \in \mathbb{C}^{E_T \times V}. \tag{3.8}$$

We will be able to obtain the received signal in the receiving end, i.e. the RSU part as the following part:

$$\mathbf{y}(t) = \mathbf{H}(t)\mathbf{s}(t)e^{-j2\pi f_0 \tau_v} + \mathbf{n}(t) \in \mathbb{C}^{E_R \times V}, \tag{3.9}$$

Therefore, we continue to calculate the received signal by using the definition of the channel as follows:

$$\begin{aligned}\mathbf{y}(t) = \mathbf{A}1_R(\varphi_v, \theta_v) \cdot \Lambda_v(t) \cdot \mathbf{A}1_T^{\mathrm{H}}(\psi_v) \\ \cdot e^{-j2\pi f_0 \tau_v} \cdot \mathbf{s}(t) + \mathbf{n}(t) \in \mathbb{C}^{E_R \times V}\end{aligned} \tag{3.10}$$

In this processing, we change the complex-gain $\mathbf{\Lambda}_v(t)$ to a vector $\alpha(t)$. For the conventional, we analyze the signal by each antenna element, and then we can calculate the covariance matrix of the receiving signal:

$$\begin{aligned}&\mathbf{R} = \mathbb{E}\left[\mathbf{y}(t)\mathbf{y}(t)^{\mathrm{H}}\right] = \\ &\Gamma\mathbf{A}1_R(\varphi_v, \theta_v)\mathbb{E}\left[\mathbf{A}1_T(\psi_v)\mathbf{s}\mathbf{s}^H\mathbf{A}1_T^H(\psi_v)\right]\mathbf{A}1_R^H(\varphi_v, \theta_v) \\ &+\mathbb{E}\left[\mathbf{Z}\mathbf{Z}^H\right] = \Gamma\mathbf{A}1_R\mathbf{R}_\mathbf{S}\mathbf{A}1_R^H + \sigma^2\mathbf{I}_{E_R},\end{aligned} \tag{3.11}$$

in the equation, to simplify the expression, we introduce Γ as an auxiliary parameter, including all the scalars such as $e^{-j2\pi f_0 \tau_v}$ and $\Lambda_p(t)$. So, based on the conventional MUSIC algorithm, we will calculate the eigenvalue and search the angles of the arrival, while the complexity will be extremely large in a 2 dimension, as shown in Figure 3.4. This figure illustrates the two-dimensional MUSIC spatial spectrum obtained from the proposed angle estimation scheme. The horizontal axis represents the azimuth angle ϕ, while the vertical axis denotes the elevation angle θ. The power spectrum exhibits distinct and sharp peaks at specific (ϕ, θ) locations, corresponding to the estimated horizontal and vertical angles of the received signal paths. These peaks indicate the jointly estimated azimuth and elevation directions of arrival, demonstrating that the proposed method can accurately resolve the 2D angular information in both horizontal and vertical domains.

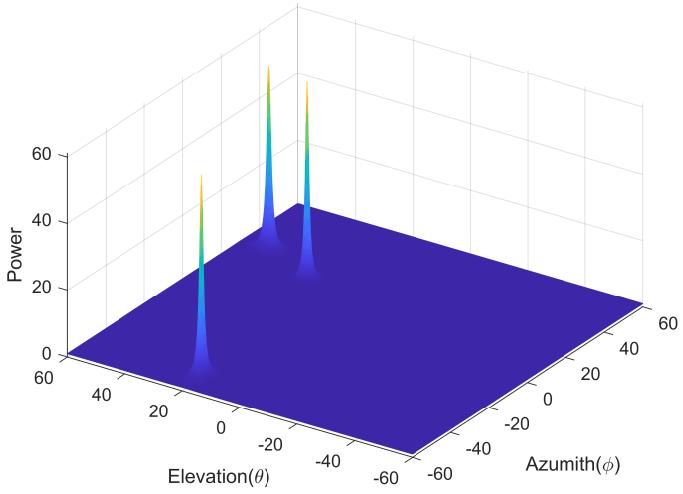


Fig.3.4: The conventional MUSIC algorithm in a 2D searching mode.

Besides, in order to legitimate the complexity of our calculation, we will give some transfor-

$$\mathbf{A}_{1_R} = \begin{bmatrix} 1 & 1 & \cdots & 1 \\ e^{j\frac{2\pi l}{\lambda}\cos\theta_1} & e^{j\frac{2\pi l}{\lambda}\cos\theta_2} & \cdots & e^{j\frac{2\pi l}{\lambda}\cos\theta_V} \\ \vdots & \vdots & \cdots & \vdots \\ e^{j(L_R-1)\frac{2\pi l}{\lambda}\cos\theta_1} & e^{j(L_R-1)\frac{2\pi l}{\lambda}\cos\theta_2} & \cdots & e^{j(L_R-1)\frac{2\pi l}{\lambda}\cos\theta_V} \\ e^{j\frac{2\pi l}{\lambda}\cos\varphi_1} & e^{j\frac{2\pi l}{\lambda}\cos\varphi_2} & \cdots & e^{j\frac{2\pi l}{\lambda}\cos\varphi_V} \\ \vdots & \vdots & \cdots & \vdots \\ e^{j\frac{2\pi l}{\lambda}[(L_R-1)\cos\theta_1+\cos\varphi_1]} & e^{j\frac{2\pi l}{\lambda}[(L_R-1)\cos\theta_2+\cos\varphi_2]} & \cdots & e^{j\frac{2\pi l}{\lambda}[(L_R-1)\cos\theta_V+\cos\varphi_V]} \\ \vdots & \vdots & \cdots & \vdots \\ e^{j(W_R-1)\frac{2\pi l}{\lambda}\cos\varphi_1} & e^{j(W_R-1)\frac{2\pi l}{\lambda}\cos\varphi_2} & \cdots & e^{j(W_R-1)\frac{2\pi l}{\lambda}\cos\varphi_V} \\ \vdots & \vdots & \cdots & \vdots \\ e^{j\frac{2\pi l}{\lambda}[(L_R-1)\cos\theta_1+(W_R-1)\cos\varphi_1]} & e^{j\frac{2\pi l}{\lambda}[(L_R-1)\cos\theta_2+(W_R-1)\cos\varphi_2]} & \cdots & e^{j\frac{2\pi l}{\lambda}[(L_R-1)\cos\theta_V+(W_R-1)\cos\varphi_V]} \end{bmatrix} \in \mathbb{C}^{L_R W_R \times V}. \tag{3.13}$$

mations for the array response vector. First, we have $\mathbf{A}_R(\varphi_v, \theta_v) \in \mathbb{C}^{E_R \times 1}$, like the definition in Eq. (3.5). Thus, we exchange the Kronecker product

$$\mathbf{A'}_R\left(\varphi_p, \theta_p\right) = \mathbf{a}_R(\varphi_p) \otimes \mathbf{a}_R(\theta_p) \in \mathbb{C}^{W_R L_R \times 1}, \tag{3.12}$$

And we demonstrate the matrix of $\mathbf{A}1_R(\varphi_v, \theta_v) \in \mathbb{C}^{L_R W_R \times 1}$ and $\mathbf{A}1'_R(\varphi_v, \theta_v) \in \mathbb{C}^{W_R L_R \times 1}$, from the equation, we can see that the top L_R rows only have the information of the elevation DoA, i.e. θ, so we can divide it into 2 parts as following:

$$\mathbf{A}1_R = \begin{bmatrix} \mathbf{A}1_R(\theta_v) \\ \mathbf{A}1_R(\varphi_v, \theta_v) \end{bmatrix}. \tag{3.15}$$

Similarly, we can also divide the matrix $\mathbf{A'}_r$:

$$\mathbf{A}1'_R = \begin{bmatrix} \mathbf{A}1'_R(\varphi_v) \\ \mathbf{A}1'_R(\varphi_v, \theta_v) \end{bmatrix} \tag{3.16}$$

Based on the conventional algorithm, we can calculate and obtain the received signal' s covariance matrix:

$$\begin{aligned} \mathbf{R}_\theta &\triangleq \mathbb{E}\left[\mathbf{X}_\theta \mathbf{X}_\theta^H\right] \\ &= \mathbf{A}1_R(\theta_v)\mathbf{R}\mathbf{A}1_R^H(\theta_v) + \sigma^2 \mathbf{I}_{L_R} \end{aligned} \tag{3.17}$$

$$\begin{aligned} \mathbf{R}_\varphi &\triangleq \mathbb{E}\left[\mathbf{X'}_\varphi \mathbf{X'}_\varphi^H\right] \\ &= \mathbf{A1'}_R(\varphi_v)\mathbf{R}\mathbf{A1'}_R^H(\varphi_v) + \sigma^2 \mathbf{I}_{W_R} \end{aligned} \tag{3.18}$$

$$\mathbf{A'}_{1_R} = \begin{bmatrix} 1 & 1 & \cdots & 1 \\ e^{j\frac{2\pi l}{\lambda}\cos\varphi_1} & e^{j\frac{2\pi l}{\lambda}\cos\varphi_2} & \cdots & e^{j\frac{2\pi l}{\lambda}\cos\varphi_V} \\ \vdots & \vdots & \cdots & \vdots \\ e^{j(W_R-1)\frac{2\pi l}{\lambda}\cos\varphi_1} & e^{j(W_R-1)\frac{2\pi l}{\lambda}\cos\varphi_2} & \cdots & e^{j(W_R-1)\frac{2\pi l}{\lambda}\cos\varphi_V} \\ e^{j\frac{2\pi l}{\lambda}\cos\theta_1} & e^{j\frac{2\pi l}{\lambda}\cos\theta_2} & \cdots & e^{j\frac{2\pi l}{\lambda}\cos\theta_V} \\ \vdots & \vdots & \cdots & \vdots \\ e^{j\frac{2\pi l}{\lambda}[(W_R-1)\cos\varphi_1+\cos\theta_1]} & e^{j\frac{2\pi l}{\lambda}[(W_R-1)\cos\varphi_2+\cos\theta_2]} & \cdots & e^{j\frac{2\pi l}{\lambda}[(W_R-1)\cos\varphi_V+\cos\theta_V]} \\ \vdots & \vdots & \cdots & \vdots \\ e^{j(L_R-1)\frac{2\pi l}{\lambda}\cos\theta_1} & e^{j(L_R-1)\frac{2\pi l}{\lambda}\cos\theta_2} & \cdots & e^{j(L_R-1)\frac{2\pi l}{\lambda}\cos\theta_V} \\ \vdots & \vdots & \cdots & \vdots \\ e^{j\frac{2\pi l}{\lambda}[(W_R-1)\cos\varphi_1+(L_R-1)\cos\theta_1]} & e^{j\frac{2\pi l}{\lambda}[(W_R-1)\cos\varphi_2+(L_R-1)\cos\theta_2]} & \cdots & e^{j\frac{2\pi l}{\lambda}[(W_R-1)\cos\varphi_V+(L_R-1)\cos\theta_V]} \end{bmatrix} \in \mathbb{C}^{W_R L_R \times V}. \tag{3.14}$$

and get the eigenvalue decomposition

$$\mathbf{R}_\varphi = \mathbf{U}_\varphi \mathbf{\Sigma}_\varphi \mathbf{V}_\varphi^H \tag{3.19}$$

$$\mathbf{R}_\theta = \mathbf{U}_\theta \mathbf{\Sigma}_\theta \mathbf{V}_\theta^H \tag{3.20}$$

From Eq. (3.11), we can see that we put the transmitting antenna array into the covariance matrix, and it can be seen as a total part and then directly process it in Eq. (3.17) and Eq. (3.18) no matter how the transmitting antenna array changes, which can be adaptive no matter how the transmitting matrix and signal changes, i.e. the ALC2D-MUSIC algorithm, and complete the MUSIC process.

We adopt the MUSIC algorithm to find the DoA by using the following equations:

$$\mathbf{Q}(\varphi) = \frac{1}{\mathbf{a}_R(\varphi_v)^H \mathbf{V}_\varphi \mathbf{V}_\varphi^H \mathbf{a}_R(\varphi_v)} \tag{3.21}$$

$$\mathbf{Q}(\theta) = \frac{1}{\mathbf{a}_v(\theta_v)^H \mathbf{V}_\theta \mathbf{V}_\theta^H \mathbf{a}_v(\theta_v)} \tag{3.22}$$

So, based on the above description, we will be able to obtain the DoA, including the azimuth and the elevation for each vehicle.

While both 2D-MUSIC and the UKF have indeed been individually applied in prior works for vehicle localization and beam tracking, our contribution lies in their tailored integration and application under a new system perspective. Specifically, although 3D-MUSIC is more widely adopted

in the literature, we intentionally adopt a 2D-MUSIC algorithm in this work to significantly reduce computational complexity, which is crucial for real-time vehicular applications. Moreover, unlike conventional approaches that rely heavily on predefined road structures or map constraints to formulate the Kalman filter update equations, our method directly uses physical *channel features*—notably DoA—as measurement inputs to the UKF. This allows our system to operate effectively even in unstructured or dynamic environments without depending on road geometry. The core innovation of this work is the organic integration of 2D-MUSIC and UKF, where the DoA estimation from the MUSIC algorithm serves as a real-time external feedback to the UKF. This tight coupling enhances the robustness and accuracy of vehicle tracking, and offers a novel solution for RSU/BS-assisted localization in future Beyond 5G/6G vehicular networks.

3.5 Proposed UKF-Based Vehicle State Estimation

3.5.1 Unscented Kalman filter Method

We will introduce the 2 part Kalman filter. In the first part, we estimate the channel parameters based on the reference signal. In the second part, we estimate the velocity and the position of the vehicles under the acceleration environment. The vehicles usually have a constant velocity when the channel estimation is considered. When the acceleration conditions are considered, the system usually does not consider the channel parameters estimation, and they usually directly use the Kalman filter to estimate the vehicles' position. However, under this kind of method, the Kalman filter method will almost depend on the road structure, which is difficult to adopt on other road structures. However, the system that uses the channel parameters to help estimate the velocity will perform better when the road structure changes.

As for the second part, we adopt the Kalman filter to estimate the positions and velocities of vehicles. The Kalman filter equation can be expressed as follows:

$$\begin{cases} x[n+1] = Ax[n] + u[n], \\ \widehat{\mathbf{\Theta}}[n] = \mathbf{h}(\mathbf{x}[n]) + \mathbf{v}[n]l \end{cases} \tag{3.23}$$

Considering the velocity change in a real scenario, we add the acceleration part, i.e. the acceleration part, where we have the state vector as

$$\mathbf{x}[n] = [p_x, p_y, p_z, v_x, v_y, v_z, a_x, a_y, a_z] \tag{3.24}$$

where the parameter p_* means the position in the * axis direction, the v_* denotes the velocities in the * axis direction, and the a_* stands for the acceleration in * axis direction. Also, we can have the transfer matrix as

$$\mathbf{A} = \begin{bmatrix} 1 & 0 & 0 & \Delta t & 0 & 0 & 0.5\Delta t^2 & 0 & 0 \\ 0 & 1 & 0 & 0 & \Delta t & 0 & 0 & 0.5\Delta t^2 & 0 \\ 0 & 0 & 1 & 0 & 0 & 0 & 0 & 0 & 0.5\Delta t^2 \\ 0 & 0 & 0 & 1 & 0 & 0 & \Delta t & 0 & 0 \\ 0 & 0 & 0 & 0 & 1 & 0 & 0 & \Delta t & 0 \\ 0 & 0 & 0 & 0 & 0 & 1 & 0 & 0 & \Delta t \\ 0 & 0 & 0 & 0 & 0 & 0 & 1 & 0 & 0 \\ 0 & 0 & 0 & 0 & 0 & 0 & 0 & 1 & 0 \\ 0 & 0 & 0 & 0 & 0 & 0 & 0 & 0 & 1 \end{bmatrix}.$$

As for the measurement equation, we can specifically express it as,

$$\widehat{\mathbf{\Theta}}[n] = \mathbf{h}(\mathbf{x}[n]) + \mathbf{v}[n] = \begin{bmatrix} \frac{r[n]}{c} + v_\tau[n] \\ \varphi_R[n] + v_\varphi[n] \\ \vartheta_R[n] + v_\vartheta[n] \end{bmatrix} = \begin{bmatrix} \frac{\|\mathbf{p}[n]-\mathbf{p}_0\|}{c} + v_r[n] \\ \arctan\left(\frac{p_y[n]-p_0}{p_x-p_0}\right) + v_\varphi[n] \\ \arccos\left(\frac{p_z[n]-p_0}{\|\mathbf{p}[n]-\mathbf{p}_0\|}\right) + v_\vartheta[n] \end{bmatrix}.$$

In the equation, $\mathbf{u}[n]$ is the system noise, and the $\mathbf{v}[n]$ is the measurement noise. Thus, we introduce the UKF method. Base on the Unscented Kalman filter transformation rule, We first need to give an unscented transformation of $\mathbf{x}[n]$ for the collected data as the following form:

$$\begin{cases} \mathbf{x}[n]^{(0)}, i = 0 \\ \mathbf{x}[n]^{(i)} + \left(\sqrt{(a_{UT}+\lambda)\mathbf{P}}\right)_i, i = 1 \cdots a_{UT} \\ \mathbf{x}[n]^{(i)} - \left(\sqrt{(a_{UT}+\lambda)\mathbf{P}}\right)_i, i = a_{UT}+1 \cdots 2a_{UT}, \end{cases} \tag{3.25}$$

In this form, we define that $\mathbf{P}$ is the covariance matrix of the parameter $\mathbf{x}[n]$ and according to the next step of the Unscented Kalman filter, we also calculate the corresponding weight $\mathbf{w}$ by the following formula:

$$w[n] => \begin{cases} w[n]^{(0)}_{means} = \frac{\lambda}{a_{UT}+\lambda} \\ w[n]^{(0)}_{\text{cov}} = \frac{\lambda}{a_{UT}+\lambda} + (1-\alpha^2+\beta) \\ w[n]^{(i)}_{\text{cov}} = w[n]^{(i)}_{means} = \frac{\lambda}{2a_{UT}+2\lambda}, i = 1 \cdots 2a_{UT}, \end{cases} \tag{3.26}$$

where $\lambda = \alpha^2(a_{UT}+\kappa) - a_{UT}$. In the formula, λ is a scale factor used to decrease the error. α is the control factor for the distribution state of the unscented transformation. κ is to control the matrix $(a_{UT}+\lambda)\mathbf{P}$ as a Positive Semi-definite Matrix. β is a non-negative parameter to include the influence of higher-order terms. They are usually selected by experience, so they can be adjusted into different values under different different scenarios. By manipulating the above steps, we can obtain a series of points with identical means and variance to the original data. Next, we reform the data and the corresponding weight obtained from Eq.((3.25))and Eq. ((3.26)) in the following form:

$$\mathbf{x}^{(i)}(n) = \left[\begin{array}{ccc} \widehat{\mathbf{x}}(n) & \widehat{\mathbf{x}}(n) + \sqrt{(a_{UT}+\lambda)\mathbf{P}(n)} & \widehat{\mathbf{x}}(n) - \sqrt{(a_{UT}+\lambda)\mathbf{P}}(n) \end{array} \right] \tag{3.27}$$

$$\mathbf{P}(n+1 \mid n) = \sum_{i=0}^{2n} w^{(i)} \left[\widehat{\mathbf{x}}(n+1 \mid n) - \mathbf{x}^{(i)}(n+1 \mid n)\right] \left[\widehat{\mathbf{x}}(n+1 \mid n) - \mathbf{x}^{(i)}(n+1 \mid n)\right]^{\mathrm{T}} + \mathbf{Q} \tag{3.30}$$

$$\mathbf{x}^{(i)}(n+1 \mid n) = \mathbf{A}\mathbf{x}^{(i)}(n) \tag{3.28}$$

$$\widehat{\mathbf{x}}(n+1 \mid n) = \sum_{i=0}^{2a_{UT}} w^{(i)} \mathbf{x}^{(i)}(n+1 \mid n) \tag{3.29}$$

Where Eq.(3.27) defines the reformulated set of sigma points obtained from the Unscented Transformation, which preserves the statistical characteristics (mean and covariance) of the original state distribution. Eq.(3.28) Propagates each sigma point through the system dynamics using the state transition matrix A, thereby predicting the state evolution from time step n to n+1. Eq.(3.29) computes the predicted mean state by taking a weighted sum of the propagated sigma points, where the weights are defined to ensure unbiased estimation of the mean. Eq.(3.30) reformulates the associated weight matrix for the sigma points, which is subsequently used for calculating both the predicted mean and covariance in the Unscented Kalman Filter framework. With the above process, we can obtain the sigma points set and corresponding weights, the estimated variance matrix $\mathbf{P}(n+1 \mid n)$. Therefore, we calculate the sigma points set of the predicted value to obtain a new group of unscented transformation points $\mathbf{x}^{(i)}(n+1 \mid n)$, and then we can also get the measurement value based on the transformed parameters, so we can obtain the following part:

$$\begin{cases} \mathbf{x}^{(i)}(n+1 \mid n) = \Big[\widehat{\mathbf{x}}(n+1 \mid n) \\ \qquad\qquad \widehat{\mathbf{x}}(n+1 \mid n) + \sqrt{(a_{UT}+\lambda)\mathbf{P}(n+1 \mid n)} \\ \qquad\qquad \widehat{\mathbf{x}}(n+1 \mid n) - \sqrt{(a_{UT}+\lambda)\mathbf{P}(n+1 \mid n)}\Big], \\ \mathbf{\Theta}^{(i)}(n+1 \mid n) = \mathbf{h}\Big(\mathbf{x}^{(i)}(n+1 \mid n)\Big), \\ \overline{\mathbf{\Theta}}(n+1 \mid n) = \sum_{i=0}^{2n} w^{(i)}\, \mathbf{\Theta}^{(i)}(n+1 \mid n) \end{cases} \tag{3.31}$$

Next, we import 2 auxiliary parameters for the process, i.e. the matrix of the variance of the measurement argument and the covariance between the position parameters and the measurement parameter as follows:

$$\begin{cases} \mathbf{K}(n+1) = \mathbf{P}_{\mathbf{x\Theta}}(n+1)\mathbf{P}_{\mathbf{\Theta\Theta}}^{-1}(n+1) \\ \widehat{\mathbf{x}}(n+1) = \widehat{\mathbf{x}}(n+1 \mid n) + \mathbf{K}(n+1)\left[\mathbf{\Theta}(n+1) - \mathbf{h}\left[\mathbf{x}(n+1 \mid n)\right]\right] \\ \mathbf{P}(n+1) = \mathbf{P}(n+1 \mid n) - \mathbf{K}(n+1)\mathbf{P}_{\mathbf{\Theta\Theta}}(n+1)\mathbf{K}^{\mathrm{T}}(n+1) \end{cases} \tag{3.33}$$

$$\begin{cases} \mathbf{P}_{\mathbf{\Theta\Theta}}(n+1) = \sum_{i=0}^{2n} w^{(i)}\left[\mathbf{\Theta}^{(i)}(n+1 \mid n) - \overline{\mathbf{\Theta}}(n+1 \mid n)\right]\left[\mathbf{\Theta}^{(i)}(n+1 \mid n) - \overline{\mathbf{\Theta}}(n+1 \mid n)\right]^{T} + R \\ \mathbf{P}_{\mathbf{x\Theta}}(n+1) = \sum_{i=0}^{2n} w^{(i)}\left[\mathbf{x}^{(i)}(n+1 \mid n) - \overline{\mathbf{\Theta}}(n+1 \mid n)\right]\left[\mathbf{\Theta}^{(i)}(n+1 \mid n) - \overline{\mathbf{\Theta}}(n+1 \mid n)\right]^{\mathrm{T}} \end{cases} \tag{3.32}$$

Finally, we use the classic Kalman filter process to complete the prediction by calculating the Kalman gain and also complete the iterative process: where we predict the position velocity and acceleration information in $\widehat{\mathbf{x}}(n+1)$ in each time slot to obtain the vehicle information in a near real-time condition. The algorithm provided under Sections IV and V is summarized in Algorithm 1. It combines the model of the robust 2D-MUSIC model and UKF.

Unlike many existing beam tracking methods that employ the Kalman filter primarily for extrapolation based on prior motion models or rely on static road structure assumptions, our approach introduces a dynamic UKF formulation that directly incorporates real-time DoA estimates obtained via the MUSIC algorithm. This coupling between channel-observable features and state estimation provides two key improvements over traditional beam tracking approaches: (1) it enables real-time correction of vehicle motion states (position, velocity, and acceleration), reducing error accumulation common in dead-reckoning systems, and (2) it allows operation in scenarios without prior knowledge of road geometry or infrastructure layout. Furthermore, we propose an adaptive motion model that updates vehicle acceleration based on historical state transitions, improving prediction performance in curved or rapidly changing trajectories. These enhancements make our UKF framework more adaptable to realistic vehicular environments and communication constraints.

3.6 Numerical Results for LoS Scenario

The simulation runs MATLAB on the Windows 11 OS platform, and our main simulation parameters are summarized in Table 5.1.

Algorithm 1 Overall Vehicle State Estimation Algorithm

Require: Reference signals from V vehicles $\mathbf{s}(t)$;

Positions of RSUs PO_j^{RSU};

Search ranges for the MUSIC algorithm;

UKF parameters α and β;

Current vehicle state $\mathbf{x}[n]$.

Ensure: Estimated vehicle state for next time slot.

for each time slot n **do**

Receive reference signals and extract the corresponding part according to (3.13) and (3.14).

Compute covariance matrices of the received signal using (3.17) and (3.18).

Perform SVD as in (3.19) and (3.20) to obtain $\mathbf{V}^{\varphi}$ and $\mathbf{V}^{\theta}$.

Estimate the DoA (azimuth/elevation) using the MUSIC spectra in (3.21) and (3.22).

Generate sigma points using (3.25).

Compute sigma-point weights $\mathbf{w}$ using (3.26).

Predict state sigma points using (3.27)–(3.29).

Predict measurement sigma points using (3.27)–(3.30).

Compute predicted measurement and covariances via (3.31) and (3.32).

Update the state estimate and covariance using UKF step (3.33) to obtain $\mathbf{x}[n+1]$.

end for

Return: $\mathbf{x}[n+1]$

Table3.2: Simulation parameters.

Parameter	**Value**
Carrier frequency	28 GHz
Noise power density	−174 dBm/Hz
E_T	4
Time window	200 ms
Reference signal periodicity	Every 100 ms
RX height	7 m

3.6.1 MUSIC Algorithm Part Analysis

In this section, we will present the performance analysis of the MUSIC algorithm. We use a respective idea to decrease the dimension of the searching area, which can greatly legitimate the complexity of the algorithm, and from Figure 3.5, we can see that we choose 3 vehicles as the

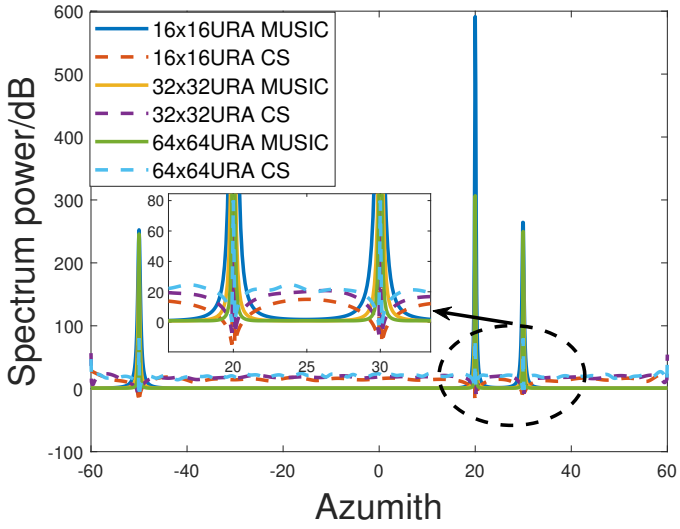


Fig.3.5: Azimuth estimation analysis using MUSIC and the compressive sensing algorithm under different antenna configurations.

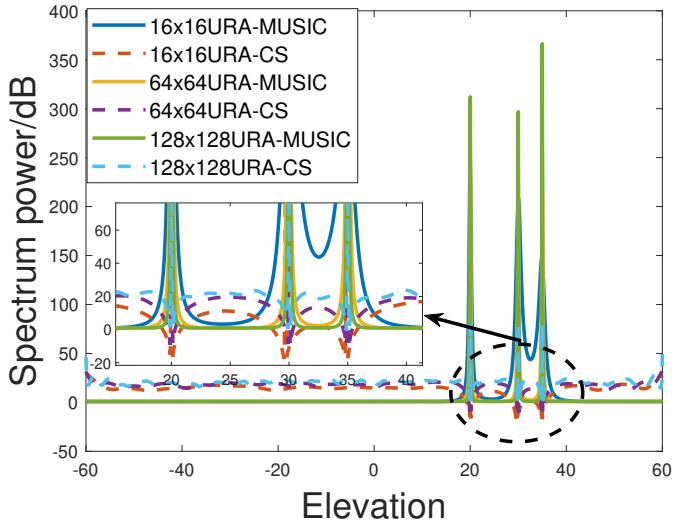


Fig.3.6: Elevation estimation analysis using MUSIC and the compressive sensing algorithm under different antenna configurations.

detection goals under the different scales of URA at the receiving end for the azimuth estimation. We compare the proposed MUSIC and compressive sensing methods in the DoA estimation. We set 16×16, 32×32, and 64×64 URA for the antenna amount to complete the assignment. From the result, we can see that under similar conditions, the CS method can also be adopted for the DoA estimation, while it will have similar complexity as the conventional MUSIC algorithm, which

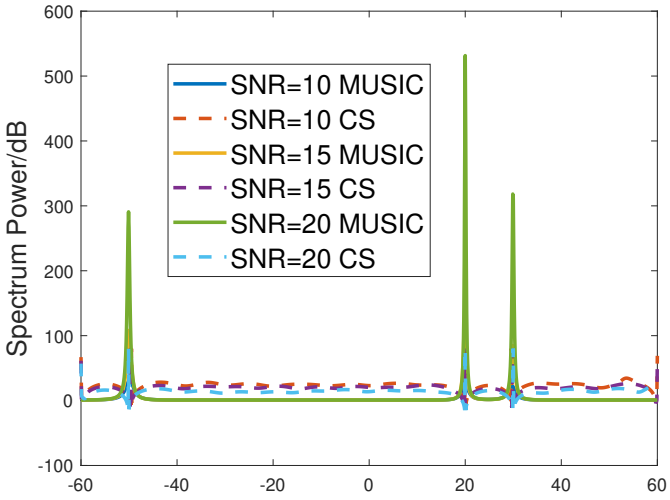


Fig.3.7: Azimuth estimation under different SNRs and searching scales using the MUSIC and compressive sensing algorithms.

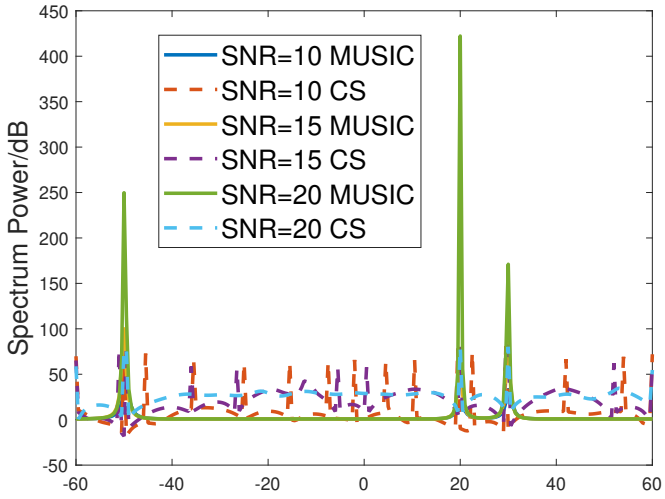


Fig.3.8: Elevation estimation under different SNRs and searching scales using the MUSIC and compressive sensing algorithms.

shows that we can achieve similar performance within in a 1D mode instead of a 2D mode. As for the antenna amount, it is obvious that when the amount of the receiving antennas becomes larger, the results will also get sharper when there are desired DoAs. We also give the elevation estimation results in a similar mode in the next picture, and the performance is extremely close.

Thus, we adjust the SNR to observe the influence of the DoA estimation. And to clarify the il-

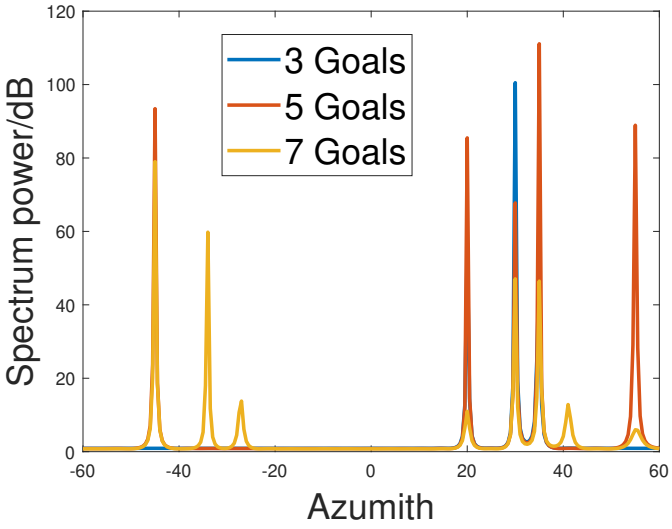


Fig.3.9: Illustration of the vehicle movement scenario.

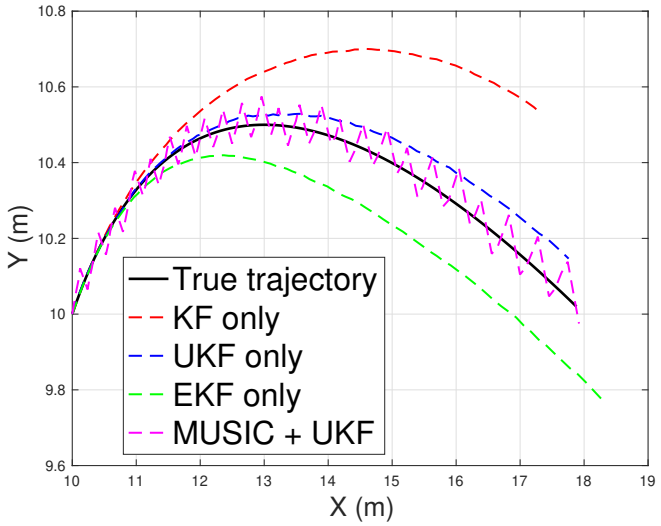


Fig.3.10: Position estimation under acceleration and curved trajectory during 200 time slots.

lustration, we just use the azimuth results to describe the results. From Figure 3.6, we set different conditions on the SNR for MUSIC and CS methods. We can see that under comparatively low SNR, neither the MUSIC nor the CS will be able to calculate the result sharply. However, when the SNR becomes larger, both algorithms will complete their function.

In the next Figures 3.7 and 3.8, we adjust the scale of the search area. In the previous simulation, we adopt the searching scale as 0.1 degrees in Figures 3.7 and in Figure 3.8 [12], we use a new scale of 0.5, and we can see that no matter how the SNR changes, the MUSIC algorithm will

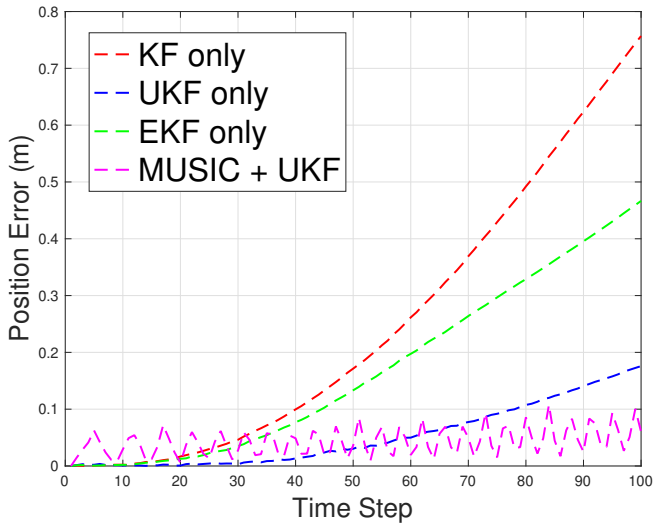


Fig.3.11: Position estimation error of the proposed method.

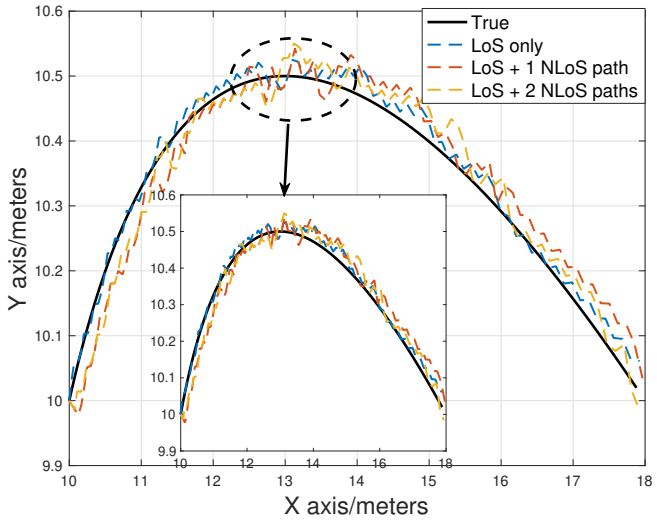


Fig.3.12: Vehicle trajectory under different channel propagation scenarios.

always get better performance when the scale becomes larger, some coherent signal may become overlap in the analysis results. So, it is better to give a smaller scale when the estimated angles are extremely close to each other.

In Figure 3.9, we give more resource origins, i.e., more vehicles, as the input of the reference signals. We set 3,5, and 7 goals for the angle estimation. Then, from this figure, we can see that the MUSIC algorithm will complete the DoA estimation while the goals become more. And the less the goals, the higher the peaks will become. It is reasonable for the system to use the same

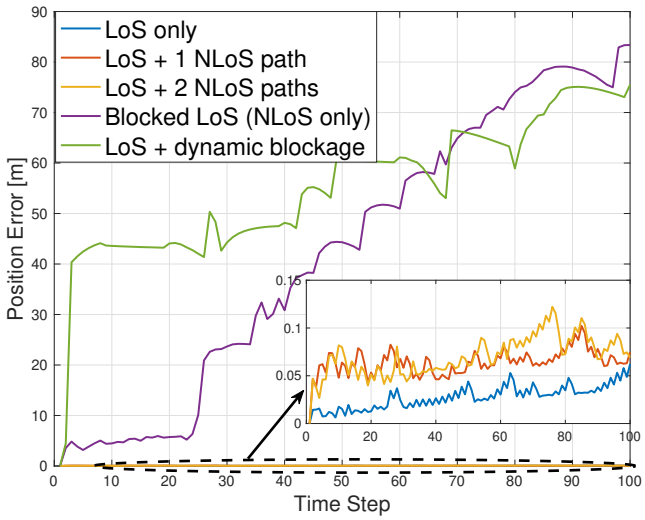


Fig.3.13: Position estimation error under different channel propagation scenarios.

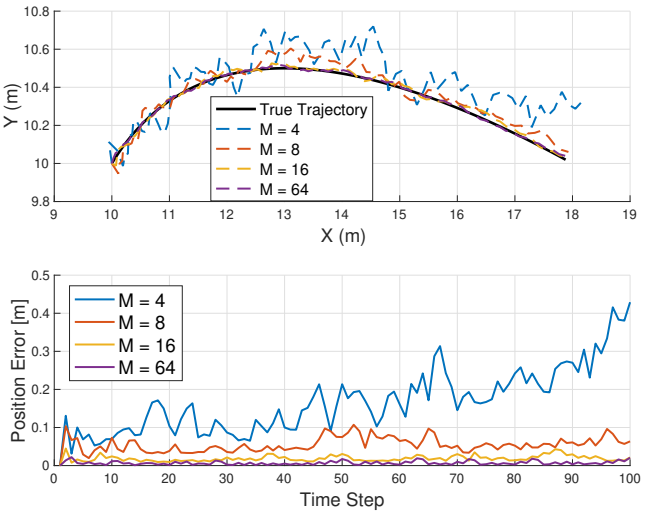


Fig.3.14: Elevation estimation performance under different antenna array sizes.

energy to complete the assignment.

3.6.2 Unscented Kalman Filter Simulation

In this section, we use the unscented Kalman filter to complete the velocity and position estimation for each vehicle. Previous work almost set the route as a straight line, but we give the scenario as a curve line for better performance analysis. As shown in Figs. 3.10 and 3.11, we compare four benchmark schemes under a dynamic scenario with acceleration and road curvature. These

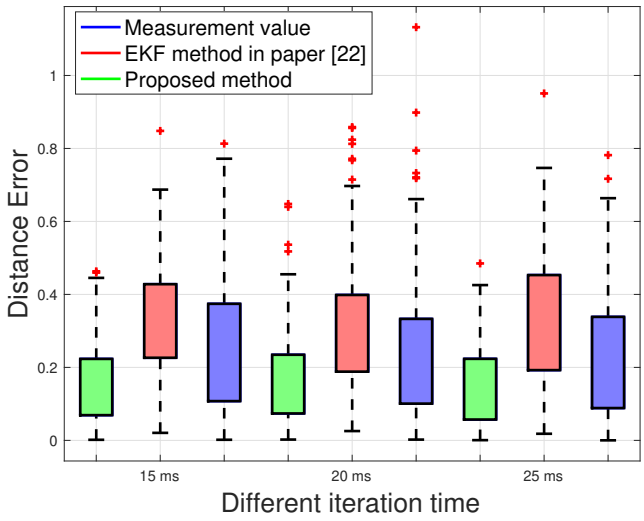


Fig.3.15: Boxplot of estimation error under different Kalman filter iteration numbers.

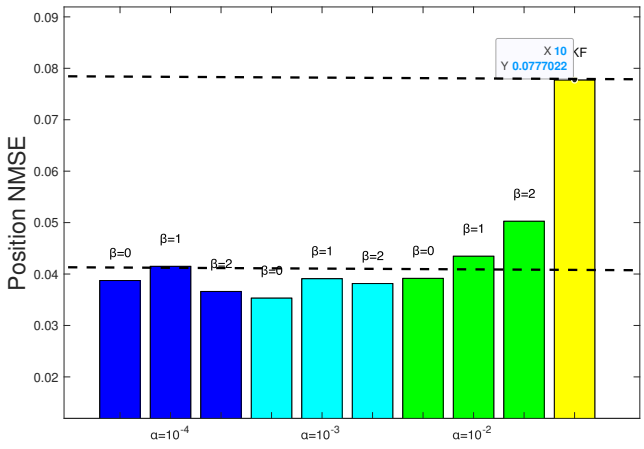


Fig.3.16: Estimation sensitivity under different UKF parameters α and β.

include **KF only** (Kalman Filter without any external feedback), **UKF only** (Unscented Kalman Filter used independently), **EKF only** (Extended Kalman Filter without observation corrections), and the proposed **MUSIC + UKF** approach. The proposed scheme leverages real-time DoA estimates from the MUSIC algorithm as external feedback to the UKF. This integration allows the system to adjust its state based on angle sensing at each time slot, effectively preventing error accumulation. In contrast, other methods, which rely solely on motion models and internal prediction, gradually accumulate errors over time, especially under nonlinear or dynamic motion conditions. The results clearly demonstrate that MUSIC-assisted UKF achieves superior tracking accuracy

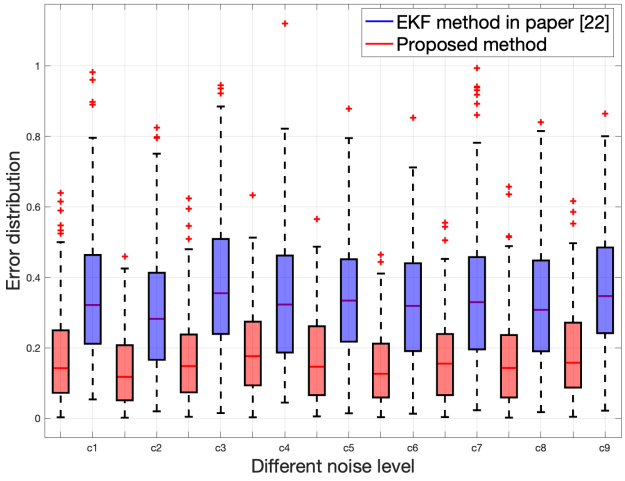


Fig.3.17: Positioning performance under different noise levels.

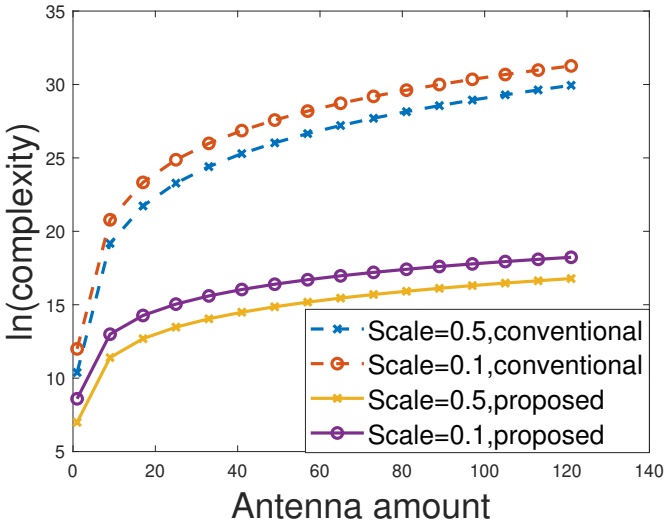


Fig.3.18: Computational complexity of the proposed algorithm compared with benchmark schemes.

and robustness, validating its effectiveness as a practical solution for vehicle localization. We give the corresponding boxplot under different iteration times (15, 20, and 25 ms, respectively.) in Figure 3.15.

Fig. 3.12 illustrates the vehicle trajectory under different channel conditions, including LoS only, LoS with one or two NLoS paths. Despite minor deviations, the proposed MUSIC+UKF framework is able to maintain robust tracking performance across all tested scenarios. As expected, the trajectory estimation remains closest to the ground truth in the pure LoS case, while

Table3.3: The 9 kinds of Noise level

R \ Q	**0.5Q**	**1Q**	**1.5Q**
0.5R	C1	C2	C3
1R	C4	C5	C6
1.5R	C7	C8	C9

the presence of additional NLoS paths slightly degrades estimation accuracy due to multipath-induced DoA errors. This demonstrates the method's resilience to moderate channel impairments.

Fig. 3.13 provides a more detailed view of the position error over time across five realistic channel scenarios: LoS only, LoS with 1 NLoS path, LoS with 2 NLoS paths, completely blocked LoS (NLoS only), and LoS with dynamic blockage. The results show that the proposed approach performs consistently well under mild multipath conditions. However, in the absence of LoS or when temporary blockages occur, DoA estimation becomes unreliable, resulting in significant performance degradation. This highlights the strong dependency of the system on reliable DoA input, motivating future work on hybrid methods that combine DoA and other features such as ToA or motion prediction under severe blockage.

Fig. 3.14 presents the impact of antenna array size ($M = 4, 8, 16, 64$) on trajectory estimation accuracy. As shown in the figure, larger antenna arrays result in significantly improved elevation tracking and reduced positioning error. This is due to the enhanced angular resolution and array gain, which allows MUSIC to achieve more accurate DoA estimation. Notably, the position error for $M = 64$ remains below 0.05 m throughout the simulation, while the error for $M = 4$ fluctuates more severely. These results confirm that array size plays a critical role in maintaining high-precision tracking in mmWave vehicular scenarios.

In Fig. 3.16, we adjust the parameters in the unscented Kalman filter, i.e., the parameter α, β, and the results of the extended Kalman filter in similar conditions. It can be seen that the parameters have a small influence on the performance, and the results are always better no matter how the parameters change.

In addition, we analyze the results and performance under different noise levels for the proposed unscented Kalman filter method. We give 10 different noise conditions named from c1 to c10, as shown in Fig. 3.17. The noise level from c1 to c10 is becoming worse overall, as shown in the form. 3, while the proposed unscented method always works better than the EKF method when they have similar noise levels. We also give the boxplot in the simulation figure to demonstrate the results.

Table3.4: The complexity of the MUSIC algorithm.

Method	Complexity
Proposed method	$O\left(\left(V+\frac{1}{\text{scale}}\right)(L_R^2+W_R^2)+(L_R^3+W_R^3)\right)$
Conventional method	$O\left(\left(V+\frac{1}{\text{scale}}\right)(L_RW_R)^2+(L_RW_R)^3\right)$

3.6.3 Complexity Analysis

In this section, we present the complexity of our MUSIC algorithm and Kalman filter algorithm, respectively.

First, we give the complexity of the MUSIC algorithm, it can be seen as the joint complexity of the autocorrelation matrix computation, singular value decomposition (SVD), and identifying the peaks that represent the number of source signals within the spectrum, which allows us to determine the DoA. We give the complexity of the comparison of our MUSIC algorithm and conventional algorithm in Table. IV and Fig. 3.18, we use the logarithm to depict the complexity for better observation than conventional idea. From the figure, we can see that when the antenna amount becomes larger (from 1 to 128), the result will greatly increase, and also, the smaller the scale is, the more numerous the complexity will be.

Next, as the UKF part, for the first part, we select $2a_{UT}$ + 1 sigma points and propagate them through the nonlinear system model. The computation for each sigma point is $O(a_{UT})$, therefore the total complexity is approximately $O(a_{UT}^2)$. Then, the analysis of the prediction step includes the calculation of the predicted covariance matrix, involving the weighted sum of each sigma point, with a complexity of $O(a_{UT}^2)$. For the Update Step, the calculation of the predicted measurement covariance matrix and the cross-covariance matrix. This involves *mea* observation variables and $2a_{UT}+1$ sigma points, with a complexity of $O(mea \times a_{UT}^2)$. Additionally, there is the inversion of an $mea \times mea$ matrix, which has a complexity of $O(mea^3)$. Overall, the total complexity of the UKF is similarly affected by $O(a_{UT}^2) + O(mea \times a_{UT}^2) + O(mea^3)$.

Chapter 4

RIS-Assisted OTFS-Based Robust Localization in NLoS Environments

4.1 Overview of the Proposed NLoS Localization Framework

with the development of 6G wireless communication technologies, high mobility scenarios such as vehicle-to-everything (V2X) communication require more robust and accurate methods for position and velocity estimation [92, 93, 94, 95]. Positioning and speed estimation are fundamental components of V2X communication systems, supporting critical applications such as cooperative driving, collision avoidance, and autonomous navigation. Traditional positioning methods primarily rely on Global Positioning System (GPS) signals, which can achieve acceptable accuracy under open-sky conditions. However, in urban environments or scenarios involving tunnels, high-rise buildings, or non-line-of-sight (NLoS) propagation, GPS-based solutions suffer from severe signal degradation. In addition, channel estimation and mobility management become increasingly difficult in high-speed vehicular environments, especially when the communication links are disrupted or unreliable. To address these challenges, Integrated Sensing and Communication (ISAC) [96] has emerged as a promising paradigm that combines wireless communication and sensing capabilities within the same platform. ISAC enables simultaneous data transmission and environmental sensing, providing a highly efficient approach for vehicle localization and mobility management in dynamic scenarios [97].

In this context, Reconfigurable Intelligent Surfaces (RIS), as a key enabler for ISAC systems, have received considerable attention for their ability to reconfigure the wireless propagation environment by dynamically adjusting the phase shifts of reflected signals. This capability allows RIS to mitigate signal propagation challenges, especially in nonline-of-sight (NLoS) conditions, where conventional GPS is still challenging. Existing research shows that RIS can effectively

address NLoS issues by reflecting signals toward the intended receiver, creating virtual LoS paths and improving both location accuracy and communication reliability. The integration of RIS with ISAC systems further enhances overall performance by leveraging the environmental reconfiguration capabilities of RIS with the unified sensing and communication framework of ISAC. This combination provides a powerful solution for highly mobile V2X applications. On the other hand, high-speed scenarios introduce severe fading effects and Doppler shifts that degrade the performance of traditional communication systems. Orthogonal Time Frequency Space (OTFS) [98], a modulation technique designed for the delay-Doppler (DD) domain, has demonstrated robustness against such fading and Doppler effects. By spreading information symbols over both time and frequency domains, OTFS allows better utilization of multipath diversity. The combination of RIS with OTFS offers a promising approach to simultaneously reconfigure the propagation environment and exploit DD diversity, enabling robust vehicle position and velocity estimation even under challenging NLoS conditions [50].

4.1.1 Contributions

In this work, we propose a framework to improve the accuracy of vehicle velocity and position estimation under NLoS conditions, especially when GPS is unavailable. The proposed framework leverages ISAC and incorporates both communication and sensing functionalities. Specifically, the proposed framework employs the MUSIC algorithm for initial angle of arrival (AoA) estimation, followed by two methods, transmitting and Kalman filter (the communication method and the sensing method), to obtain vehicle velocity. For the communication approach, OTFS modulation enables the vehicle to transmit velocity information to the base station (BS) as a source of estimate. On the other hand, for the sensing approach, an unscented Kalman filter (UKF) tracks velocity and position using reference signals transmitted by the vehicle as another source. We will use these two methods to estimate our velocity, improving the reliability of vehicle positioning and velocity estimation in V2X scenarios. In addition, we explore various modulation techniques such as Zero-Padding (ZP), Cyclic Prefix (CP), and their recursive variants to show that the OTFS framework outperforms OFDM in this context. We propose a novel velocity-carried low peak-to-average power ratio (PAPR) frame structure within the OTFS framework to support the robust velocity estimation method. Despite significant progress in vehicular localization techniques, many existing approaches face key limitations. First, methods based solely on GPS are highly vulnerable to blockage and multipath effects. Second, radar- or LiDAR-based positioning systems, while precise, often require additional hardware. Third, existing frameworks typically focus on either positioning or speed estimation independently, lacking a joint and unified solution.

Table4.1: Summary of Notations in NLoS scenario.

Symbol	Description	Symbol	Description
$\mathbf{P}_B = (x_B, y_B, z_B)$	Position of BS	$\mathbf{P}_R = (x_R, y_R, z_R)$	Position of RIS
$\mathbf{P}_V = (x_V, y_V, z_V)$	Position of the vehicle	$\mathbf{X}[l, k]$	Transmitted DD domain signal
$\mathbf{X}_{tf}[m, n]$	Time–frequency domain signal	$s(t)$	Time-domain transmitted signal
h_p	Channel gain	v_p^h	Doppler shift of the path
τ_p^h	Delay of the channel path	θ^{AOD}	Elevation angle (RIS $\rightarrow$ BS)
ψ^{AOD}	Azimuth angle (RIS $\rightarrow$ BS)	θ^{AOA}	Elevation angle (RIS $\rightarrow$ Vehicle)
ψ^{AOA}	Azimuth angle (RIS $\rightarrow$ Vehicle)	$\mathbf{r}^{RIS}(t)$	Received signal at RIS
$\mathbf{a}(\theta_p^{AOA}, \phi_p^{AOA})$	Steering vector of AOA	$r(t)$	Received signal at BS
$Y(f, t)$	Time–frequency domain received signal	$\mathbf{Y}[m, n]$	DD domain received signal
$\mathbf{A}$	Transition matrix in UKF	$\mathbf{x}[n]$	State vector at time slot n
$\mathbf{P}$	State covariance matrix	$\mathbf{K}(n+1)$	Kalman gain
α	UKF scaling parameter 1	β	UKF scaling parameter 2
(v_x, v_y, v_z)	Vehicle velocity in 3D	(a_x, a_y, a_z)	Vehicle acceleration in 3D
$\omega[n]$	Sigma point weight	$\lambda[n]$	UKF scaling factor

These challenges underscore the need for a robust and integrated framework capable of addressing both localization and velocity estimation under practical and adverse conditions. To the best of our knowledge, this is the first work to utilize a pilot signal, distinct from the embedded pilot, while addressing PAPR concerns in velocity position and velocity tracking within an OTFS system. In summary, the contribution of this paper can be summarized as follows:

- Propose a complete solution in the NLoS path to detect the position of the vehicle in a non-GPS environment based on RIS and OTFS modulation.
- We investigate ZP, CP, and their reduced variants (RZP/RCP) to study the trade-offs among BER, padding length, and also focus on the peak-to-average power ratio (PAPR) of our signals for better transmission.
- Design a two-branch velocity estimation framework that fuses direct velocity transmission and UKF tracking, enabling robust and accurate positioning even under severe Doppler and blockage.
- Present a comprehensive comparison of our method with OFDM in terms of BER. Additionally, evaluate NMSE and PAPR by comparing our low PAPR method with the traditional embedded pilot scheme. Also, analyze the tracking performance enhanced by the UKF through numerical results.

Table4.2: List of abbreviations used in the NLoS part

Abbreviation	Meaning	Abbreviation	Meaning
AoA	Angle of Arrival	AoD	Angle of Departure
BS	Base Station	CP	Cyclic Prefix
CRLB	Cramér–Rao Lower Bound	DD	Delay–Doppler
DFT	Discrete Fourier Transform	EKF	Extended Kalman Filter
FFT	Fast Fourier Transform	GPS	Global Positioning System
ISAC	Integrated Sensing and Communication	LoS	Line-of-Sight
MIMO	Multiple Input Multiple Output	MMSE	Minimum Mean Square Error
MRC	Maximum Ratio Combining	NLoS	Non-Line-of-Sight
NMSE	Normalized Mean Square Error	OFDM	Orthogonal Frequency Division Multiplexing
OMP	Orthogonal Matching Pursuit	OTFS	Orthogonal Time Frequency Space
PAPR	Peak-to-Average Power Ratio	QAM	Quadrature Amplitude Modulation
RCP	Repeated Cyclic Prefix	RIS	Reconfigurable Intelligent Surface
RZP	Repeated Zero Padding	SNR	Signal-to-Noise Ratio
TF	Time–Frequency	UKF	Unscented Kalman Filter
V2X	Vehicle-to-Everything	ZP	Zero Padding

4.2 System and Channel Model

In this section, we explain our system models and their roles. We also provide the main parameters in Table 4.1. And also to improve readability and clarity, we have added a table that organizes all abbreviations used in the NLoS Scenario as Table 4.2.

4.2.1 System Description

We consider an uplink scenario for the RIS-assisted channel model as shown in Fig. 4.1. We assume that the BS and the vehicle have one single antenna and the RIS has a uniform rectangular element array $M_1 \times M_2$. The goal is to get the velocity and location of the vehicle when the GPS is not working. We have vehicle, RIS, and BSs in our model; we give their definition and description as follows:

Vehicle: The vehicle wants to transmit its positions and velocities to the BS when the GPS is not working, so it needs to transmit a signal to the BS and let the BS detect its velocities and positions. In addition, some obvious obstacles prevent the LoS signal from reaching the vehicle from the BS. Therefore, the signals have to be transmitted through a RIS. The signal can be divided into the reference signal and the velocity data.

RIS: The RIS, that is, the reconfigurable intelligent surface that is controlled by the programmable controller (to analyze the received signals and control to resend them to the BS) that can receive and transmit signals from one end to another. Our system uses them to reconfigure

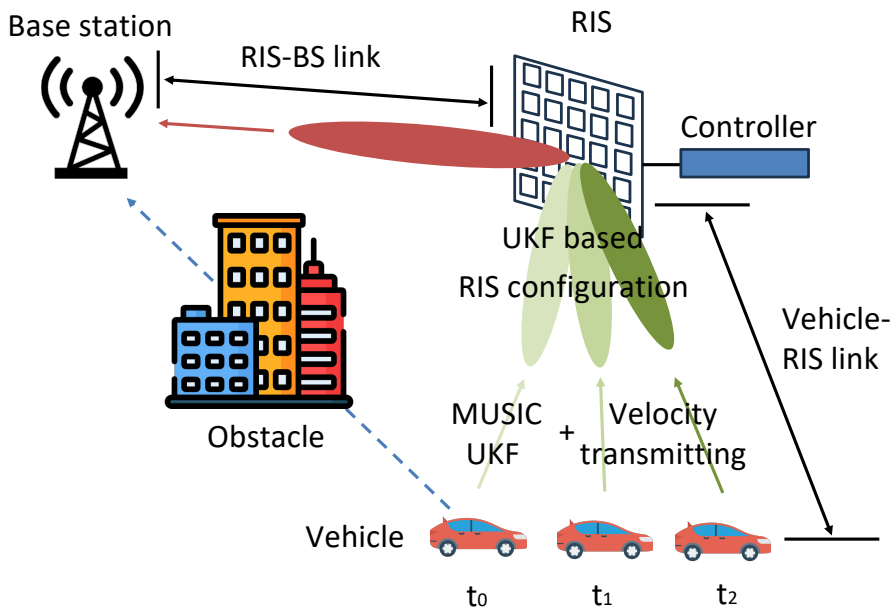


Fig.4.1: Framework of the NLoS scenario.

the signal from vehicle to BS. We need to note that Compared to relays or active BSs, RIS offers much lower power consumption, cost, and hardware complexity, making it more suitable for scalable deployment in dense or coverage-challenged V2X environments. In addition, we assume the RIS as a hybrid RIS architecture, where part of the RIS elements are equipped with minimal active components. These active elements allow for basic signal processing tasks, such as signal extraction or feedback to the BS, while the remaining elements operate passively to maintain overall energy efficiency. This hybrid configuration strikes a balance between practical feasibility and system functionality. Moreover, a relay introduces additional noise and latency, while RIS preserves the signal power through intelligent reflection.

In addition, since the positions of the BS and RIS are fixed and known, the AoD from RIS to BS can be calculated in advance. Therefore, the only unknown angle is the AoA from the vehicle to the RIS, which we estimate using the RIS array. This makes MUSIC-based estimation feasible and practical even in a single-antenna transceiver setting.That said, we assume a deterministic LoS channel between the BS and the RIS primarily as a modeling simplification as a Rank-1 channel [54],[55].

BS: The BS receives a signal from the RIS in the uplink channel and then completes all the

signal processing and calculates the position from the signals.

4.2.2 General Process Model in OTFS under RIS

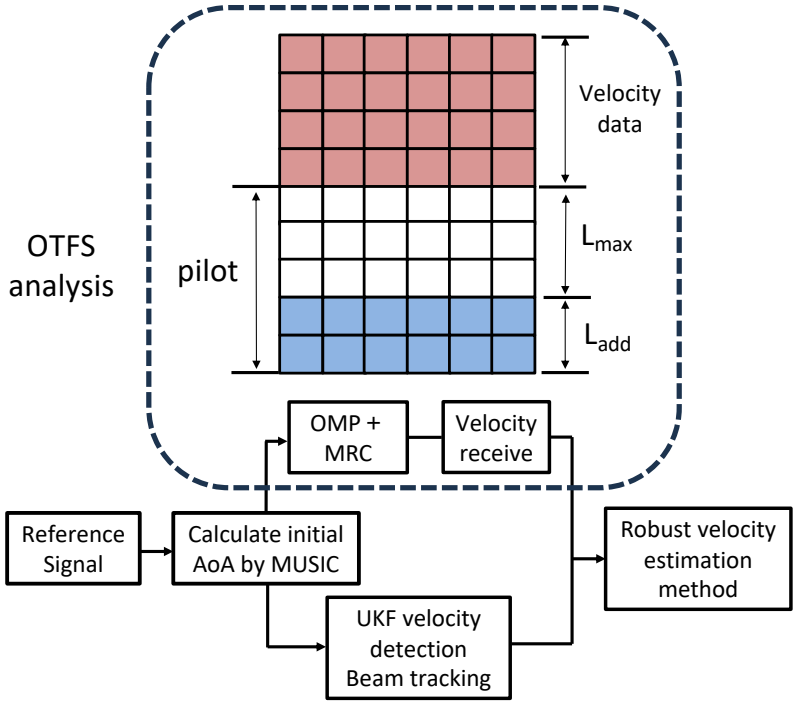


Fig.4.2: Flowchart of the NLoS process.

We define the position of the BS, RIS and vehicle as $\mathbf{P}_B = (x_B, y_B, z_B)$, $\mathbf{P}_R = (x_R, y_R, z_R)$ and $\mathbf{P}_V = (x_V, y_V, z_V)$, respectively. We describe the scenario of vehicle-RIS and RIS-BS links progress, respectively, as shown in Fig. 4.2. The two-dimensional grid in the figure represents the OTFS resource allocation in the delay–Doppler domain. Specifically, the horizontal axis corresponds to the Doppler bins, which is directly related to the relative velocity of the vehicle, while the vertical axis represents the delay bins, corresponding to the propagation delay of the channel paths. Each grid element denotes one OTFS resource block occupying a specific delay–Doppler location. At the transmitter, a sequence of bits is first mapped onto a two-dimensional (2D) grid in the DD domain, with dimensions $M \times N$, where M and N are the number of delay and Doppler bins, respectively. First, we have the delay-Doppler domain signal, denoted by $\mathbf{X}[l, k]$, which can be transformed into a TF domain signal by inverse symplectic fast Fourier transform (ISFFT) as

follows:

$$\mathbf{X}_{tf}[m,n] = \frac{1}{\sqrt{NM}} \sum_{l=0}^{N-1} \sum_{k=0}^{M-1} \mathbf{X}[l,k] e^{j2\pi\left(\frac{nl}{N} - \frac{mk}{M}\right)}, \tag{4.1}$$

where $x[k,l]$ is the QAM symbols and $l = 0,\ldots,M-1, k = 0,\ldots,N-1$ stand for the delay and Doppler domain index, and $\mathbf{X}_{tf} \in \mathbb{C}^{M\times N}$ is the TF domain transmitted samples matrix. The ISFFT is a 2D transformation that performs an M point discrete Fourier transformation (DFT) on the columns of $\mathbf{X}_{tf}$ and an N point inverse discrete Fourier transformation (IDFT) on the rows of $\mathbf{X}_{tf}$. Furthermore, in the familiar TF domain, we can have the following relationship:

$$\mathbf{Y}_{\text{tf}}[m,n] = \mathbf{H}_{\text{tf}}[m,n]\mathbf{X}_{\text{tf}}[m,n], \tag{4.2}$$

where $\mathbf{H}_{\text{tf}}[m,n] = \sum_l \sum_k h[l,k] e^{j2\pi\left(\frac{nk}{N} - \frac{ml}{M}\right)}$. The $\mathbf{H}_{\text{tf}}[m,n]$ and $\mathbf{h}[l,k]$ are the TF and DD domain channel models, respectively. For the TF domain signal, we can simply transform it into the TF by using the Heisenberg transform with the help of a transmit pulse $g_{\text{tx}}(t-nT)$ as

$$s(t) = \sum_{k=0}^{N-1} \sum_{l=0}^{M-1} \mathbf{X}_{\text{tf}}[m,n] g_{\text{tx}}(t-nT) e^{j2\pi n\Delta f(t-mT)}, \tag{4.3}$$

and the above operation can be considered in the literature as the Heisenberg transform, which requires the parameters of N, M and $g_{\text{tx}}(t-nT)$.

The signal is then from the vehicle-RIS channel, and after transmitting to RIS, we can express the received signal $\mathbf{r}^{\text{RIS}}(t)$ on the RIS side as

$$\mathbf{r}^{\text{RIS}}(t) = \sum_{p=1}^{P_1} h_p e^{j2\pi v_p^h\left(t-\tau_p^h\right)} s\left(t-\tau_p^h\right) \mathbf{a}\left(\theta_p^{\text{AOA}}, \phi_p^{\text{AOA}}\right), \tag{4.4}$$

where the P_1 is the amount of path in the vehicle-RIS link. h_p, v_p^h and τ_p^h are the channel gain, Doppler shift and delay shift of this channel between the vehicle and the RIS. θ_p^{AOA} and ϕ_p^{AOA} are the elevation and azimuth angles of arrival in the p-th path, respectively. As for denoting the steering vectors $\mathbf{a}(\theta_p^{\text{AOA}}, \phi_p^{\text{AOA}})$, it can be expressed as follows:

$$\mathbf{a}(\theta_p^{\text{AOA}}, \phi_p^{\text{AOA}}) = \mathbf{a}_x(\theta_p^{\text{AOA}}, \phi_p^{\text{AOA}}) \otimes \mathbf{a}_y(\theta_p^{\text{AOA}}, \phi_p^{\text{AOA}})), \tag{4.5}$$

Then the vertical and horizontal AoA in the x and y axes can be expressed as follows [99]:

$$\begin{aligned} \mathbf{a}_x(\theta_p^{\text{AOA}}, \phi_p^{\text{AOA}}) &= e^{-j2\pi\mathbf{m}_1 \frac{d}{\lambda} \sin(\phi_p^{\text{AOA}}) \sin(\theta_p^{\text{AOA}})} \\ \mathbf{a}_y(\theta_p^{\text{AOA}}, \phi_p^{\text{AOA}}) &= e^{-j2\pi\mathbf{m}_2 \frac{d}{\lambda} \sin(\phi_p^{\text{AOA}}) \cos(\theta_p^{\text{AOA}})}. \end{aligned} \tag{4.6}$$

where $\mathbf{m}_1 = [0, 1, \ldots, M_1 - 1]$ and $\mathbf{m}_2 = [0, 1, \ldots, M_2 - 1]$, and we have d as the antenna spacing which $d = \lambda/2$. Then we can get the received signal at the BS side as follows:

$$\begin{aligned} r(t) &= \sum_{q=1}^{P_1} g_q \boldsymbol{\phi}^{\mathrm{T}} \operatorname{diag}\left(\mathbf{a}^H\left(\theta_q^{\mathrm{AOD}}, \psi_q^{\mathrm{AOD}}\right)\right) \mathbf{r}^{\mathrm{RIS}}\left(t - \tau_q^g\right) + w(t) \\ &= \sum_{q=1}^{P_1}\sum_{p=1}^{P_2} g_q h_p \boldsymbol{\phi}^{\mathrm{T}} \operatorname{diag}\left(\mathbf{a}^H\left(\theta_q^{\mathrm{AOD}}, \psi_q^{\mathrm{AOD}}\right)\right) \\ &\quad \mathbf{a}\left(\theta_p^{\mathrm{AOA}}, \psi_p^{\mathrm{AOA}}\right) e^{j2\pi v_p^h\left(t-\tau_p^h-\tau_q^g\right)} s\left(t - \tau_p^h - \tau_q^g\right) \\ &\quad + w(t), \end{aligned} \tag{4.7}$$

where g_q and $w(t)$ are the channel gain and the noise in the RIS-BS link, and we have the θ^{AOD} and ψ^{AOD}, also the θ^{AOA} and ψ^{AOA} can be expressed respectively as

$$\begin{aligned} \theta^{\mathrm{AOD}} &= \arctan \frac{\sqrt{(x_B - x_R)^2 + (y_B - y_R)^2}}{z_R - z_B} \\ \psi^{\mathrm{AOD}} &= \arctan \frac{y_B - y_R}{x_B - x_R}, \end{aligned} \tag{4.8}$$

$$\begin{aligned} \theta^{\mathrm{AOA}} &= \arctan \frac{\sqrt{(x_V - x_R)^2 + (y_V - y_R)^2}}{z_V - z_R} \\ \psi^{\mathrm{AOA}} &= \arctan \frac{y_V - y_R}{x_V - x_R}, \end{aligned} \tag{4.9}$$

and the $\boldsymbol{\phi}$ can be expressed as

$$\boldsymbol{\phi} = [\phi_1, \ldots, \phi_{M_r}]^{\mathrm{T}}, \tag{4.10}$$

where $\dot{\phi}_{m_r} = \beta_{m_r} e^{j\omega_{m_r}}$, and in the equation β_{m_r} and ω_{m_r} denote the amplitude and phase shift of the m_r-th element in RIS.

Without loss of generality, we assume that the positions of BS and RIS are perfectly known, and we also assume that there is no scattering during BS and RIS, since they are located at relatively high places [100]. So we have that $P_1 = 1$, and because of this, all angels in the RIS-BS link can be calculated directly, so the RIS-BS link part parameters can be seen as some constants, and as for the transmission delay shift in the RIS-BS link, since the distance is perfectly known by the system, we can derive $\tau_q^g = \frac{\|\mathbf{p}_B - \mathbf{p}_R\|^2}{c}$, and then we can rewrite the received signal as

$$r(t) = \sum_{p=1}^{P_2} h_p \mathbf{C} s\left(t - \tau_p^h - \tau_q^g\right) \mathbf{a}\left(\theta_p^{AOA}, \psi_p^{AOA}\right) + n_0(t), \tag{4.11}$$

where

$$\mathbf{C} = g_q \phi^T \operatorname{diag}\left(\mathbf{a}\left(\theta_q^{AOD}, \psi_q^{AOD}\right)\right), \tag{4.12}$$

where g_q and τ_q^g are the DD-domain channel response and the delay shift of the q-th path in the link between RIS and BS, respectively, and since $q = 1$ and the channel is perfectly known, we then turn mainly to the analysis of the RIS-vehicle link. Let θ_q^{AOD} and ψ_q^{AOD} represent the elevation and azimuth departure angles between the BS and the RIS, respectively. Then we continue with the demodulation process. We can obtain the received signal in the TF domain, i.e., computing the cross-ambiguity function [101] as

$$Y(f,t) = A_{g_{\mathrm{rx}},r}(f,t) \triangleq \int r(t')\, g_{\mathrm{rx}}^*(t'-t)\, e^{-j2\pi f(t'-t)} dt', \tag{4.13}$$

where $\mathbf{Y}_{\mathrm{tf}}[l,k] = Y(f,t)|_{f=l\Delta f, t=kT}$. We can calculate the received DD domain signal $\mathbf{Y}[m,n]$ as

$$\mathbf{Y}[m,n] = \frac{1}{\sqrt{NM}} \sum_{k=0}^{N-1} \sum_{l=0}^{M-1} \mathbf{Y}_{\mathrm{tf}}[l,k] e^{-j2\pi\left(\frac{nk}{N} - \frac{ml}{M}\right)}. \tag{4.14}$$

For the latter part, we divide the channel estimation into two parts: gain, delay, and Doppler, that is, the channel part based on a low PAPR velocity-based estimation method and the angle estimation method armed with the MUSIC algorithm. It is worth noting that since the link from the RIS to the BS has a fixed location, we assume that we can directly transmit the signal from the RIS to the BS extremely easily. Therefore, we will mainly analyze the part between the vehicle and the RIS, and we will start our channel estimation analysis mainly from (4.4).

4.2.3 RIS Configuration

We use the angle of arrival, which is best suited for tracking the vehicle when receiving signals from the vehicle. During the channel training phase, as suggested in [102], the phase vectors in RIS are chosen to match the columns of the DFT matrix to minimize channel estimation errors. In the data transmission phase, optimizing the RIS phase shifts improves the signal quality at the BS. The overall objective is to maximize the sum rate, which translates into a RIS beam tracking optimization problem formulated as follows:

$$\begin{aligned} &(\mathrm{P1}): \max_{\boldsymbol{\phi}} \sum_{q=1}^{P_2} \sum_{p=1}^{P_1} \log_2\left(1+\rho_{p,q}\right) \\ &\text{s.t. } \left|\phi_{m_r}\right| = 1, \forall m_r = 1,2,\ldots,M_r, \end{aligned} \tag{4.15}$$

where we have $\rho_{p,q} = P_t \left\|\boldsymbol{\phi}^{\mathrm{T}} \mathbf{h}_{pq}\right\|^2 / \sigma^2$ and P_t is the transmit power, and we have $\mathbf{h}_{pq} = g_q h_p \,\mathrm{diag}\left(\mathbf{a}^H\left(\theta_q^{\mathrm{AOD}}, \psi_q^{\mathrm{AOD}}\right)\right) \mathbf{a}\left(\theta_p^{\mathrm{AOA}}, \psi_p^{\mathrm{AOA}}\right)$. When we have the path amounts $P_1 = 1$ and $P_2 = 1$, the optimal phase-shift solution for solving problem (P1) is $\boldsymbol{\phi}^\star = \left[\mathrm{diag}\left(\mathbf{a}^H\left(\theta^{\mathrm{AOD}}, \psi^{\mathrm{AOD}}\right)\right) \mathbf{a}\left(\theta^{\mathrm{AOA}}, \psi^{\mathrm{AOA}}\right)\right]^*$. It is worth noting that the ideal solution to (P1) would

involve compensating for the phase of all paths in the vehicle–RIS–BS link to steer the signal in the desired direction. However, this is impractical because a single-phase vector cannot simultaneously compensate for all paths. However, the presence of multipath is considered, the RIS phase vector optimization becomes a non-concave problem, making it difficult to solve directly. Since this part is not the main part of our work, we adopt this solution directly by considering the strongest path in the DD domain and then tracking that direction as the main direction.

4.3 Channel Estimation Method

In this section, we give the background of the OTFS variant and specifically propose our channel estimation model. First, we illustrate the OTFS variant design and the AoA estimation using the MUSIC algorithm as the basic condition, and then give the low PAPR channel estimation method to complete the channel estimation and obtain the transmitted velocity. In the next part, we complete the beam tracking and velocity estimation using UKF, and finally we use the robust velocity estimation to guarantee the better correctness of our velocity.

4.3.1 OTFS Variant Design

In our scenario, with the help of RIS, the OTFS variant design improves signal transmission and helps BS locate the vehicle accurately. To achieve this, we explore several effective OTFS variant schemes.

Two widely used methods for padding each OTFS sub-symbol are the Cyclic Prefix (CP) and the Zero Padding (ZP). The CP method adds padding at the beginning of each sub-symbol by copying and appending the final samples of the corresponding subsymbol to its front. In contrast, the ZP method adds paddles at the end of each sub-symbol by appending zeros instead of duplicating samples. For additional methods like Reduced ZP (RZP) and Reduced CP (RCP), padding is applied either before or after the entire symbol sequence rather than after each individual sub-symbol.

To illustrate these variant methods of OTFS, Fig. 4.3 provides a clear representation of each padding approach, showing how CP, ZP, RZP and RCP differ in structure and functionality. Each cell in Fig. 4.3 represents a resource block in the delay-Doppler (DD) domain and later in this paper, The two-dimensional grid in the figure represents the OTFS resource allocation in the delay–Doppler domain. Specifically, the horizontal axis corresponds to the Doppler bins, which is directly related to the relative velocity of the vehicle, while the vertical axis represents the delay

bins, corresponding to the propagation delay of the channel paths. We will present simulation results comparing these variant modulations, providing a specific analysis of their performance in RIS-aided OTFS transmission. In the design of the OTFS system, the selection of the pilot frame structure significantly affects key performance metrics such as spectral efficiency, transmit power, channel estimation complexity, and detection robustness. Based on the reference [101], four common pilot schemes—Cyclic Prefix (CP), Zero Padding (ZP), Repeated CP (RCP), and Repeated ZP (RZP)—each exhibit distinct trade-offs.

CP-OTFS adds a cyclic prefix (CP) per block. While this allows for straightforward equalization and time-invariant convolution modeling, it incurs additional energy consumption and lowers spectral efficiency due to per-block overhead.

ZP-OTFS uses zero padding instead of a CP. This ensures the lowest transmit power and leads to the sparsest effective channel matrix, facilitating low-complexity detection and sparse estimation. However, it can be sensitive to synchronization and may suffer from edge leakage unless properly designed.

RCP-OTFS employs a CP per frame, improving spectral efficiency compared to CP-OTFS. The channel sparsity remains similar to that of CP-OTFS, but frame-level CP may reduce flexibility for block-wise processing.

RZP-OTFS uses ZP per frame. This approach balances power efficiency with higher spectral efficiency. However, the effective channel matrix becomes less sparse due to the frame-wise structure, especially when the top-right submatrices become full, increasing the complexity of the estimation. By investigating these modulations, we aim to better understand how each variant strategy affects the effectiveness of vehicle localization, ultimately advancing our approach to reliable and efficient OTFS modulation for vehicular applications.

4.3.2 Initial Channel Angle Estimation

In this section, we use the MUSIC algorithm [103] to estimate the initial AoA information of the vehicle. Based on (4.10), in order to facilitate the AoA estimation, we convert it into the next equivalent vectorized equation:

$$\bar{\mathbf{X}} = \mathbf{C}\mathbf{A}_{music} \underbrace{\begin{bmatrix} s\left(t-\tau_1^h-\tau_q^g\right) & s\left(t-\tau_2^h-\tau_q^g\right) & \cdots & s\left(t-\tau_p^h-\tau_q^g\right) \end{bmatrix}^T}_{P\times 1 \ matrix} + \mathbf{N_0}, \tag{4.16}$$

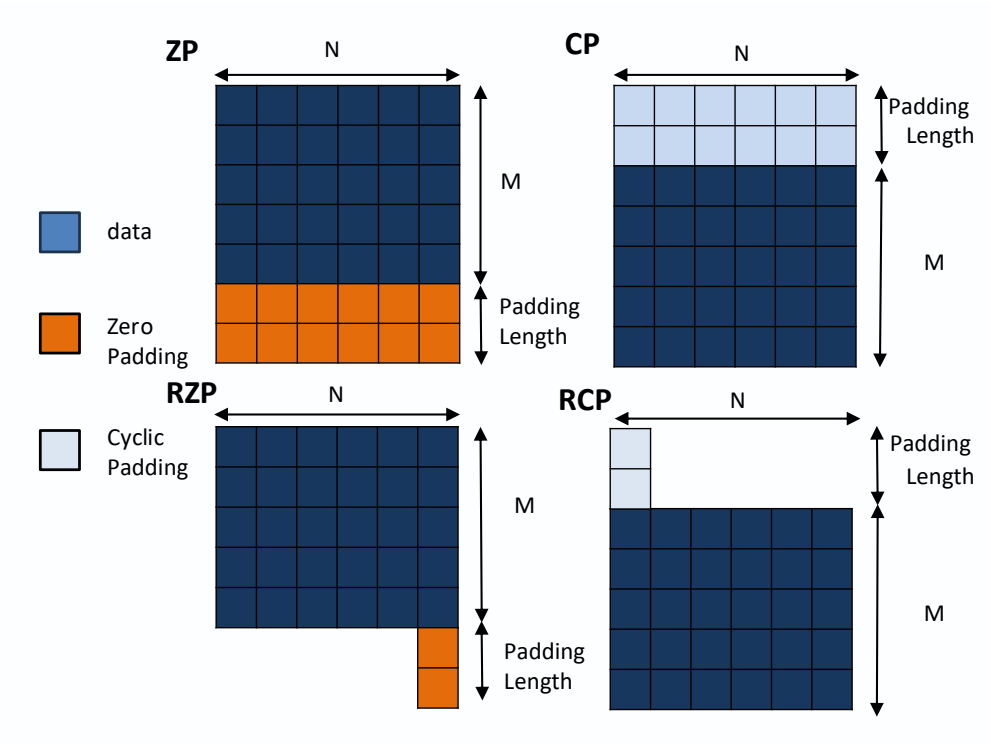


Fig.4.3: Different OTFS variant design (ZP, CP, RZP, RCP).

where $\mathbf{A}_{music} = \left[\mathbf{a}\left(\theta_1^{AOA}, \psi_1^{AOA}\right) \quad \ldots \quad \mathbf{a}\left(\theta_p^{AOA}, \psi_p^{AOA}\right) \right]$, $\mathbf{C}$ is defined in (4.12) and $\mathbf{N_0}$ is the noise. Then we can calculate the angles using with the MUSIC algorithm through the following steps:

$$\begin{aligned} \mathbf{R}_{\bar{\mathbf{X}}} &\triangleq E\left[\bar{\mathbf{X}}\bar{\mathbf{X}}^H\right] \\ &= \mathbf{C}^2\mathbf{A}E\left[\mathbf{S}\boldsymbol{S}^H\right]\mathbf{A}^H + \mathbf{C}^2E\left[\mathbf{N_0}{\mathbf{N_0}}^H\right] \\ &= \mathbf{C}^2\mathbf{A}\mathbf{R}_\mathbf{S}\mathbf{A}^H + \mathbf{C}^2\sigma^2\mathbf{I}_{MN}, \end{aligned} \tag{4.17}$$

where $\mathbf{I}_{MN}$ is a $M \times N$ identity matrix and σ^2 is the noise variance. Then we assume that the R_S is full-rank so that we can use the singular value decomposition (SVD) into $\mathbf{R}_{\bar{\mathbf{X}}}$ as

$$\mathbf{R}_{\bar{\mathrm{X}}} = \mathbf{U}\boldsymbol{\Sigma}\mathbf{V}^H, \tag{4.18}$$

where Σ denotes the singular value matrix, which is a diagonal matrix, $\boldsymbol{U} \in \mathbb{C}^{M_1M_2 \times M_1M_2}$ and V stand for the left and right singular vector matrix respectively. And, according to MUSIC algorithm, we use the right-most $M_1M_2 - P$ columns of matrix V, which are orthogonal eigenvectors corresponding to the smallest $M_1M_2 - P$ eigenvalues of $R_{\bar{\mathrm{X}}}$. This matrix subset is defined as $\mathbf{V}_{\bar{\mathbf{X}}} \in \mathbb{C}^{M_1M_2 \times (M_1M_2 - P)}$. Finally, the elevation and the azimuth angles $\left(\theta_p^{AOA}, \psi_p^{AOA}\right)$ can be determined by performing a joint search for peaks on the 2D MUSIC spectrum as

$$\mathbf{Q}_{\mathrm{MUSIC}}\left(\theta_i, \phi_i\right) = \frac{1}{\mathbf{a_i}^H\mathbf{V}_{\bar{\mathrm{X}}}\mathbf{V}_{\bar{\mathrm{X}}}^H\mathbf{a}_i}. \tag{4.19}$$

Finally, we can obtain the AoA on the RIS-vehicle link by calculating the value $\mathbf{Q}_{\text{MUSIC}}(\theta_i, \phi_i)$ in (4.19).

4.3.3 Reduced-PAPR Channel Estimation

Without loss of generality, we consider the ZP technique (the extension to other techniques is straightforward). We propose a low PAPR training design for channel estimation in ZP-coded OTFS schemes. This signal is used for detecting velocities and positions, and also carries the velocity data. Specifically, we propose a velocity-carried pilot structure to double-check if the BS has received the correct position and velocity information, which can be seen as a transformation of the ZP code. We assume that if the velocity is checked correctly, then the position will also be seen as correct.

In our system, as described in (4.1) in Section. III, we set a $M \times N$ symbol plot, where the delay bin index is denoted by $l = 1, 2 \ldots, M-1$, shows the delay of $\tau = \frac{l}{M\Delta f}$, and the Doppler bin index is expressed by $k = 0, 1, \ldots, N-1$, shows a Doppler shift of $\nu = \frac{k}{NT_s}$.

The Δf is the subcarrier spacing. The available bandwidth is $B = M\Delta f$, the frame duration is $T = NT_s$, and without loss of generality, we assume the $T_s\Delta f = 1$.

Again, as shown in Fig. 4.2, each cell in the figure represents a resource block in the delay-Doppler (DD) domain, which serves as the fundamental unit in OTFS (Orthogonal Time Frequency Space) modulation in the DD domain, the transmission signal can be divided into the pilot part and the transmission part of the velocity. This part is shown explicitly to explain our proposed velocity-carried low-PAPR design. However, the entire OTFS block is not solely dedicated to velocity data. In practice, the remaining regions of the OTFS frame—which are not shown in the figure—can be flexibly allocated for other types of data transmission, such as control signaling, additional sensing information, or communication payload. We assume that the GPS system is not available. However, the vehicle itself knows the velocity with some errors in the dashboard itself, so the vehicle will transmit the pilot symbols and the vehicle's velocity information as a double check in velocity. From this figure, we can see that in a sub-symbol, the velocity information and ZP and pilot signal combined the sub-symbol.

We can rewrite and depict the symbol matrix X in (4.1) as $\mathbf{X} = \mathbf{X}_p + \mathbf{X}_{vel} \in \mathbb{C}^{M\times N}$, where $\mathbf{X}_p$ is the pilot symbols and $\mathbf{X}_{vel}$ is the velocity information transmitted by the vehicle. In the ZP variant system, the l_{zp} is defined as the rows that are set to be zero along the delay axis, i.e. M axis. And we set the $l_{zp} = l_{\max} + l_{add}$, where $l_{\max}$ is the maximum delay taps index of the current scenario, and we have $\tau_{\max} = \frac{l_{\max}}{M\Delta f}$. The set for the length of $l_z p$ guarantees that the last rows of pilot symbols, denoted as l_{add}, are free of interference, allowing us to estimate the channel armed

with these pilot symbols. As for the pilot symbols, we set them as a Zadoff-Chu sequence under the formula of $X[l,k] = e^{-j\pi q\frac{k^2}{N}}$ and $l = M - l_{ZP}, \ldots, M-1$. The delay time domain representation can be expressed as

$$\tilde{\mathbf{X}} = \mathbf{X}\mathbf{F}_N^{\mathrm{H}}, \tag{4.20}$$

where the F_N is the N-point DFT matrix. We can then calculate and rewrite the time domain signal in (4.3) by vectorizing the signal of the time delay domain as:

$$\mathrm{s}(t) = \mathrm{s}_p + \mathrm{s}_{vel} = \mathrm{vec}\left(\mathbf{X}\mathbf{F}_{\mathrm{N}}^{\mathrm{H}}\right), \tag{4.21}$$

where $\mathrm{s}(t) \in \mathbb{C}^{MN\times 1}$, and we can also get $\mathrm{s}_d = \mathrm{vec}\left(\mathrm{X}_d\,\mathrm{F}_N^H\right)$ similarly. As for the DD channel, for the OMP algorithm we will use in the next part, we can have and rewrite the expression of the channel in (4.4) in a mathematical way by using h_i replacing h_p for all channel paths and rewriting the whole channel p as

$$h(\tau,\nu) = \sum_{i=1}^{Q} h_i \delta(\tau-\tau_i)\,\delta(\nu-\nu_i), \tag{4.22}$$

which is a sparse expression of the channel, and the Q means all the possibilities in the channel condition. So we can have the value of Q easily by calculating all possibilities as $Q = (l_{\max}+1)(2k_{\max}+1)$, where $l_{\max}$ and $k_{\max}$ are the maximum delay spread and the maximum Doppler spread index, respectively. The input-output relationship in time domain can be expressed as

$$r = \mathbf{H}\mathbf{s}_p + \mathbf{H}\mathbf{s}_{vel} + \mathbf{w} = \mathbf{r}_p + \mathbf{r}_{vel} + \mathbf{w}, \tag{4.23}$$

where the non-zero element h_i sparsely distributed in Q, combines all paths, or all taps in the DD plot. The value of h_i determines the channel coefficient, and the location of the element determines the delay and Doppler, respectively. Thus, we define the channel matrix as

$$\mathbf{H} = \sum_{i=1}^{Q} h_i \boldsymbol{\rho}^{l_i}\Delta^{k_i}, \tag{4.24}$$

where $\boldsymbol{\rho} \in \mathbb{C}^{MN\times MN}$ s a standard premutation matrix, $\Delta = \mathrm{diag}\left(z^0, z^1, \ldots z^{MN-1}\right) \in \mathbb{C}^{MN\times MN}$ is the diagonal Doppler matrix, and $z = e^{\frac{j2\pi}{MN}}$. The last l_{add} sample of each OTFS sub-symbol in r is unaffected by channel-induced data interference. This paper adopts a velocity check approach for channel estimation and position and velocity transmitting. We utilize these channel-affected pilot samples in r to estimate the channel vector h. This method is built upon the method [95], but with some key features designed for our velocity check. We set the M bins relatively short while the N bins relatively long since the velocity and pilot symbols will not occupy too much information.

Therefore, we sacrifice some delay resolution to improve the Doppler resolution. Additionally, we use only step one in [95] with a low complexity Maximum Ratio Combining (MRC) method to give a lower complexity and better calculation time. After substituting (4.23) into (4.24), we can replace the equations by

$$r = [\Psi_1, \Psi_2, \ldots, \Psi_{\mathrm{Q}}]\,\mathbf{h} + \mathbf{w} = \mathbf{\Psi}_{vel}\mathbf{h} + \mathbf{\Psi}_p\mathbf{h} + \mathrm{w}, \tag{4.25}$$

where $\mathbf{\Psi}_i = \boldsymbol{\rho}^{l_i}\Delta^{k_i} \in \mathbb{C}^{MN\times 1}$, and $\mathbf{h} \in \mathbb{C}^{Q\times 1}$ is the channel vector, and $\mathbf{\Psi} = \mathbf{\Psi}_p + \mathbf{\Psi}_{vel} \in \mathbb{C}^{MN\times Q}$ shows the time domain symbol matrix. And in the i-th element for the channel vector h, we define the delay and Doppler in the location by following rules:

$$\begin{cases} l_i = \mod(i-1, l_{\max}+1) \\ k_i = \text{ floor } \left(\frac{i-1}{l_{\max}-1}\right), \text{ if floor } \left(\frac{i-1}{l_{\max}-1}\right) \le k_{\max} \\ k_i = \text{ floor } \left(\frac{i-1}{l_{\max}-1}\right) \\ -(2k_{\max}+1), \text{ if floor } \left(\frac{i-1}{l_{\max}-1}\right) > k_{\max} \end{cases}, \tag{4.26}$$

In OTFS, the length of the pilot signal must be longer than $l_{\max}$ to be free of interference, and, since $l_{zp} = l_{\max} + l_{add}$, we can use the last rows l_{add} of the signals to estimate the channel as they are free of interference from the velocity signal and can be used directly as the channel estimation. We define them as r'_p and use a λ matrix to extract them, the extraction matrix is denoted as follows:

$$\boldsymbol{\lambda} = \left[\ \boldsymbol{\lambda}_0^T, \quad \boldsymbol{\lambda}_1^T, \quad \ldots, \quad \boldsymbol{\lambda}_{Nl_{add}-1}^T\ \right]^1, \tag{4.27}$$

where $\boldsymbol{\lambda}_i^T \in \mathbb{C}^{MN\times 1}$ is a vector, for $i = 0, \ldots, Nl_{add}-1$ whose floor $\left(\frac{i}{l_{\mathrm{add}}}\right)M + \mod(i, N)$-th element is 1 and other elements are all 0. So we can have the following expression:

$$\boldsymbol{\lambda}\mathrm{r} = \boldsymbol{\lambda}\mathbf{\Psi}\boldsymbol{h} + \boldsymbol{\lambda}\mathbf{w} = \boldsymbol{\lambda}\left(\mathbf{\Psi}_{\mathrm{vel}} + \mathbf{\Psi}_{\mathbf{p}}\right)\boldsymbol{h} + \boldsymbol{\lambda}\mathbf{w} = \mathbf{\Psi}'_{\boldsymbol{p}}\boldsymbol{h} + \mathbf{w}', \tag{4.28}$$

where $\boldsymbol{\lambda}\mathbf{\Psi}_{\mathbf{vel}}\mathbf{h} = 0^{N\times 1}$ and $\boldsymbol{\lambda}\Psi_p\mathrm{h}$ will only remain the information of the last l_{add} lines of the pilot signal, $\mathbf{\Psi}'_p \in \mathbb{C}^{Nl_{add}\times Q}$ is the non-interference time domain pilot matrix. We define the remaining part of the signal, which is generated by the last l_{add} rows of the pilot signals as $\mathbf{r}'_p$, so we define the signal we need at the first estimation part as

$$\mathbf{r}'_p = \mathbf{\Psi}'_p\mathbf{h} + \mathbf{w}' \in \mathbb{C}^{l_{add}N\times 1}, \tag{4.29}$$

Next, we use the orthogonal matching pursuit (OMP) algorithm to estimate the channel vector $\hat{h}$. As for the OMP estimation, it is a sparse matrix estimation method and we use it to estimate our channel information. In our model, we estimate it based on (4.29).

The main idea of the OMP algorithm is to compute the correlations between r and each column of Ψ_p, then identify the column with the highest correlation. This column indicates the index of h

that is nonzero. To start the algorithm, we need to set the residue, an index set, and the iteration counter:

$$\begin{cases} \mathbf{res}^{(0)} \leftarrow \mathbf{r}'_p \\ \Lambda^{(0)} = \varnothing \\ k = 1 \end{cases}, \tag{4.30}$$

then we extract the column whose absolute value of correlation with the residual vector is largest in $\mathbf{\Psi}'_p$:

$$\zeta^{(k)} = \underset{j \notin \Lambda^{(k-1)}}{\operatorname{argmax}} \left| \left\langle \mathbf{\Psi}'_{pj}, \mathbf{res}^{(k-1)} \right\rangle \right|, \tag{4.31}$$

and we extend the index set:

$$\Lambda^{(k)} = \Lambda^{(k-1)} \cup \left\{ \zeta^{(k)} \right\}, \tag{4.32}$$

using with the new index set, we can get new estimates by calculating

$$\hat{\mathbf{h}}^{(k)} \left(i \in \Lambda^{(k)} \right) = \underset{\hat{\mathrm{h}}}{\operatorname{argmin}} \left\| \Psi_{p\Lambda_k} \hat{\mathbf{h}} - \mathbf{r'}_p \right\|, \hat{\mathbf{h}}^{(k)} \left(i \in \Lambda^{(k)} \right) = 0, \tag{4.33}$$

where $\mathbf{\Psi}_{p\Lambda_k}$ is a sub-matrix of $\mathbf{\Psi}_p$ with the columns indicated by $\Lambda^{(k)}$, and under the (4.33), we can have

$$\begin{cases} \hat{\mathbf{r}}'_p(k) = \mathbf{\Psi}'_p \hat{h}^{(k)} \\ \mathrm{res}^{(k)} = \mathbf{r}'_p - \hat{\mathbf{r}}'_p(k) \end{cases}, \tag{4.34}$$

and we continue the loop to complete the estimation. By repeating this loop [104], we will finally get the estimated channel $\hat{h}$. Then we use the MRC [101] to complete the reception of the signal and obtain the velocity data. We need to point out that the reduction in PAPR is mainly achieved through the distribution pattern of the pilot symbols. Unlike traditional embedded pilot schemes where the pilot is concentrated at a single central location in the delay-Doppler domain, our method spreads the pilot symbols uniformly across a wider area within the frame. This even distribution helps to avoid localized power spikes, which are a common cause of high PAPR.

4.3.4 UKF-Based Velocity Position Estimation and Beam Tracking

In this section, we use the UKF to track the vehicle and assist in RIS beam tracking. The Kalman filter equations [51] are shown as follows:

$$\begin{cases} \mathbf{x}[n+1] = \mathbf{A}\mathbf{x}[n] + \mathbf{u}[n], \\ \widehat{\mathbf{\Theta}}[n] = \mathbf{h}(\mathbf{x}[n]) + \mathbf{v}[n] \end{cases}, \tag{4.35}$$

In (4.35), $\mathbf{u}[n]$ is the system noise, and $\mathbf{v}[n]$ denotes the measurement noise. To account for velocity changes in a real scenario, we include an acceleration component. This results in an extended state vector that includes acceleration, represented as:

$$\mathbf{x}[n] = [x_V, y_V, z_V, v_x, v_y, v_z, a_x, a_y, a_z], \tag{4.36}$$

Here, the parameter $*_V$ represents the position along the * axis, v_* denotes the velocity along the * axis, and a_* represents the acceleration in the * axis direction. Furthermore, the transition matrix can be expressed as

$$\mathbf{A} = \begin{bmatrix} 1 & 0 & 0 & \Delta t & 0 & 0 & 0.5\Delta t^2 & 0 & 0 \\ 0 & 1 & 0 & 0 & \Delta t & 0 & 0 & 0.5\Delta t^2 & 0 \\ 0 & 0 & 1 & 0 & 0 & 0 & 0 & 0 & 0.5\Delta t^2 \\ 0 & 0 & 0 & 1 & 0 & 0 & \Delta t & 0 & 0 \\ 0 & 0 & 0 & 0 & 1 & 0 & 0 & \Delta t & 0 \\ 0 & 0 & 0 & 0 & 0 & 1 & 0 & 0 & \Delta t \\ 0 & 0 & 0 & 0 & 0 & 0 & 1 & 0 & 0 \\ 0 & 0 & 0 & 0 & 0 & 0 & 0 & 1 & 0 \\ 0 & 0 & 0 & 0 & 0 & 0 & 0 & 0 & 1 \end{bmatrix}.$$

The measurement equation can be specifically expressed as

$$\begin{aligned} \widehat{\mathbf{\Theta}}[n] = \mathbf{h}(\mathbf{x}[n]) + \mathbf{v}[n] &= \begin{bmatrix} \frac{r[n]}{c} + v_\tau[n] \\ \varphi_{AOA}[n] + v_\varphi[n] \\ \vartheta_{AOA}[n] + v_\vartheta[n] \end{bmatrix} \\ &= \begin{bmatrix} \frac{\|\mathbf{p}[n]-\mathbf{p}_0\|}{c} + v_r[n] \\ \arctan\left(\frac{y_V[n]-p_0}{p_x-p_0}\right) + v_\varphi[n] \\ \arccos\left(\frac{z_V[n]-p_0}{\|\mathbf{p}[n]-\mathbf{p}_0\|}\right) + v_\vartheta[n] \end{bmatrix}. \end{aligned}$$

The symbol c is the light speed. Thus, we apply the UKF approach. Following the UKF transformation rules, we first perform an unscented transformation on $\mathbf{x}[n]$ for the collected data, which is structured as follows.

$$\begin{cases} \mathbf{x}[n]^{(0)}, i = 0 \\ \mathbf{x}[n]^{(i)} + \left(\sqrt{(a_{UT}+\lambda)\mathbf{P}}\right)_i, i = 1 \cdots a_{UT} \\ \mathbf{x}[n]^{(i)} - \left(\sqrt{(a_{UT}+\lambda)\mathbf{P}}\right)_i, i = a_{UT}+1 \cdots 2a_{UT}, \end{cases} \tag{4.37}$$

In this form, we define that $\mathbf{P}$ is the covariance matrix of the parameter $\mathbf{x}[n]$, λ is a scaling factor used to reduce the error and a_{UT} is the dimensionality of the state. According to the next step of the UKF, we also calculate the corresponding weight $\mathbf{w}$, which is given by

$$w[n] => \begin{cases} w[n]^{(0)}_{means} = \frac{\lambda}{a_{UT}+\lambda} \\ w[n]^{(0)}_{\text{cov}} = \frac{\lambda}{a_{UT}+\lambda} + (1-\alpha^2+\beta) \\ w[n]^{(i)}_{\text{cov}} = w[n]^{(i)}_{means} = \frac{\lambda}{2a_{UT}+2\lambda}, i = 1 \cdots 2a_{UT}, \end{cases} \tag{4.38}$$

$$\mathbf{x}^{(i)}(n) = \left[\begin{array}{ccc} \widehat{\mathbf{x}}(n) & \widehat{\mathbf{x}}(n) + \sqrt{(a_{UT}+\lambda)\mathbf{P}(n)} & \widehat{\mathbf{x}}(n) - \sqrt{(a_{UT}+\lambda)\mathbf{P}}(n) \end{array} \right], \tag{4.39}$$

$$\mathbf{P}(n+1 \mid n) = \sum_{i=0}^{2n} w^{(i)} \left[\widehat{\mathbf{x}}(n+1 \mid n) - \mathbf{x}^{(i)}(n+1 \mid n)\right] \left[\widehat{\mathbf{x}}(n+1 \mid n) - \mathbf{x}^{(i)}(n+1 \mid n)\right]^{\mathrm{T}} + \mathbf{Q}. \tag{4.40}$$

$$\begin{cases} \mathbf{P}_{\mathbf{\Theta\Theta}}(n+1) = \sum\limits_{i=0}^{2n} w^{(i)} \left[\mathbf{\Theta}^{(i)}(n+1 \mid n) - \overline{\mathbf{\Theta}}(n+1 \mid n)\right] \left[\mathbf{\Theta}^{(i)}(n+1 \mid n) - \overline{\mathbf{\Theta}}(n+1 \mid n)\right]^{T} + R \\ \mathbf{P}_{\mathbf{x\Theta}}(n+1) = \sum\limits_{i=0}^{2n} w^{(i)} \left[\mathbf{x}^{(i)}(n+1 \mid n) - \overline{\mathbf{\Theta}}(n+1 \mid n)\right] \left[\mathbf{\Theta}^{(i)}(n+1 \mid n) - \overline{\mathbf{\Theta}}(n+1 \mid n)\right]^{\mathrm{T}}, \end{cases} \tag{4.42}$$

$$\begin{cases} \mathbf{K}(n+1) = \mathbf{P}_{\mathbf{x\Theta}}(n+1)\mathbf{P}_{\mathbf{\Theta\Theta}}^{-1}(n+1) \\ \widehat{\mathbf{x}}(n+1) = \widehat{\mathbf{x}}(n+1 \mid n) + \mathbf{K}(n+1)\left[\mathbf{\Theta}(n+1) - \mathbf{h}\left[\mathbf{x}(n+1 \mid n)\right]\right] \\ \mathbf{P}(n+1) = \mathbf{P}(n+1 \mid n) - \mathbf{K}(n+1)\mathbf{P}_{\mathbf{\Theta\Theta}}(n+1)\mathbf{K}^{\mathrm{T}}(n+1) \end{cases}, \tag{4.43}$$

$$\begin{cases} \mathbf{x}^{(i)}(n+1|n) = \Big[\widehat{\mathbf{x}}(n+1|n),\ \widehat{\mathbf{x}}(n+1|n) + \sqrt{(a_{UT}+\lambda)\,\mathbf{P}(n+1|n)}, \\ \qquad\qquad \widehat{\mathbf{x}}(n+1|n) - \sqrt{(a_{UT}+\lambda)\,\mathbf{P}(n+1|n)}\Big], \\ \mathbf{\Theta}^{(i)}(n+1|n) = \mathbf{h}\Big(\mathbf{x}^{(i)}(n+1|n)\Big), \\ \overline{\mathbf{\Theta}}(n+1|n) = \sum\limits_{i=0}^{2n} w^{(i)}\,\mathbf{\Theta}^{(i)}(n+1|n). \end{cases} \tag{4.41}$$

where $\lambda = \alpha^2(a_{UT}+\kappa) - a_{UT}$. In (4.40), α controls the distribution state in the unscented transformation, and κ ensures that the matrix $(a_{UT}+\lambda)\mathbf{P}$ remains positive semi-definite. β is non-negative and accounts for the impact of higher-order terms. These parameters are generally chosen based on experience and can be adjusted as needed depending on the specific scenario. By following the steps outlined above, we can generate a set of points that preserve the same mean and variance as the original data. Next, we reformulate the data and the associated weights derived from (4.37) and (4.38) in the following form

By following the above process, we obtain a set of sigma points and their corresponding weights, along with the estimated covariance matrix $\mathbf{P}(n+1 \mid n)$. Using this approach, we compute the sigma points set for the predicted values, yielding a new set of unscented transformation points $\mathbf{x}^{(i)}(n+1 \mid n)$. From these transformed parameters, we can then calculate the measurement values, resulting in the following outcomes:

Algorithm 2 Overall Localization Algorithm

Require: Uplink signal from the vehicle $\mathbf{s}(t)$ containing velocity information and low-PAPR pilot

Ensure: Estimated vehicle velocity and position at the BS $\mathbf{x}[n+1]$

for each time slot n **do**
    The vehicle transmits $\mathbf{s}(t)$ with embedded velocity data and low-PAPR pilot
    At the BS side, estimate the delay of the RIS–BS LoS link
    Estimate the angles of arrival of the RIS–vehicle LoS link using the MUSIC algorithm based on (4.16)–(4.19)
    Estimate the channel via the OMP algorithm according to (4.30)–(4.34)
    Obtain the velocity-related measurements using the MRC-based detector
    Estimate the vehicle velocity and position with the UKF using the pilot signal, based on (4.35)–(4.38)
    Cross-check the velocity estimates from the two paths (OTFS-based and UKF-based)
    if thre $< |v_t - v_{\text{ukf}}|$ **then**
        Refine the velocity estimate using (4.54)
        break ▷ Exit the current iteration once the refined velocity is obtained
    else
        Restart the velocity transmission and repeat the above steps for the next iteration
    end if
end for
return $\mathbf{x}[n+1]$ ▷ Final estimated velocity and position at the BS

Next, we introduce two auxiliary parameters for the process: the variance matrix of the measurement parameter and the covariance matrix between the position parameters and the measurement parameter, as follows:

4.3.5 Robust Velocity Estimation Method

In this section, we introduce our robust velocity estimation method. This method uses UKF to improve the accuracy of the velocity estimation, instead of using only the velocity information transmitted by the signal part. We define our obtained velocity as v_t and v_{ukf}, which means the velocity transmitted directly by the vehicle and the velocity estimated by UKF, respectively. The real velocity is defined as v. And we have the following definition:

$$\begin{cases} v_t = v + n_1, \quad n_1 \sim N\left(0, \sigma_1^2\right) \\ v_{ukf} = v + n_2, \quad n_2 \sim N\left(0, \sigma_2^2\right) \end{cases}, \tag{4.44}$$

where n_1 means the system error from the transmitting part including the quantitation error, transmitting error and some other errors, and n_2 means the system error from the kalman filter part.

Lemma 1: Then in order to obtain the velocity, we need to combine these two velocities and obtain a new estimated one $\hat{v}$ with some parameters as following (4.45)

$$\hat{v} = \alpha_1 v_t + \alpha_2 v_{ukf}, \tag{4.45}$$

Then we have the following relationships

$$\alpha_1 = \frac{\sigma_2^2}{\sigma_1^2 + \sigma_2^2}, \quad \alpha_2 = \frac{\sigma_1^2}{\sigma_1^2 + \sigma_2^2}. \tag{4.46}$$

Proof. In order to complete the estimate, we set the following minimum square error (MSE) estimation and minimize it as following

$$\text{MSE} = \mathbb{E}\left[(\hat{v} - v)^2\right], \tag{4.47}$$

substitute (4.45) into (4.47) and we can get the

$$\begin{aligned} \text{MSE} &= \mathbb{E}\left[(\alpha_1 (v + n_1) + \alpha_2 (v + n_2) - v)^2\right] \\ &= \mathbb{E}\left[(\alpha_1 v + \alpha_1 n_1 + \alpha_2 v + \alpha_2 n_2 - v)^2\right] \\ &= \mathbb{E}\left[((\alpha_1 + \alpha_2 - 1) v + \alpha_1 n_1 + \alpha_2 n_2)^2\right] \end{aligned}, \tag{4.48}$$

Since v,n_1 and n_2 are independent and have zero means, all cross terms vanish

$$\mathbb{E}[v n_1] = \mathbb{E}[v n_2] = \mathbb{E}[n_1 n_2] = 0. \tag{4.49}$$

And then we have

$$\text{S} = (\alpha_1 + \alpha_2 - 1)^2 \sigma_v^2 + \alpha_1^2 \sigma_1^2 + \alpha_2^2 \sigma_2^2. \tag{4.50}$$

To minimize the MSE, take partial derivatives of MSE with respect to α_1 and α_2 as

$$\begin{cases} \frac{\partial \text{S}}{\partial \alpha_1} = 2 (\alpha_1 + \alpha_2 - 1) \sigma_v^2 + 2\alpha_1 \sigma_1^2 = 0 \\ \frac{\partial \text{S}}{\partial \alpha_2} = 2 (\alpha_1 + \alpha_2 - 1) \sigma_v^2 + 2\alpha_2 \sigma_2^2 = 0, \end{cases} \tag{4.51}$$

To solve the equations, we set it as the matix form and solve it as

$$\begin{bmatrix} \sigma_1^2 & \sigma_v^2 \\ \sigma_v^2 & \sigma_2^2 \end{bmatrix} \begin{bmatrix} \alpha_1 \\ \alpha_2 \end{bmatrix} = \begin{bmatrix} \sigma_v^2 \\ \sigma_v^2 \end{bmatrix}, \tag{4.52}$$

and get the result as

$$\alpha_1 = \frac{\sigma_2^2}{\sigma_1^2 + \sigma_2^2}, \quad \alpha_2 = \frac{\sigma_1^2}{\sigma_1^2 + \sigma_2^2}. \tag{4.53}$$

So we have the optimal estimator is:

$$\hat{v} = \frac{\sigma_2^2}{\sigma_1^2 + \sigma_2^2} v_t + \frac{\sigma_1^2}{\sigma_1^2 + \sigma_2^2} v_{ukf}. \tag{4.54}$$

□

And because the bit error may cause a huge error, we set a threshold to check if the velocity need to be retransmitted as following

$$thre < \left| v_t - v_{ukf} \right|, \tag{4.55}$$

if it is not satisfied, we assume the transmit velocity is wrong.

Finally, we complete the prediction using the classic Kalman filter process by calculating the Kalman gain and finalizing the iterative process. For better understanding, we also include the overall algorithm, as shown in **Algorithm 2**.

In the algorithm, we predict the position, velocity, and acceleration result in $\widehat{\mathbf{x}}(n+1)$ in each time-slot to obtain the vehicle information in a near real-time condition. The intention is to prevent large discrepancies caused by severe channel distortion, unexpected vehicle maneuvers, or bit errors. Although fixed, it serves as a fail-safe mechanism rather than a frequently triggered feature.

4.4 Evaluation of the Proposed Method 2: RIS-Assisted OTFS under NLoS

In this section, we compare and analyze performance and numerical results under different conditions. The main simulation parameters are given in Table 4.3. In our simulation, we assume a typical RIS-assisted vehicular communication scenario where the direct link between the vehicle (user) and the base station (BS) is fully blocked due to obstacles such as buildings or terrain. Therefore, the vehicle-BS path is modeled as NLoS and is completely unavailable—all communication relies on the reflection via the RIS.

For the vehicle-to-RIS link, we model three propagation paths to represent a realistic urban environment with local scattering around the vehicle. These paths may include one dominant component (quasi-LoS) and two weaker multipath reflections.

For the RIS-to-BS link, we assume a single LoS path, as the RIS is typically deployed with an unobstructed view toward the base station (e.g., mounted high on a building).

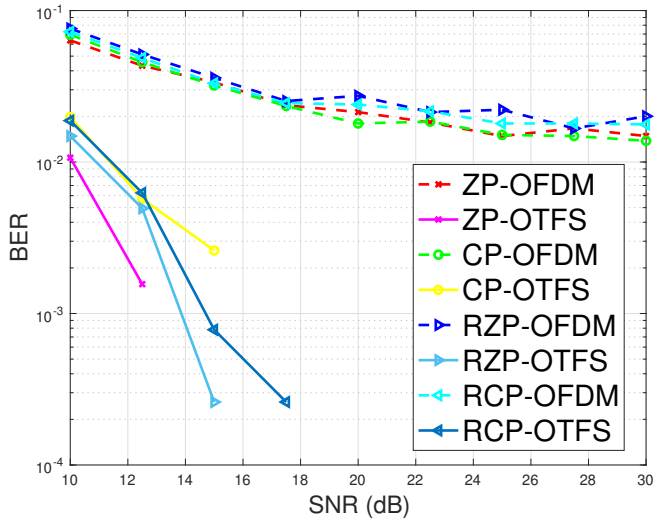


Fig.4.4: BER performance under different variant.

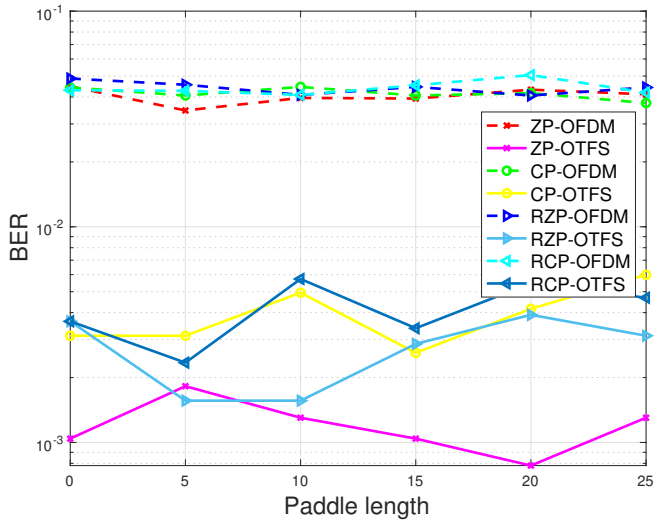


Fig.4.5: BER performance for different padding lengths using several variant methods (SNR = 15 dB).

Regarding the energy ratio between the LoS and NLoS components, since the vehicle-BS NLoS path is assumed to be entirely blocked, no energy arrives directly at the BS from the user. All the signal power received at the BS originates from the reflected signal via the RIS. The energy contribution from each path is therefore determined by geometry-based path loss and RIS beamforming, and we do not artificially assign a LoS/NLoS energy ratio in the simulation.

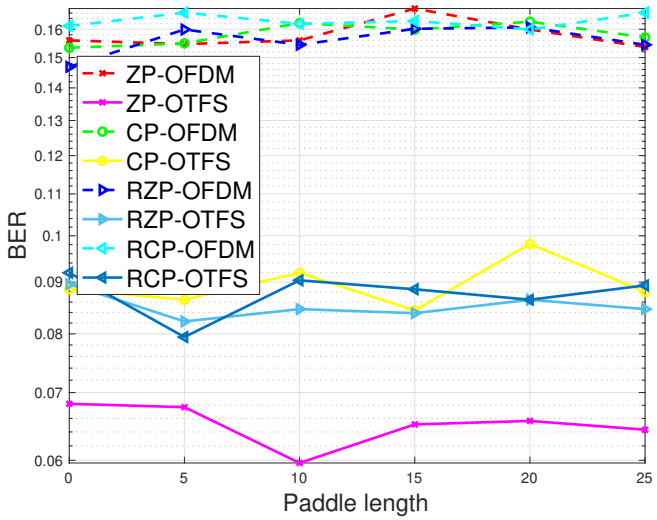


Fig.4.6: BER performance for different padding lengths using several variant methods (SNR = 10 dB).

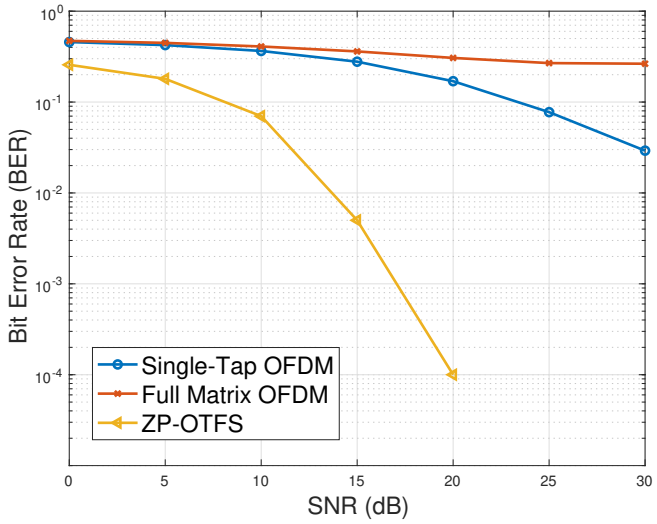


Fig.4.7: The BER comparison with FULL matrix OFDM and ZP-OTFS when the velocity is 200 km/h.

4.4.1 OTFS Performance

In this subsection, we study the performance of the proposed OTFS technique, including comparisons with traditional OFDM. Our goal is to examine these variant modulations closely and evaluate their effectiveness across various dimensions, allowing us to identify their respective ad-

Table4.3: Simulation parameters for NLoS Scenario.

Parameter	**Value**
BS–RIS path	1
RIS reflection efficiency	0.8
RIS–vehicle path	3
Carrier frequency	28 GHz
Delay bins M	64
Doppler bins N	32
RIS antennas (M_1, M_2)	From 2 to 16
Subcarrier bandwidth Δf	150 kHz
l_{add}	5
Reference signal periodicity	Every 100 ms
Vehicle antenna height	7 m
Location of BS antenna $\mathbf{P}_R = (x_R, y_R, z_R)$	$(200, -30, 15)$ m
Location of RIS antenna $\mathbf{P}_V = (x_V, y_V, z_V)$	$(180, -20, 15)$ m

vantages and limitations in different applications. In Fig. 4.4, we compare the BER under different SNRs using different variant methods. As expected, a higher SNR leads to a lower BER. We can also see a gap between the OFDM modulation and the OTFS modulation, which shows a better performance of the OTFS. Also, we can see that when the SNR is higher than approximately 15 dB, the BER of OTFS in different variant methods remain in extremely good condition. In addition, in Figs. 4.5 and 4.6, we analyze two different SNRs higher than or lower than 15 dB for the analysis of different padding lengths, and we can observe that no matter how long the padding length varies, the OTFS always performs better than OFDM with an obvious gap due to the high speed of the vehicle.We also propose and adopt a modified ZP-based pilot structure, which is a deviation from the classical ZP-OTFS. Specifically, rather than using true zero-padding, we embed a structured signal to guarantee low PAPR, Maintained Partial Sparsity in Channel Matrix: Despite the non-zero pilot, the structure of the delay-Doppler channel still exhibits the lowest sparsity, and also have the relatively low bit error rate. When the SNR is less than 15 dB, the BER in OTFS also becomes obviously higher compared to the result in SNR = 20 dB. So we can see that the padding length does not affect too much, but considering the Inter Symbol Interference (ISI), we still recommend some paddle amounts. And In Fig. 4.7, we also implemented full matrix-based MMSE equalization for OFDM in our simulations. Although this improves OFDM performance slightly compared to single-tap equalization, the performance gap between OTFS and OFDM remains significant under high Doppler conditions.

4.4.2 Result in MUSIC Algorithm

In this subsection, we will analyze the MUSIC algorithm and the UKF part. In this part, we just follow the traditional MUSIC algorithm to obtain the initial angles, and we use three paths to track the AoA to show the accuracy as shown in Fig. 4.8. Since it is not the main point of our analysis, we just follow the traditional method [9].

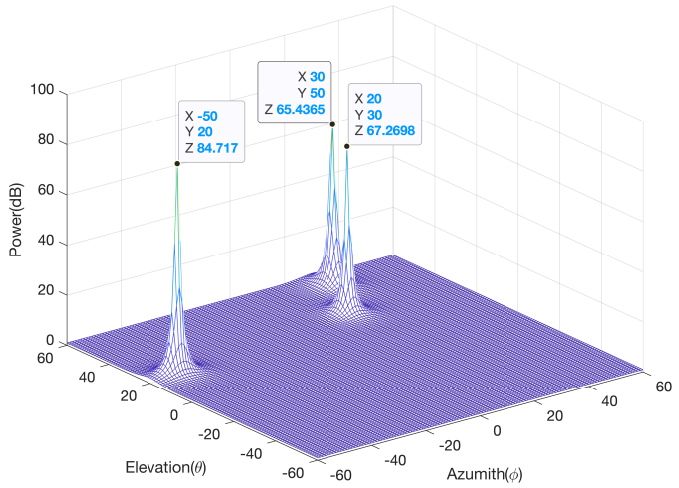


Fig.4.8: The MUSIC algorithm to get the elevation and azimuth in different paths from the vehicle.

4.4.3 Result in low PAPR Estimation Method

In this subsection, we will get the result of the low PAPR estimation method. we will compare BER, MNSE, spectrum efficiency, and PAPR from Fig. 4.9 to Fig. 4.12. In the BER and MMSE comparisons, we compare different velocity and QAM schemes and their influence and performance. First, we compare the BER with MNSE and in different scenarios in Fig. 4.9 and 4.10. We compare velocities of 100, 200, and 300 km/h, alongside the 4 QAM and 16 QAM schemes, comparing our method with the embedded method as a benchmark. And we also compare our method and embedded method as a benchmark. On the one hand, as for the velocity, because the OTFS has robustness in any velocities, we can see that no matter how the velocity changes, the BER and MNSE are both extremely stable and have lower BER when the SNR becomes larger. On the other hand, the 16 QAM condition will perform worse than 4 QAM in our proposed method as a general condition. We also compare our method with the embedded pilot benchmark. On the one hand, the performance of 4 QAM in our proposed method is better compared to the embedded

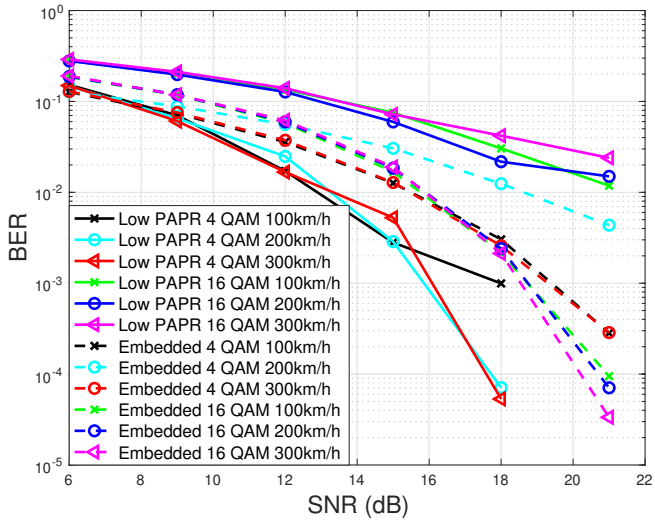


Fig.4.9: BER performance for different SNR among different OTFS modulation.

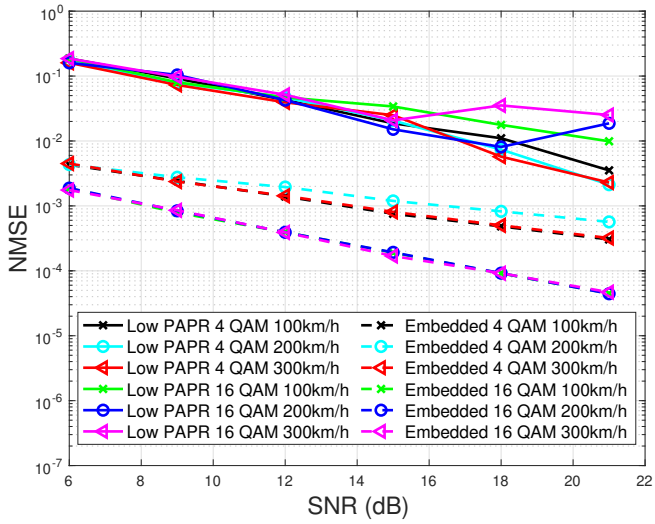


Fig.4.10: NMSE under different SNR among different OTFS modulation.

pilot, while the 16 QAM has worse performance. It can also be understood that our low PAPR may make it easier to get errors in 16 QAM. On the other hand, considering the distortion that can be produced during very high (more than 10) PAPR and also at very high velocity such as 500 km/h. It is also worth noting that when the SNR is relatively low, our proposed method can perform similarly to the embedded pilot method.

In addition, the embedded pilot scheme exhibits better MNSE compared to our method, as shown in Fig. 4.10, while maintaining stability in velocity. In Fig. 4.11, we calculate the spectrum

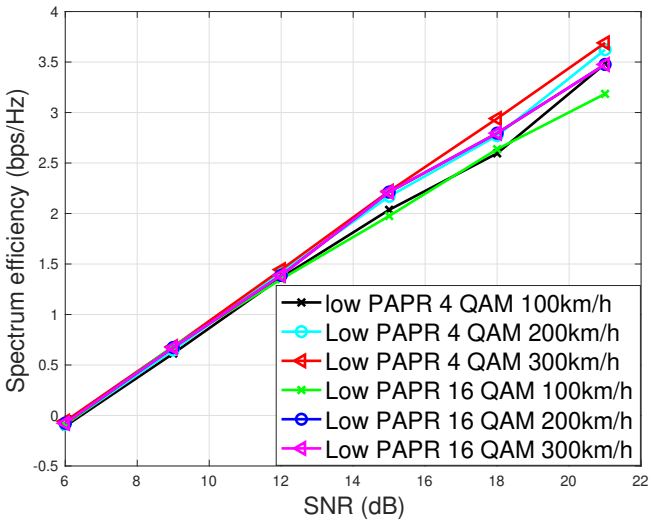


Fig.4.11: Spectral efficiency for different SNR among different OTFS modulation.

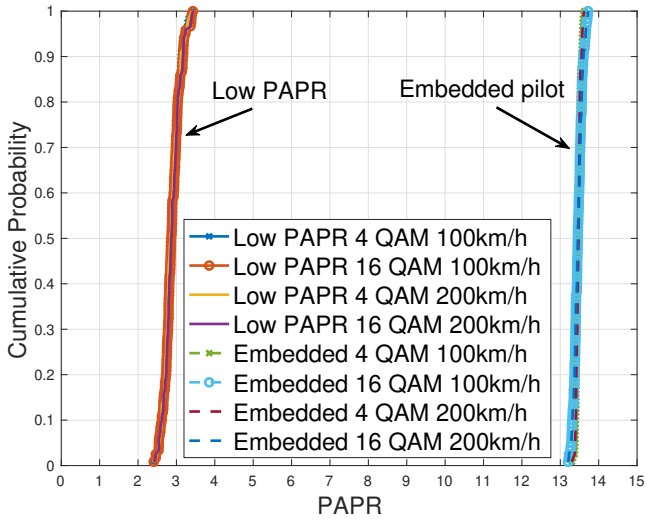


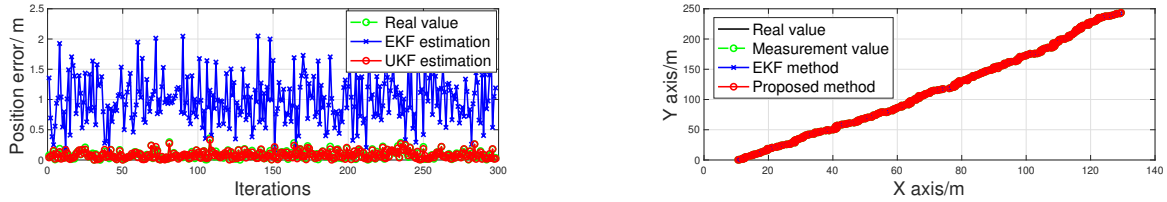
Fig.4.12: Cumulative probability of the PAPR for different OTFS schemes.

efficiency for our proposed method, and it is also comparatively stable no matter how the velocity changes, and the 4 QAM and 16 QAM will have similar performance, while the 4 QAM will have better robustness in signal interference. We then compare the PAPR for different velocities and 4 QAM and 16 QAM with our method and the embedded pilot method. it can be seen that our low PAPR method can have a lower PAPR compared to embedded pilots, regardless of the velocity and QAM condition. In Fig. 4.12, Our method consistently maintains a PAPR of approximately 3, while the embedded pilot method has a PAPR of more than 13. The large PAPR can have a

significant poor influence such as signal amplifier distortion and transmission error, etc., so in our method, we calculate the average PAPR and compare them, the PAPR will only be about 21.54 % of the embedded pilot, which will be much easier to transmit without distortion.

Complexity Note: The OTFS receiver includes SFFT/ISFFT operations ($\mathcal{O}(MN \log MN)$), sparse estimation via OMP ($\mathcal{O}(P^2MN)$), and MMSE detection. In contrast, OFDM uses $\mathcal{O}(N \log N)$ FFT and single-tap equalization. While OTFS is more complex, its robustness under Doppler spread justifies the added cost in high-mobility scenarios.

4.4.4 Result in UKF Tracking



(a) Position estimation error.

(b) Vehicle trajectory.

Fig.4.13: Localization performance in the straight driving scenario. (a) estimation error, (b) reconstructed trajectory.

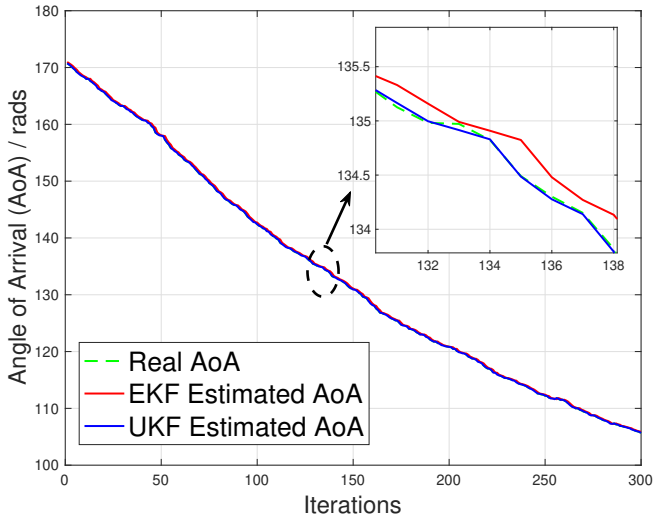
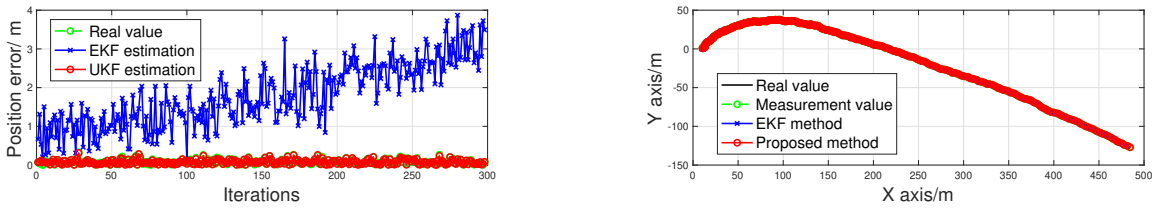


Fig.4.14: The AoA estimation in a straight scenario.

In the UKF part, we give the conditions of the straight line condition and the curve scenario in Fig. 4.13 and Fig. 4.15, respectively. For the estimation of AoA, we give the results in Fig.



(a) Position estimation error.

(b) Vehicle trajectory.

Fig.4.15: Localization performance in the curved driving scenario. (a) estimation error, (b) reconstructed trajectory.

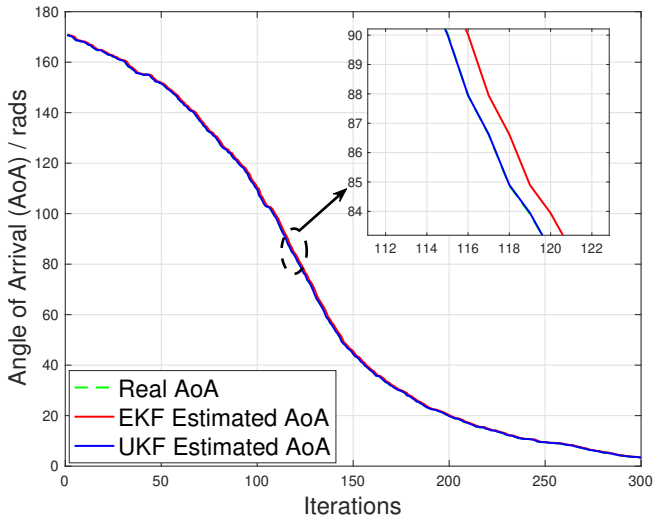


Fig.4.16: The AoA estimation in curve scenario.

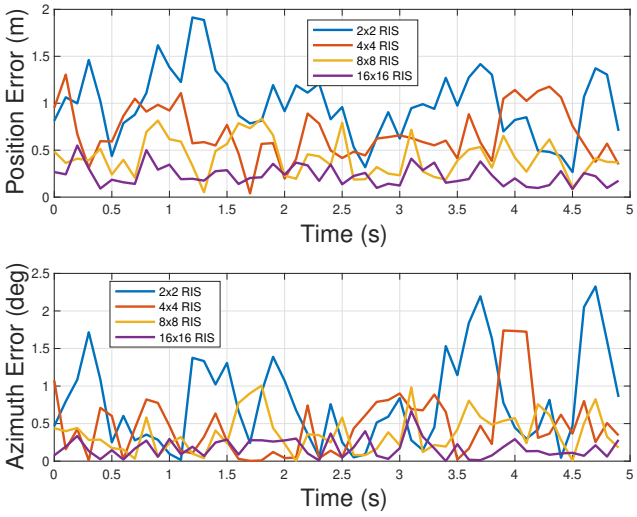


Fig.4.17: The error in different antenna scale of RIS.

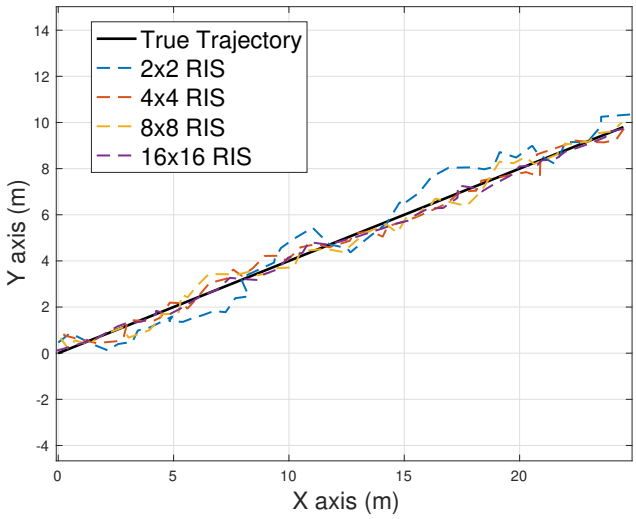


Fig.4.18: The trajectory in different antenna scale of RIS.

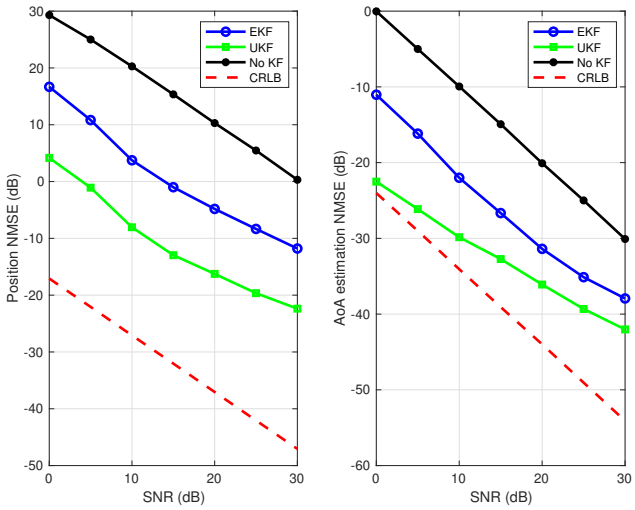


Fig.4.19: The CRLB analysis of the position and AoAs.

4.14 and Fig. 4.16, respectively, for the straight and curve scenarios. We take the real value and the EKF value as a reference point. We can see that no matter what condition it is, the UKF will always perform better in position and angle tracking, which will provide a reference for the RIS beam tracking in the RIS configuration as explained before.

As for the analysis of the RIS antenna, we can see that Fig. 4.17 shows the estimation errors of the position and azimuth angle on different scales of the RIS antenna array. It can be seen that as the number of RIS elements increases from 2×2 to 16×16, both the position error

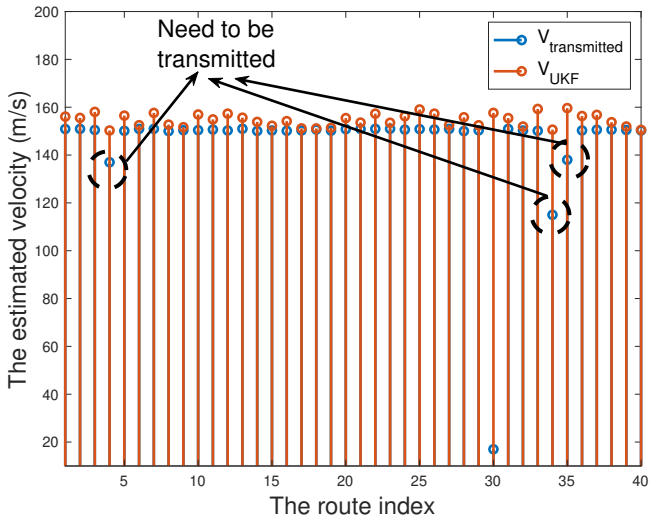


Fig.4.20: System accuracy.

and the AoA (Azimuth) error decrease significantly. This is because larger RIS arrays provide higher signal gain, which improves measurement accuracy and reduces uncertainty in the UKF estimation process. In particular, the 16 $\times$ 16 RIS configuration exhibits the lowest and most stable error performance throughout the simulation period. And Fig. 4.18illustrates the estimated 2D trajectories using UKF under different RIS configurations, compared to the true trajectory. The estimation accuracy improves as the RIS scale increases. The 2 $\times$ 2 RIS trajectory deviates noticeably from the true path, while the 16 $\times$ 16 RIS estimation almost perfectly follows the actual trajectory. This further confirms that a larger RIS array improves the angular and range sensing, significantly improving the overall tracking performance.

In order to compare the result more clearly, we have included the Cramer-Rao Bound (CRB) as a reference for the position and AOA estimation results in the simulation section. Fig. 4.19 presents the normalized mean square error (NMSE) of position estimation (left) and AoA estimation (right) with respect to SNR, comparing the performance of EKF, UKF without Kalman filter and the theoretical CRLB. In the left subplot, we observe that the NMSE of position estimation for both EKF and UKF decreases monotonically as the SNR increases. The UKF consistently outperforms the EKF across the entire SNR range due to its better handling of nonlinear models. The CRLB provides a theoretical lower bound, and the UKF approaches this bound more closely than the EKF, especially at high SNR. In the right subplot, a similar trend is observed in the AoA estimation. The UKF demonstrates superior angular estimation performance compared to the EKF and achieves results closer to the CRLB. And they both outperform the condition without Kalman filter. This again highlights the advantage of UKF in capturing nonlinear relationships in the mea-

surement model. In addition, both estimation methods improve significantly with increasing SNR, showing that high-quality signal conditions greatly improve tracking accuracy.

In addition, the use of Kalman filters (both EKF and UKF) consistently improves both the position and the accuracy of the AoA estimation compared to using raw measurements directly without filtering.

Specifically, even at relatively high SNR (e.g., 20–30 dB, corresponding to sub-meter level measurement noise), Kalman filters still provide slightly better or at least comparable estimation accuracy in our dynamic scenario.

Because the Extended Kalman Filter (EKF) relies on a first-order Taylor expansion (linearization) of the nonlinear state and observation models. This approximation becomes inaccurate when the system exhibits strong nonlinearity, such as during rapid vehicle acceleration, sharp turns, or under fluctuating Doppler and AoA conditions induced by RIS reflections. In contrast, the Unscented Kalman Filter (UKF) does not rely on local linearization. Instead, it uses the unscented transform to propagate a carefully chosen set of sigma points through the nonlinear system, capturing the true mean and covariance more accurately up to the second-order statistics. So in our results, the UKF tends to have better results

4.4.5 Robust Velocity Estimation Method Reliability

We simply use a stem plot to show the reliability of our method in Fig. 4.20. We can see that when the velocity is very close between v_1 and v_2, we assume the velocity is correct, when they get extremely far, we assume the velocity is wrong and need to be retransmitted.

4.4.6 Complexity Analysis of Channel Estimation

First, we show the complexity of the channel estimation and receive part, which can be divided mainly into the OMP algorithm and the MRC receive. First, we analyze the OMP part. The complexity can be summarized as matching, orthogonal projection, and residue up, and the total complexity can be considered as $O(k * Nl_{add} * Q)$. As for MRC complexity, we use the MRC algorithm based on [105], so the readers can refer to this paper for its complexity. Next, as for the UKF part, for the first part, we choose $2a_{UT} + 1$ sigma points and propagate them through the model of the non-linear system. The calculation for each sigma point is $O(a_{UT})$, so the total complexity is approximately $O(a_{UT}^2)$. Then, the analysis of the prediction step includes calculating the predicted covariance matrix, which includes the weighted sum of each sigma point, with a complexity of $O(a_{UT}^2)$. For the update step, the predicted measurement covariance matrix and the

cross-covariance matrix are calculated. This involves *mea* observation variables and $2a_{UT} + 1$ sigma points, with a complexity of $O(mea \times a_{UT}^2)$. In addition, there is an inversion of an $mea \times mea$ matrix, which has a complexity of $O(mea^3)$. In general, the total complexity of the UKF is similarly affected by $O(a_{UT}^2) + O(mea \times a_{UT}^2) + O(mea^3)$.

Chapter 5

Multi-User Scenario Extension and System Unification

5.1 Multi-User OTFS Channel Modeling

5.1.1 Main Introduction

In modern wireless communication systems, the demand for reliable high-capacity transmissions continues to grow, particularly in scenarios characterized by high mobility and dense multi-user connectivity. Orthogonal Time Frequency Space (OTFS) modulation has recently emerged as a promising candidate due to its robustness against Doppler effects and its ability to provide a sparse and stable representation of time-varying channels. However, practical deployment of OTFS still faces critical challenges such as efficient pilot design, low peak-to-average power ratio (PAPR) transmission, and scalability to a large number of users.

To address these issues, we previously introduced a *low-PAPR page-style OTFS modulation framework* [106, 6], which improves pilot placement strategies for enhanced channel estimation and applies successive interference cancellation (SIC) for effective multi-user detection. While prior studies have demonstrated the framework's effectiveness in mitigating interference and improving bit error rate (BER) performance, additional analysis is required to fully assess its robustness under diverse system conditions.

In this extended work, we broaden the scope of our study to the following key aspects:

- **Impact of mobility:** We evaluate system performance at different vehicle speeds, highlighting the robustness of the page-style OTFS framework in high-mobility scenarios.
- **Impact of subcarrier configurations:** We investigate how varying the number of subcarriers affects BER, spectral efficiency, and PAPR, thereby demonstrating the adaptability of

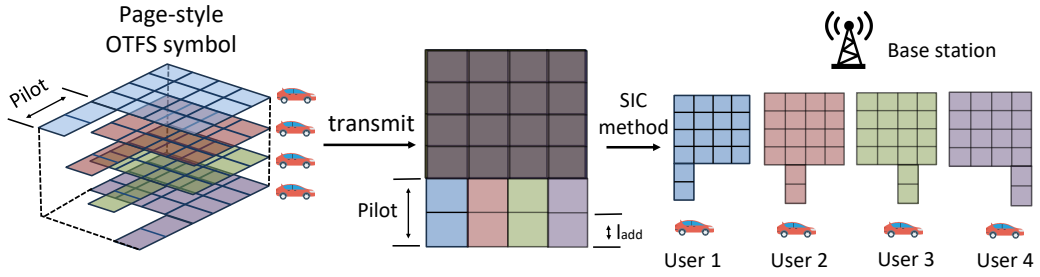


Fig.5.1: The framework of the page-style system

the framework to different bandwidth settings.

- **Impact of user scalability:** We analyze system performance when increasing the number of active users, focusing on the trade-offs between interference mitigation, detection complexity, and overall throughput.

Through extensive simulations, we demonstrate that the proposed page-style OTFS framework consistently outperforms conventional methods, including OFDM and non-orthogonal multiple access (NOMA), under all considered conditions. Our findings validate the suitability of this framework for next-generation communication systems that require mobility resilience, scalability, and power-efficient transmission.

5.1.2 Methods

This section describes the system model.

5.1.3 Basic Assumptions

We assume K users in our scenario, and the Delay-Doppler (DD) domain is divided into M and N bins along the delay and Doppler axes, respectively. The l-th delay bin ($l = 0, 1, \cdots, M-1$) corresponds to the delay of $\tau = \frac{l}{M\Delta f}$, the k-th Doppler bin ($k = 0, 1, \cdots, N-1$), which denotes the Dopper shift index of $\nu = \frac{k}{NT_s}$, where Δf express the subcarrier spacing. We assume that the bandwidth can be used as $B = M\Delta f$, the time duration of the scenario T is $T = NT_s$, and T_s denotes the OTFS sub-symbol duration, and we have $T_s\Delta f = 1$. The signal transmitted in the delay-Doppler (DD) domain is illustrated in Fig. 5.1. We can also let the transmitted DD-domain signal of the n-th user be expressed as a matrix.

$$\mathbf{X}^{(n)} = \mathbf{X}_d^{(n)} + \mathbf{X}_p^{(n)} \in \mathbb{C}^{M\times N}, \tag{5.1}$$

where $\mathbf{X}^{(n)}$ denotes the delay-Doppler domain signal channel of the n-th user, $\mathbf{X}_d^{(n)}$ and $\mathbf{X}_p^{(n)}$ represent the data symbols and pilot symbols of the n-th user, respectively. For each user, we have similar settings. The parameter l_p, which denotes the number of rows that must be set to zero along the delay axis, is configured as $l_p = l_{\max} + l_a dd$, where $l_{\max}$ is the maximum delay spread for the channel of all users, which can be expressed as $\tau_{\max} = \frac{l_{\max}}{M\Delta f}$. The setting method of l_p guarantees that the last row of the received delay-Doppler domain matrix is unaffected by interference from channel-impaired information symbols, facilitating channel estimation using this row. Thus, the first $M - l_p$ rows are the data symbols, and the last l_p rows are pilot symbols. Without loss of generality, we assume all of the pilot symbols as zadoff chu symbols (ZC symbols), which can be expressed as $X^{(n)}[l,k] = \exp\left[-j\pi q\frac{k^2}{N}\right]$ for the n-th user for $l = M - l_p, \cdots, M-1$. Each pilot row is assigned a unique root index q to minimize the mutual coherence of the dictionary matrix, thereby improving the system performance. We set the average power of the transmitted signal to one. To obtain the delay-time domain signal, we need to use an inverse discrete Zak transform from the DD domain matrix, which can be expressed as [107]

$$\begin{aligned} \mathrm{s}^{(n)} = \mathrm{s}_d^{(n)} + \mathrm{s}_p^{(n)} = \mathrm{IDZT}(\mathrm{X}^{(n)}) = \\ \mathrm{vec}\left(\mathrm{X}^{(n)}\mathrm{F}_N^H\right) = \left(\mathbf{F}_N^H \otimes \mathbf{I}_M\right)\mathrm{x}^{(n)}, \end{aligned} \tag{5.2}$$

where $x^{(n)}$ is the received symbol vectors of the n-th user as

$$\mathbf{x}^{(n)} = \begin{bmatrix} \mathbf{x}_0^{(n)} \\ \vdots \\ \mathbf{x}_{M-1}^{(n)} \end{bmatrix} = \mathrm{vec}\left(\mathbf{X}^{(n)\mathrm{T}}\right), \tag{5.3}$$

where $\mathbf{x} \in \mathbb{C}^{NM\times 1}$ is the transmitted symbol vector of the nth user. The pilot symbols are distinguishable from the data symbols. In each M-sample OTFS sub-symbol of the time-domain signal, the last l samples are allocated as the pilot symbols. To eliminate inter-frame interference, $l_a dd$ symbols can be used to detect non-interference pilot signals in $\mathrm{s}^{(n)}$.

5.1.4 Channel Estimation Model

Without loss of generality, we explain the details for the n-th user in the latter part of this section. The DD domain channel can be expressed as the mathematical formula as

$$h^{(n)}(\tau,\nu) = \sum_{i=1}^{Q} h_i^{(n)}\delta\left(\tau - \tau_i^{(n)}\right)\left(\nu - \nu_i^{(n)}\right), \tag{5.4}$$

The $\left\{h_i^{(n)}\right\}_{i=1}^{Q}$ represents the channel coefficients by its value and shows the Doppler spread and delay spread by the location of $\nu_i^{(n)}$ and $\tau_i^{(n)}$ where $Q = (l_{\max}+1)(2k_{\max}+1)$ and $k_{\max}$ is the maximum Doppler spread of the channel, where $\nu_{\max} = \frac{k_{\max}}{NT}$. It is a sparse matrix and can be solved by compressive sensing problems, and we can obtain the input-output relationship by

$$\begin{aligned} \mathrm{r}^{(n)} = \mathrm{Hs}^{(n)} + \mathrm{w}^{(n)} = \mathrm{H}^{(\mathrm{n})}\mathrm{s}_d^{(n)} + \\ \mathrm{H}^{(\mathrm{n})}\mathrm{s}_p^{(n)} + \mathrm{w}^{(\mathrm{n})} = \mathrm{r}_d^{(n)} + \mathrm{r}_p^{(n)} + \mathrm{w}^{(\mathrm{n})}, \end{aligned} \tag{5.5}$$

where $\mathbf{w}^{(n)} \in \mathbb{C}^{MN\times 1}$ denotes the noise vector, $\mathbf{H}^{(n)} \in \mathbb{C}^{MN\times MN}$ shows the time-domain channel matrix, $r_d^{(n)}$ and $r_p^{(n)}$ denote the data and pilot vectors, respectively. Specifically, we can rewrite the channel formula as the following expression

$$\mathbf{H}^{(n)} = \sum_{i=1}^{Q} h_i^{(n)} \Pi^{l_i} \Delta^{k_i} \tag{5.6}$$

where $\Pi \in \mathbb{C}^{MN\times MN}$ denotes the standard permutation matrix, and $\Delta = \mathrm{diag}\left(z^0, z^1, \cdots, z^{MN-1}\right) \in \mathbb{C}^{MN\times MN}$ stands for the diagonal Doppler matrix, and $z = e^{j2\pi/(MN)}$. We utilize the channel-impaired pilot samples in $r^{(n)}$ to estimate the channel. Subsequently, an MRC detector is applied to the received signal to detect the information symbols. This is facilitated by our pilot signal, which supports the use of a soft MRC detector. After substituting (5.6) to (5.5), we can obtain the equation as

$$\begin{aligned} \mathbf{r}^{(n)} = \left[\Psi_1^{(n)}, \Psi_2^{(n)}, \cdots, \Psi_Q^{(n)}\right]\mathbf{h}^{(n)} + \mathrm{w}^{(n)} \\ = \Psi \mathrm{h}^{(n)} + \mathrm{w}^{(n)} = \Psi_d^{(n)}\,\mathrm{h}^{(n)} + \Psi_p^{(n)}\,\mathrm{h}^{(n)} + \mathrm{w}^{(n)}, \end{aligned} \tag{5.7}$$

where $\Psi_i^{(n)} = \Pi^{l_i}\Delta^{k_i}\,\mathrm{s}^{(n)} \in \mathbb{C}^{MN\times 1}$, $\mathrm{h} \in \mathbb{C}^{Q\times 1}$ denotes time domain signal matrix, We denote the delay and Doppler locations according to the following rules:

$$\begin{cases} l_i = \mathrm{mod}\,(i-1, l_{\max}+1) \\ k_i = \mathrm{floor}\left(\frac{i-1}{l_{\max}-1}\right), \text{ if floor } \left(\frac{i-1}{l_{\max}-1}\right) \le k_{\max} \\ k_i = \mathrm{floor}\left(\frac{i-1}{l_{\max}-1}\right) \\ -(2k_{\max}+1), \text{ if floor } \left(\frac{i-1}{l_{\max}-1}\right) > k_{\max} \end{cases} \tag{5.8}$$

In OTFS, we [107] have set the length of the pilot signal to be longer than $l_{\max}$ to be out of interference, and, since $l_{zp} = l_{\max} + l_{add}$, we can use the last rows l_{add} of the signals to estimate the channel as they are free of interference from the velocity signal and can be used into the channel estimation. We denote them as r'_p and use a λ matrix to extract them. The extraction matrix can be expressed as follows:

$$\lambda = \left[\begin{array}{cccc} \lambda_0^T, & \lambda_1^T, & \ldots, & \lambda_{Nl_{add}-1}^T \end{array}\right]^T \tag{5.9}$$

where $\lambda_i^T \in \mathbb{C}^{MN\times 1}$ is a vector, for $i = 0, \ldots, Nl_{add}-1$ whose floor $\left(\frac{i}{l_{\text{add}}}\right) M +$ mod (i, N)-th element is 1 and other elements are all 0. Therefore, we can obtain the following expression:

$$\begin{aligned} \lambda \mathrm{r}^{(n)} = \lambda \Psi^{(n)} \mathrm{h}^{(n)} + \lambda \mathrm{w}^{(n)} = \\ \lambda \left(\Psi_{\mathrm{d}}^{(n)} + \Psi_{\mathrm{p}}^{(n)}\right) \mathrm{h}^{(n)} + \lambda \mathrm{w}^{(n)} = \Psi_p^{(n)\prime} \mathrm{h}^{(n)} + \mathrm{w}^{(n)\prime}, \end{aligned} \tag{5.10}$$

where $\lambda \mathbf{\Psi_{vel}} \mathbf{h} = 0^{N\times 1}$ and $\lambda \Psi_p \mathrm{h}$ will only remain the information of the last l_{add} lines of the pilot signal, $\mathbf{\Psi'}_p \in \mathbb{C}^{Nl_{add}\times Q}$ is the non-interference time domain pilot matrix. We denote the remaining part of the signal, and it is generated by the last l_{add} rows of the pilot signals as $\mathbf{r'}_p$, so we denote the signal we need at the estimation part as

$$\mathbf{r}_p^{(n)\prime} = \mathbf{\Psi}_p^{(n)\prime} \mathbf{h}^{(n)} + \mathbf{w}^{(n)\prime} \in \mathbb{C}^{l_{add}N\times 1}. \tag{5.11}$$

Under this formula, we will have different pilots in different positions, and we can choose them as we want because they are also separate in the time domain and extracted by our formula (5.11). Then, the channel vector is estimated using the Orthogonal Matching Pursuit (OMP) algorithm, a widely adopted sparse recovery method. The OMP algorithm can be applied to equation (5.7). In this study, we chose the OMP algorithm for its computational efficiency, owing to its low complexity and ability to deliver accurate results. We will not illustrate the OMP algorithm for the page limit, and since it is a widely used method, it can be researched in multitudinous references.

5.1.5 Iterative Successive Interference Cancellation Detection

In this section, we will introduce the Iterative successive interference cancellation detection to obtain the signal from different users. The received signal r_{sum} is the superposition of all signal from different users as

$$\mathbf{r}_{sum} = \sum_{n=1}^{K} \mathbf{r}^{(\mathbf{n})}. \tag{5.12}$$

Without loss of generality, we assume that the power of the K-th users have different values $P^{(n)}$, so we can give an order when comparing them. To use the iterative successive interference cancellation detection method, we first define a set to note the calculated user α and then find the user index that has the strongest power as

$$n_0 = \arg\max \left\{P^{(1)}, P^{(2)} \cdots, P^{(n)}\right\}, \tag{5.13}$$

then we add the user n_0 to the set α and eliminate $P^{(n_0)}$ from the user group in the iterative steps. Then we use OMP algorithm to calculate channel parameters, including channel coefficient, delay and Doppler using the received signal, power as the following expression

$$\hat{h}^{(n_0)}, \hat{\tau}^{(n_0)}, \hat{\upsilon}^{(n_0)} = \mathrm{OMP}(\mathbf{r}_{sum} - \sum_{\alpha} \mathbf{r}^{(n_0)}, P^{(n_0)}, \mathbf{\Psi}_p^{(n_0)'}), \tag{5.14}$$

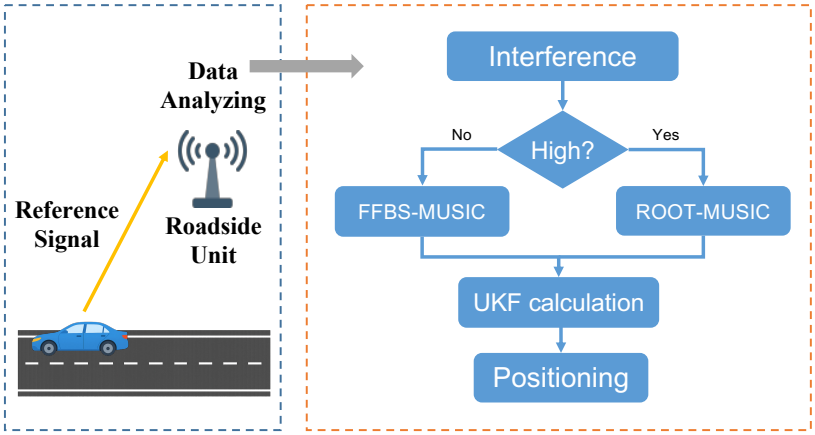


Fig.5.2: The adaptive music framework.

then we use the estimated channel parameters to receive the data taking advantage of MRC by using the formula as

$$\hat{\mathbf{r}}^{(\mathbf{n})} = \mathrm{MRC}(\mathbf{r}_{sum} - \sum_{\alpha} \mathbf{r}^{(n_0)}, \hat{h}^{(n_0)}, \hat{\tau}^{(n_0)}, \hat{\upsilon}^{(n_0)}). \tag{5.15}$$

After completing all of the users in the iterations, we will obtain the data from all of the users. Then, we summarize the algorithm in **Algorithm 3**.

5.2 Adaptive DoA Estimation Based on FBSS/Root-MUSIC

5.3 System Model

5.3.1 Description

We consider bearing-only vehicle localization using a roadside unit (RSU) equipped with a uniform linear array (ULA) as shown in Fig .5.2. The array front-end produces a DOA estimate that is fed to a state estimator (UKF). All equations are presented in order.

5.3.2 Vehicle Acceleration Model

The 2-D state is

$$\mathbf{x}_k \triangleq \begin{bmatrix} x_k & y_k & v_{x,k} & v_{y,k} & a_{x,k} & a_{y,k} \end{bmatrix}^{\top} \in \mathbb{R}^6. \tag{5.16}$$

With sampling period Δt, the motion model is

$$\mathbf{x}_{k+1} = \mathbf{F}\,\mathbf{x}_k + \mathbf{w}_k, \qquad \mathbf{w}_k \sim \mathcal{N}(\mathbf{0}, \mathbf{Q}), \tag{5.17}$$

$$\mathbf{F} = \begin{bmatrix} 1 & 0 & \Delta t & 0 & \frac{1}{2}\Delta t^2 & 0 \\ 0 & 1 & 0 & \Delta t & 0 & \frac{1}{2}\Delta t^2 \\ 0 & 0 & 1 & 0 & \Delta t & 0 \\ 0 & 0 & 0 & 1 & 0 & \Delta t \\ 0 & 0 & 0 & 0 & 1 & 0 \\ 0 & 0 & 0 & 0 & 0 & 1 \end{bmatrix}. \tag{5.18}$$

Let the RSU position be $\mathbf{s} = [s_x, s_y]^\top$. The planar bearing is

$$\theta_k \triangleq h(\mathbf{x}_k) = \operatorname{atan2}(y_k - s_y,\ x_k - s_x). \tag{5.19}$$

The tracker receives a noisy bearing

$$z_k = \theta_k + v_k, \qquad v_k \sim \mathcal{N}(0, R_\theta). \tag{5.20}$$

5.3.3 Array Signal Model with Interference

We consider a uniform linear array (ULA) of M antennas with inter-element spacing d and wavelength λ. At time step k, the received snapshot at the array can be written as

$$\mathbf{x}_k[\ell] = \mathbf{a}(\theta_k)\, s_k[\ell] \ + \ \mathbf{a}(\theta_{j,k})\, j_k[\ell] \ + \ \mathbf{w}_k[\ell], \tag{5.21}$$

where $\ell = 1, 2, \ldots, L$ is the snapshot index within time step k, with L total snapshots, θ_k is the direction-of-arrival (DOA) of the desired vehicle signal, $\theta_{j,k}$ is the DOA of the jammer (interferer), $s_k[\ell] \in \mathbb{C}$ is the baseband symbol of the desired signal at snapshot ℓ, $j_k[\ell] \in \mathbb{C}$ is the interfering (jammer) signal at snapshot ℓ, $\mathbf{a}(\theta) \in \mathbb{C}^M$ is the ULA steering vector, defined as

$$\mathbf{a}(\theta) = \begin{bmatrix} 1 & \cdots & e^{j(M-1)\psi(\theta)} \end{bmatrix}^\top, \quad \psi(\theta) = \frac{2\pi d}{\lambda}\sin(\theta), \tag{5.22}$$

$\mathbf{w}_k[\ell] \sim \mathcal{CN}(\mathbf{0}, \sigma_w^2 \mathbf{I}_M)$ is additive white Gaussian noise (AWGN). The covariance matrix of the received signal at time step k is then

$$\widehat{\mathbf{R}}_{xx,k} = \frac{1}{L}\sum_{\ell=1}^{L} \mathbf{x}_k[\ell]\mathbf{x}_k[\ell]^H. \tag{5.23}$$

For subarray length m and $K = M - m + 1$ shifts, let $\mathbf{X}_{i,k} \in \mathbb{C}^{m \times L_k}$ be snapshots from subarray i. The FBSS covariance is

$$\widehat{\mathbf{R}}_{\mathrm{FBSS},k} = \frac{1}{K}\sum_{i=1}^{K} \frac{1}{L_k}\mathbf{X}_{i,k}\mathbf{X}_{i,k}^H. \tag{5.24}$$

Forward–backward averaging (FBA) uses the *exchange matrix* $\mathbf{J}_m \in \{0,1\}^{m\times m}$ defined by

$$[\mathbf{J}_m]_{i,j} = \begin{cases} 1, & i+j = m+1, \\ 0, & \text{otherwise}, \end{cases} \tag{5.25}$$

which flips a vector (or matrix) along its anti-diagonal and satisfies $\mathbf{J}_m^{-1} = \mathbf{J}_m^H = \mathbf{J}_m$. The FBA covariance is then

$$\widehat{\mathbf{R}}_{\mathrm{FBA},k} = \tfrac{1}{2}\Big(\widehat{\mathbf{R}}_{\mathrm{FBSS},k} + \mathbf{J}_m\, \widehat{\mathbf{R}}^{*}_{\mathrm{FBSS},k}\, \mathbf{J}_m\Big). \tag{5.26}$$

Let $\mathbf{X}_k \in \mathbb{C}^{M\times L_k}$ denote the k-th block of array snapshots and

$$\widehat{\mathbf{R}}_{xx,k} \triangleq \frac{1}{L_k}\mathbf{X}_k\mathbf{X}_k^H \in \mathbb{C}^{M\times M}. \tag{5.27}$$

The M-element ULA has steering vector

$$\mathbf{a}(\theta) = \big[1,\, e^{\jmath\psi},\, \ldots,\, e^{\jmath(M-1)\psi}\big]^{\top}, \qquad \psi = \tfrac{2\pi d}{\lambda}\sin\theta. \tag{5.28}$$

From the eigendecomposition of a chosen covariance matrix $\widehat{\mathbf{R}}_k$, either $\widehat{\mathbf{R}}_{xx,k}$, $\widehat{\mathbf{R}}_{\mathrm{FBSS},k}$, or $\widehat{\mathbf{R}}_{\mathrm{FBA},k}$, extract the noise subspace $\mathbf{E}_n$. Then we choose a subarray length $m\,(P{+}1 \le m \le M)$ and $K = M - m + 1$ overlapping contiguous subarrays. Let $\mathbf{S}_i \in \mathbb{R}^{m\times M}$ be the i-th selection matrix that extracts sensors $\{i, \ldots, i+m-1\}$, i.e.,

$$\mathbf{S}_i \triangleq \begin{bmatrix} \mathbf{0}_{1\times(i-1)} & 1 & \cdots & 0 & \mathbf{0}_{1\times(M-i)} \\ \vdots & & \ddots & & \vdots \\ \mathbf{0}_{1\times(i-1)} & 0 & \cdots & 1 & \mathbf{0}_{1\times(M-i)} \end{bmatrix}. \tag{5.29}$$

Define the *forward-smoothed* covariance and the *backward* (conjugate-reversed) one as

$$\begin{cases} \widehat{\mathbf{R}}_{\mathrm{F},k} = \dfrac{1}{K}\displaystyle\sum_{i=1}^{K} \mathbf{S}_i\, \widehat{\mathbf{R}}_{xx,k}\, \mathbf{S}_i^H, \quad \widehat{\mathbf{R}}_{\mathrm{F},k} \in \mathbb{C}^{m\times m}, \\ \widehat{\mathbf{R}}_{\mathrm{B},k} = \dfrac{1}{K}\displaystyle\sum_{i=1}^{K} \mathbf{J}_m\, \mathbf{S}_i^{*}\, \widehat{\mathbf{R}}^{*}_{xx,k}\, \mathbf{S}_i^{\top}\mathbf{J}_m, \quad \widehat{\mathbf{R}}_{\mathrm{B},k} \in \mathbb{C}^{m\times m}. \end{cases} \tag{5.30}$$

where $\mathbf{J}_m$ is the $m\times m$ exchange matrix with ones on the anti-diagonal. The *forward–backward averaged* FBSS covariance is

$$\begin{aligned} \widehat{\mathbf{R}}_{\mathrm{FBSS},k} &\triangleq \frac{1}{2}\big(\widehat{\mathbf{R}}_{\mathrm{F},k} + \widehat{\mathbf{R}}_{\mathrm{B},k}\big) \\ &= \frac{1}{2K}\sum_{i=1}^{K}\Big(\mathbf{S}_i\, \widehat{\mathbf{R}}_{xx,k}\, \mathbf{S}_i^H \\ &\qquad + \mathbf{J}_m\, \mathbf{S}_i^{*}\, \widehat{\mathbf{R}}^{*}_{xx,k}\, \mathbf{S}_i^{\top}\mathbf{J}_m\Big). \end{aligned} \tag{5.31}$$

FBSS restores the covariance rank under coherent sources and mitigates jammer/multipath correlation. In practice one may optionally apply diagonal loading: $\widehat{\mathbf{R}}_{\mathrm{FBSS},k} \leftarrow \widehat{\mathbf{R}}_{\mathrm{FBSS},k} + \epsilon\,\mathrm{tr}(\widehat{\mathbf{R}}_{\mathrm{FBSS},k})\mathbf{I}_m/m$.

In what follows, $\widehat{\mathbf{R}}_k$ can be either the un-smoothed $\widehat{\mathbf{R}}_{xx,k}$ ($M\times M$) or the FBSS covariance $\widehat{\mathbf{R}}_{\mathrm{FBSS},k}$ ($m \times m$). Perform EVD $\widehat{\mathbf{R}}_k = \mathbf{E}\mathbf{\Lambda}\mathbf{E}^H$ and take the noise-subspace basis $\mathbf{E}_n$ (dimension $M-P$ or $m-P$ accordingly).

■MUSIC:

$$P_{\mathrm{MU}}(\theta) = \frac{1}{\mathbf{a}(\theta)^H \mathbf{E}_n \mathbf{E}_n^H \mathbf{a}(\theta)}, \qquad \widehat{\theta}_k = \arg\max_{\theta\in\Theta} P_{\mathrm{MU}}(\theta). \tag{5.32}$$

(When FBSS is used, replace $\mathbf{a}(\theta)$ by the m-element subarray steering vector.)

■Root-MUSIC (ULA): Let $\mathbf{b}_r(z) = [1, z, \ldots, z^{r-1}]^\top$ with $r = M$ (no smoothing) or $r = m$ (FBSS). Define the noise projector $\mathbf{P}_n = \mathbf{E}_n\mathbf{E}_n^H$ and the polynomial

$$\begin{cases} q(z) = \mathbf{b}_r(z)^H\, \mathbf{P}_n\, \mathbf{b}_r(z) = \displaystyle\sum_{\ell=-(r-1)}^{r-1} c_\ell\, z^{-\ell}, \\ \\ c_\ell \triangleq \displaystyle\sum_{\substack{1\le i,j\le r \\ j-i=\ell}} [\mathbf{P}_n]_{i,j}. \end{cases} \tag{5.33}$$

Let $\{z_i\}$ be the roots of the associated conjugate-symmetric polynomial (in z). The P roots closest to the unit circle ($|z_\star| \approx 1$) yield spatial frequencies $\widehat{\psi}_k = \arg(z_\star)$ and DoAs

$$\widehat{\theta}_k = \arcsin\Big(\frac{\widehat{\psi}_k}{2\pi d/\lambda}\Big). \tag{5.34}$$

In FBSS-Root-MUSIC, use $r = m$ and the FBSS covariance to form $\mathbf{E}_n$, which confers robustness against coherent multipath and strong interferers.

Given an interference threshold Γ, the DOA front-end is chosen as

$$\widehat{\theta}_k = \begin{cases} \widehat{\theta}_k^{\text{Root-MUSIC}}(\widehat{\mathbf{R}}_{xx,k}), & \text{if } \mathrm{INR}_k \le \Gamma, \\ \widehat{\theta}_k^{\text{FBSS-Root}}(\widehat{\mathbf{R}}_{\mathrm{FBA},k}), & \text{if } \mathrm{INR}_k > \Gamma. \end{cases} \tag{5.35}$$

5.3.4 Tracking with Unscented Kalman Filter (UKF)

To estimate the vehicle trajectory from the noisy DoA measurements, we employ the Unscented Kalman Filter (UKF). The UKF is well-suited for nonlinear systems, as it propagates a set of deterministically chosen *sigma points* through the nonlinear functions instead of relying on Jacobian linearization as in the EKF.

Algorithm 3 Adaptive DoA-Based Vehicular Localization Framework

Require: Received snapshots $\mathbf{X}$; array parameters; interference threshold γ; previous vehicle state $\hat{\mathbf{x}}_{k-1}$

Ensure: Estimated vehicle state $\hat{\mathbf{x}}_k$

Step 1: Signal preprocessing
Compute the covariance matrix $\mathbf{R}_{xx} \leftarrow \frac{1}{L}\mathbf{X}\mathbf{X}^H$
Estimate the SINR from $\mathbf{R}_{xx}$
Step 2: Adaptive DoA estimation
if SINR $> \gamma$ **then** ▷ Low-interference regime
    Apply Root-MUSIC to estimate the DoA $\hat{\theta}_k$
else ▷ High-interference regime
    Apply FBSS followed by Root-MUSIC to estimate the DoA $\hat{\theta}_k$
end if
Step 3: State update with UKF
Convert the DoA measurement $\hat{\theta}_k$ into a bearing observation z_k
Perform the UKF prediction and update steps to obtain the new vehicle state $\hat{\mathbf{x}}_k$
return $\hat{\mathbf{x}}_k$

State Transition Model

The system state vector is defined as

$$\mathbf{x}_k = \begin{bmatrix} x_k & y_k & v_{x,k} & v_{y,k} & a_{x,k} & a_{y,k} \end{bmatrix}^T, \tag{5.36}$$

where (x_k, y_k) is the position, $(v_{x,k}, v_{y,k})$ is the velocity, and $(a_{x,k}, a_{y,k})$ is the acceleration.

The nonlinear state transition is given by

$$\begin{cases} x_{k+1} = x_k + v_{x,k}\Delta t + \frac{1}{2}a_{x,k}\Delta t^2, \\ y_{k+1} = y_k + v_{y,k}\Delta t + \frac{1}{2}a_{y,k}\Delta t^2, \\ v_{x,k+1} = v_{x,k} + a_{x,k}\Delta t, \\ v_{y,k+1} = v_{y,k} + a_{y,k}\Delta t, \\ a_{x,k+1} = a_{x,k}, \quad a_{y,k+1} = a_{y,k}. \end{cases} \tag{5.37}$$

This can be compactly written as

$$\mathbf{x}_{k+1} = f(\mathbf{x}_k) + \mathbf{q}_k, \quad \mathbf{q}_k \sim \mathcal{N}(\mathbf{0}, \mathbf{Q}), \tag{5.38}$$

where $\mathbf{Q}$ is the process noise covariance.

Measurement Model

The RSU located at $\mathbf{s} = (s_x, s_y)$ measures the bearing angle θ_k as

$$z_k = h(\mathbf{x}_k) + w_k, \tag{5.39}$$

with

$$h(\mathbf{x}_k) = \arctan\left(\frac{y_k - s_y}{x_k - s_x}\right), \quad w_k \sim \mathcal{N}(0, R). \tag{5.40}$$

UKF Prediction Step

First, sigma points are generated from the prior estimate:

$$\begin{cases} \chi_{k-1}^{i} = \mathbf{x}_{k-1|k-1} + \left(\sqrt{(n+\lambda)\mathbf{P}_{k-1|k-1}}\right)_i, \\ \chi_{k-1}^{i+n} = \mathbf{x}_{k-1|k-1} - \left(\sqrt{(n+\lambda)\mathbf{P}_{k-1|k-1}}\right)_i, \end{cases} . \tag{5.41}$$

for $i = 1, \ldots, n$, where n is the state dimension and λ is a scaling parameter.

Each sigma point is propagated through the state transition:

$$\chi_{k|k-1}^{i} = f(\chi_{k-1}^{i}). \tag{5.42}$$

The predicted mean and covariance are then obtained as

$$\begin{cases} \mathbf{x}_{k|k-1} = \sum_{i=0}^{2n} W_i^{(m)} \chi_{k|k-1}^{i}, \\ \mathbf{P}_{k|k-1} = \sum_{i=0}^{2n} W_i^{(c)} \left(\chi_{k|k-1}^{i} - \mathbf{x}_{k|k-1}\right)\left(\chi_{k|k-1}^{i} - \mathbf{x}_{k|k-1}\right)^T \\ +\mathbf{Q}. \end{cases} \tag{5.43}$$

UKF Update Step

The propagated sigma points are transformed into the measurement domain:

$$\zeta_{k|k-1}^{i} = h(\chi_{k|k-1}^{i}). \tag{5.44}$$

Then, the predicted measurement and its covariance are computed as

$$\begin{cases} \hat{z}_{k|k-1} = \sum_{i=0}^{2n} W_i^{(m)} \zeta_{k|k-1}^{i}, \\ S_k = \sum_{i=0}^{2n} W_i^{(c)} \left(\zeta_{k|k-1}^{i} - \hat{z}_{k|k-1}\right)^2 + R. \end{cases} \tag{5.45}$$

Table5.1: The Page style Simulation parameters.

Parameter	Value
Carrier frequency	$f_c = 4\,\text{GHz}$
Subcarrier spacing	$\Delta f = 15\,\text{kHz}$
(M, N)	$(64, 32)$
Max. speed	$300\,\text{km/h}$
User amount K	2

The cross-covariance is

$$\mathbf{P}_{xz} = \sum_{i=0}^{2n} W_i^{(c)} \left(\chi_{k|k-1}^i - \mathbf{x}_{k|k-1}\right)\left(\zeta_{k|k-1}^i - \hat{z}_{k|k-1}\right)^T. \tag{5.46}$$

Finally, the Kalman gain and update equations are

$$\begin{cases} \mathbf{K}_k = \mathbf{P}_{xz} S_k^{-1}, \\ \mathbf{x}_{k|k} = \mathbf{x}_{k|k-1} + \mathbf{K}_k(z_k - \hat{z}_{k|k-1}), \\ \mathbf{P}_{k|k} = \mathbf{P}_{k|k-1} - \mathbf{K}_k S_k \mathbf{K}_k^T. \end{cases} \tag{5.47}$$

And we summrize the idea into the Algorithm 1 in the paper.

5.4 Results for Page-style

Based on the OTFS modulation structure and the previously developed adaptive DoA estimation and filtering mechanisms, a scalable system model was formulated to support simultaneous vehicle transmissions under shared spectrum access.

To address the mutual interference introduced by concurrent users, an iterative symbol-level SIC structure was adopted. The OTFS sparsity property, together with the OMP-based channel estimation, enabled reliable reconstruction of individual user signals even in the presence of overlapping delay–Doppler components. Furthermore, the FBSS/Root-MUSIC-based adaptive DoA estimator—originally designed for interference-varying NLoS cases—was successfully extended to the multi-vehicle case, demonstrating robustness against varying mobility levels and Doppler dynamics. The estimated angular information was then incorporated into a UKF-based tracking framework for maintaining accurate multi-user trajectory reconstruction.

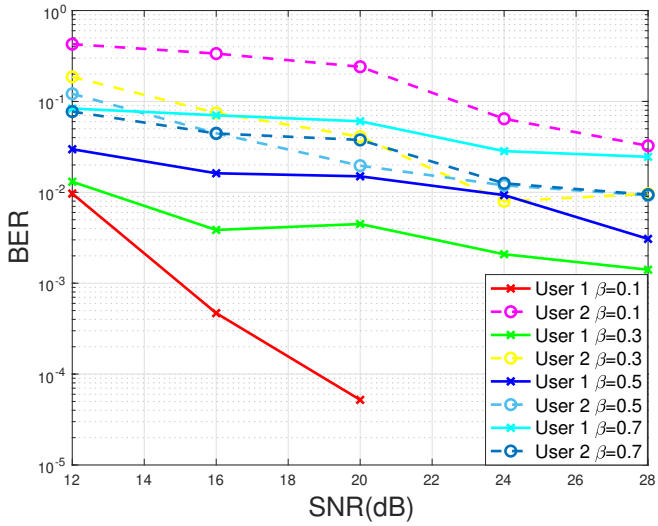


Fig.5.3: BER performance under different values of β for different users.

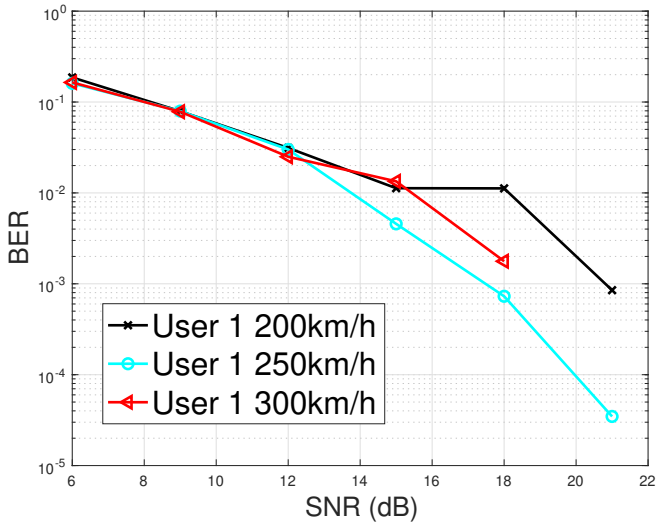


Fig.5.4: BER performance under different vehicle velocities.

5.4.1 Complexity

For the Complexity of the Proposed Method, the overall computational complexity of the Page-style OTFS receiver is primarily attributed to the following components: First, Delay-Doppler domain channel estimation using OMP is $O(K \cdot M \cdot N)$, where K is the number of non-zero delay-Doppler components (channel sparsity), and $M \times N$ is the size of the delay-Doppler grid. Successive interference cancellation (SIC) across U users can be written as $O(U \cdot M \cdot N)$, and finally

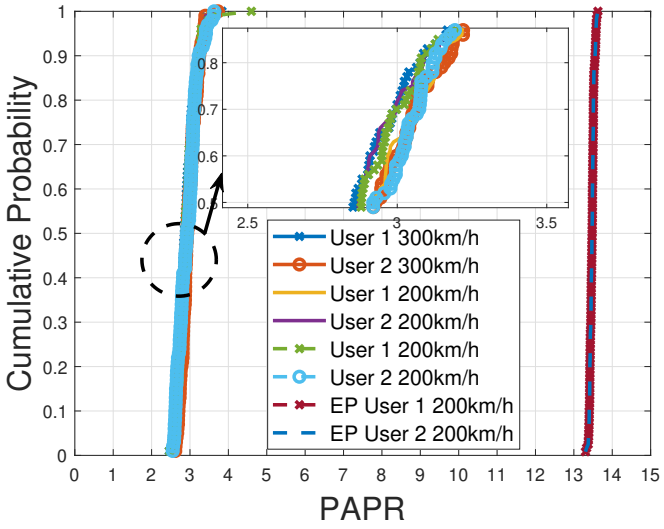


Fig.5.5: PAPR comparison between the proposed method and benchmark scheme EP.

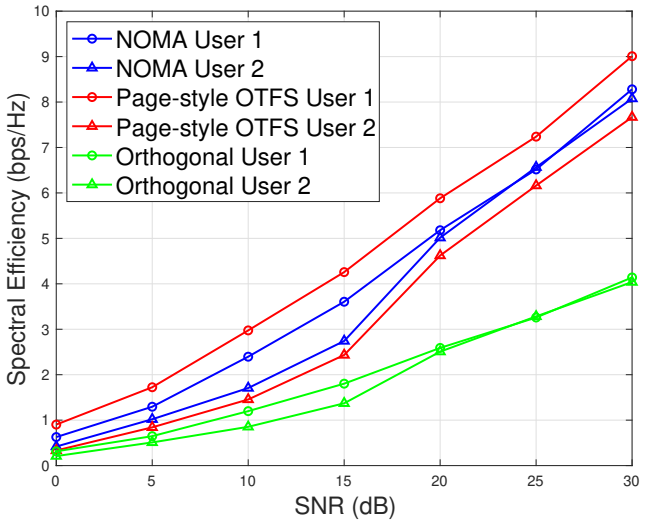


Fig.5.6: Spectral efficiency comparison with benchmark schemes.

MRC detection for each user can be summarized as $O(M \cdot N)$. Therefore, the overall complexity can be expressed as $O((K+U) \cdot M \cdot N)$. Second, regarding the Complexity of the Orthogonal Method (OMA), In the OMA baseline, each user occupies half of the time-frequency (or delay-Doppler) grid. Because no interference exists, there is no SIC, and the channel estimation and detection are performed independently per user, which can be expressed as $O(U \cdot M \cdot N/2)$, making OMA significantly simpler in implementation. As shown in Fig. 5.7, we investigate the BER performance of four users with different received power levels. User 1 is the strongest user, while

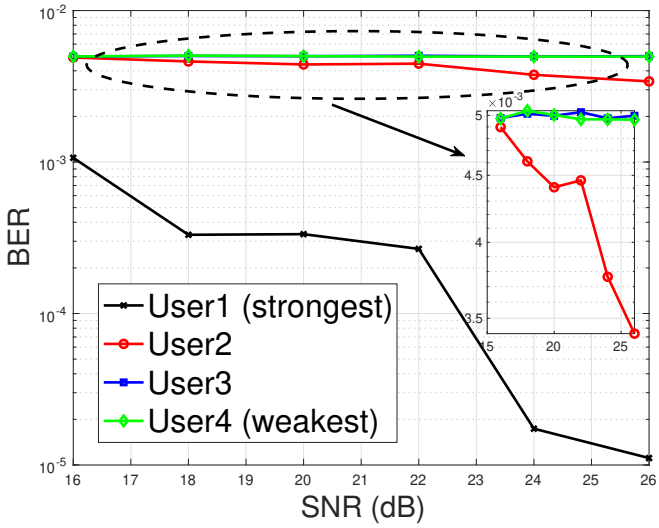


Fig.5.7: BER simulation result for the 4-user scenario.

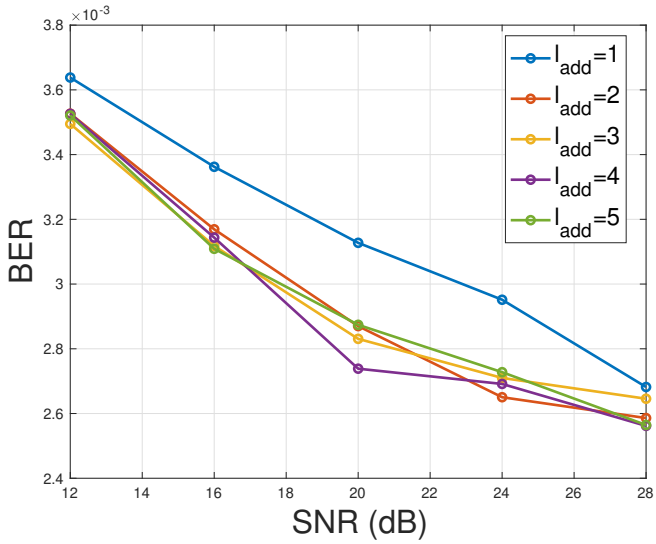


Fig.5.8: LAdd parameter comparison.

User 4 is the weakest one. It can be observed that the decoding order significantly affects the BER results: the strongest user achieves a BER down to 10^{-5} at high SNR, while the weaker users suffer from an error floor due to residual interference. This is consistent with the principle of successive interference cancellation (SIC), where stronger users can be decoded and cancelled first, thereby reducing the interference for subsequent users. These results confirm that the proposed receiver structure can effectively separate users with distinct power levels, though the weakest users still experience performance degradation.

As shown in Fig. 5.8, the BER performance varies with different choices of the additional guard length l_{add}. When l_{add} is too small, interference from delay spread cannot be fully mitigated, resulting in higher BER values. As l_{add} increases, the error rate improves since the system becomes more resilient to interference. However, the improvement tends to saturate beyond a certain point, indicating that overly large l_{add} does not bring further significant gains. These results highlight the importance of carefully selecting l_{add} to achieve a good trade-off between the performance and resource utilization.

Fig. 5.10 illustrates the simulation runtime of the proposed system with different numbers of users K and various values of the guard interval l_{add}. It can be observed that the runtime increases almost linearly with the number of users, as expected. Moreover, for a fixed number of users, a larger l_{add} results in higher computational cost, since more pilot and guard resources need to be processed. However, the overall runtime remains within practical limits (on the order of 10^{-4} seconds), showing that the proposed algorithm is feasible for real-time implementation. Fig. 5.9 shows the theoretical complexity analysis of the proposed scheme. The overall computational complexity can be expressed as

$$O(K \cdot (MN + l_{\text{add}} \cdot N)), \tag{5.48}$$

where K is the number of users, M and N denote the OTFS grid dimensions in delay and Doppler, and l_{add} represents the additional guard interval length. The results demonstrate that the complexity grows linearly with the number of users K, whereas increasing l_{add} reduces the effective number of available data symbols per user, thus leading to a relatively smaller normalized complexity per data symbol. This matches well with the measured runtime shown in Fig. 5.10, confirming the accuracy of our theoretical analysis.

This section presents the performance evaluation of the proposed method, with the simulation parameters listed in Table 5.1. We assume that there are 2 users in our scenario and use a power coefficient β to control the relationship that $P^{(2)} = \beta P^{(1)}$ and we set $P^{(1)}$ is greater than $P^{(2)}$, so β is always from 0 to 1.

Fig. 5.3 compares BER along different β, SNR for user 1 and user 2 when they both use the velocity of 100 km/h. Because User 1 has a larger transmit power, the BER always performs better than user 2. When the parameter β becomes smaller, the performance of User 2 will become worse for the smaller power compared to user 1, and when the parameter β becomes larger, user 2 will perform better, whereas user 1 will have a relatively low SNR compared to the lower β value. This can be considered as a trade-off problem to control the ratio of the power of different users, which will be discussed in our future work.

In Fig. 5.4, to show our method has robustness to velocity, we take user 1 as the instant and

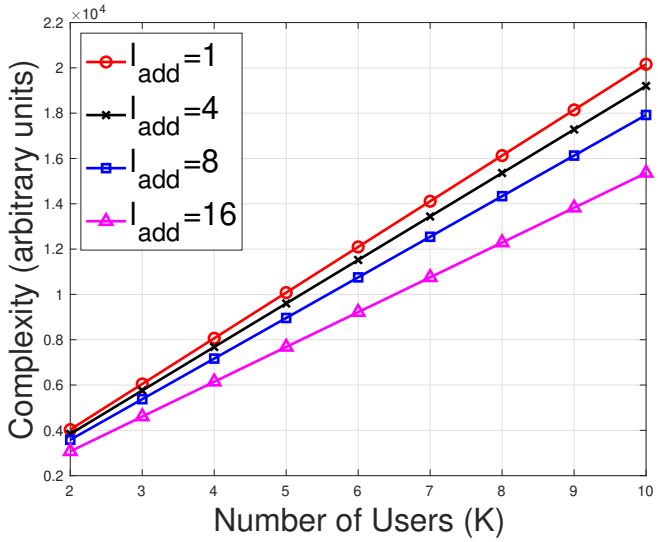


Fig.5.9: Theoretical runtime under different numbers of users K and guard interval lengths l_{add}.

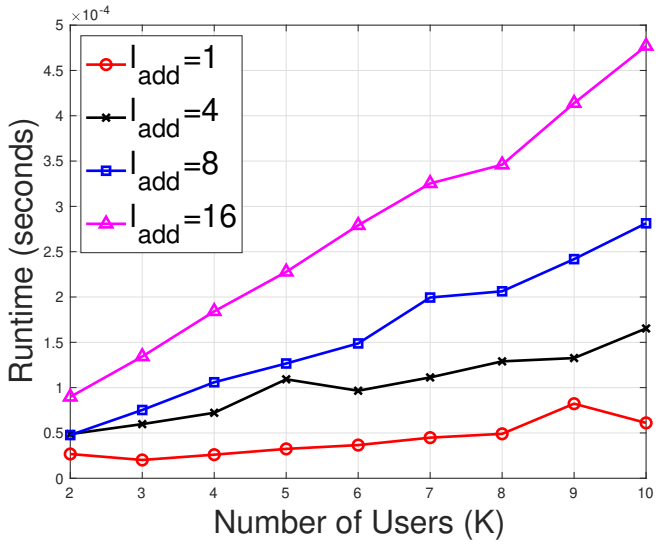


Fig.5.10: Measured computational complexity under different numbers of users K and guard interval lengths l_{add}.

compare the performance at different velocities as 200 km/h, 250 km/h, and 300 km/h, respectively. The results show that our method can guarantee availability under different velocities.

Fig. 5.5 compares the PAPR of our method with that of the embedded pilot method (EP) under different velocities and SNR. EP is a commonly used pilot structure in OTFS systems, where a single pilot symbol is embedded in the delay-Doppler grid. To avoid interference with the surrounding data symbols, zero-valued guard symbols are placed around the pilot symbols. The

Table5.2: Simulation parameters for adaptive MUSIC scenario.

Parameter	**Value**
Antenna spacing d	0.5λ
Snapshots (Seg. 1 / Seg. 2)	32/20
Interference angle	$-25° / -30°$
Process noise covariance Q	$0.01\mathbf{I}_6$
Measurement noise variance R	$(1°)$ (in radians)
Sampling interval Δt	0.02 s
Target motion model	Constant acceleration
Filtering methods	KF, EKF, UKF

data symbols are then transmitted to the remaining grid positions. This structure enables the pilot to coexist with the data symbols in the same OTFS frame. [51] Because of there are many pilot signals in our method, the pilot make the power more average so we have lower PAPR compared to EP method for both user 1 and user 2, which can protect the signal transmission from distortion.

Fig. 5.6 depicts the spectrum efficiency of our method and the common method when they use only orthogonal block resources. We also compare with the NOMA idea. We can see that the Page-style OTFS consistently outperforms NOMA across all SNR levels for user 1. This is because Page-style OTFS leverages a structured delay-Doppler pilot design and decodes users in power order, enabling better channel estimation and reduced interference, particularly for weak users. In contrast, NOMA suffers from SIC error propagation and a less effective use of the signal structure. The results demonstrate that Page-style OTFS provides higher spectral efficiency for both users compared to NOMA, particularly at high SNR, and our results show that the method has better spectrum efficiency than the OMA method because it reuses the same resource block and uses SIC to separate them.

5.5 Results for Adaptive MUSIC Framework

Then we give the numerical results of our model. Fig. 5.11 shows the RMSE performance of MUSIC, Root-MUSIC, and FBSS-MUSIC under different SNR conditions without interference. All three algorithms improve as SNR increases and converge to nearly identical accuracy above 3 dB. However, clear differences appear in the low-SNR region: conventional MUSIC suffers from large estimation errors, while Root-MUSIC achieves the best robustness and maintains small errors even below 0 dB. FBSS-MUSIC, although effective for interference suppression, incurs performance loss in this interference-free scenario due to reduced aperture and degrees of freedom. These results highlight that Root-MUSIC is preferable in noise-limited conditions, whereas FBSS

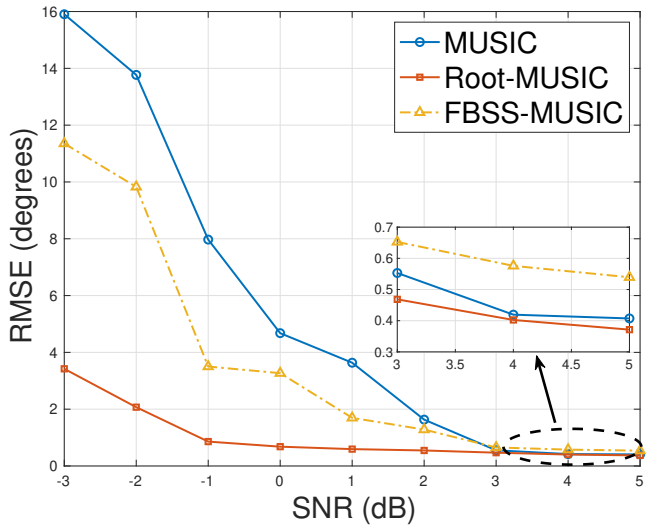


Fig.5.11: MUSIC RMSE without noise under different SNR.

should be reserved for interference-dominated environments.

Fig. 5.13 compares the NMSE of MUSIC, Root-MUSIC, and FBSS-Root-MUSIC in two segments: the first half with low SNR (2 dB) and no interference, and the second half with higher SNR (10 dB) but strong coherent interference (INR = 2 dB). In the first segment, Root-MUSIC outperforms the other methods due to its robustness in noise-limited conditions, while MUSIC exhibits larger errors and FBSS shows moderate performance. In the second segment, however, both MUSIC and Root-MUSIC degrade significantly in the presence of coherent interference, whereas FBSS-Root-MUSIC maintains stable and low error thanks to the spatial smoothing process. These results confirm the complementary strengths of Root-MUSIC and FBSS-Root-MUSIC: the former is more effective under low SNR without interference, while the latter is superior in interference-dominated environments.

The simulation results Fig. 5.12 demonstrate that the performance of FBSS-MUSIC strongly depends on the number of antennas. With a small array size ($M = 4$ or $M = 8$), the RMSE remains relatively high, especially under low SNR, indicating limited resolution and robustness. As the number of antennas increases ($M = 16$ and $M = 32$), the RMSE drops to nearly zero across the entire SNR range, showing that larger arrays significantly improve estimation accuracy and robustness. This confirms that spatial smoothing combined with sufficient aperture size enables FBSS-MUSIC to effectively suppress noise and interference, achieving reliable DoA estimation.

Fig. 5.14 illustrates the target trajectory estimation performance under different DOA–filtering schemes. The true trajectory is well preserved when FBSS-Root-MUSIC is combined with KF, EKF, or UKF, showing excellent robustness against interference and noise. In contrast, Root-

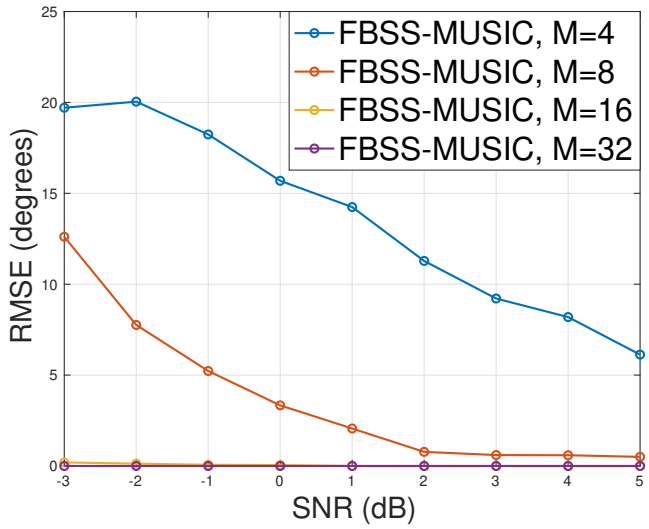


Fig.5.12: BSS-MUSIC DoA RMSE vs. SNR for Different Array Sizes.

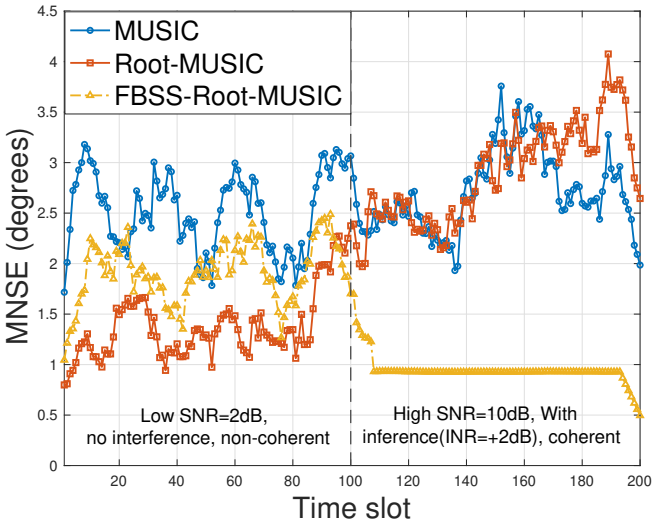


Fig.5.13: MUSIC NMSE without (0-T/2) and with noise (T/2-T).

MUSIC combined with KF or EKF suffers from severe deviations, particularly in the presence of interference, where trajectory divergence is observed. MUSIC-based methods show moderate tracking accuracy but remain less stable compared to FBSS. Notably, the UKF consistently provides the most accurate trajectory reconstruction across all DOA estimators, confirming its advantage in handling nonlinear bearing-only tracking. These results highlight that FBSS-Root-MUSIC with UKF achieves the most reliable trajectory recovery in practical interference conditions.

Fig. 5.15 shows the absolute position error for different DOA–filtering schemes. In the first

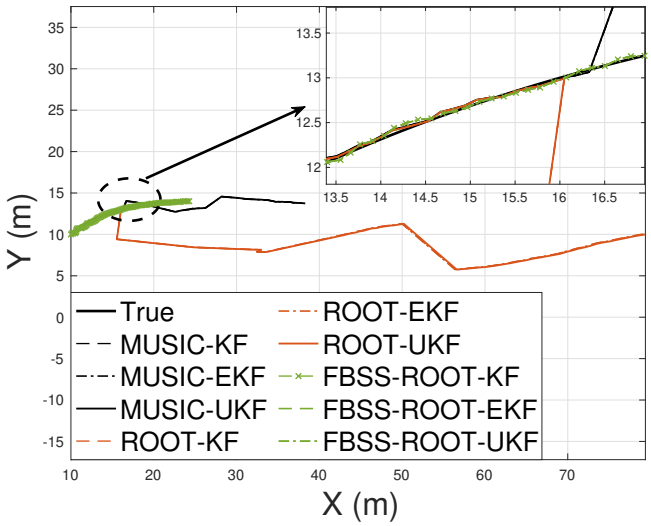


Fig.5.14: The trajectory under different scheme.

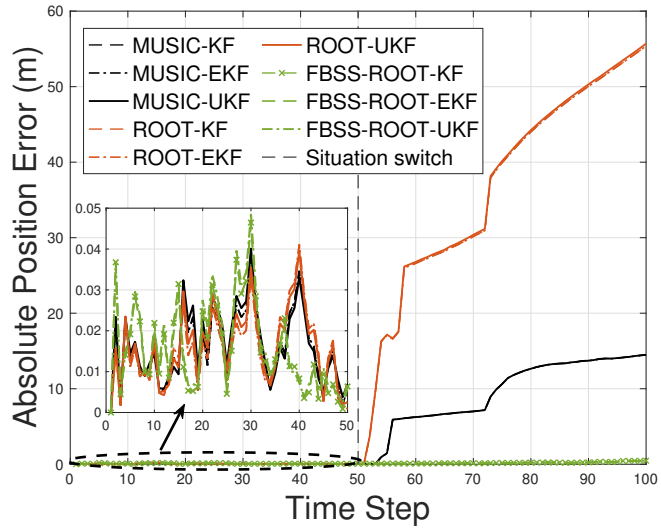


Fig.5.15: The trajectory error under different scheme.

half of the experiment (low SNR, no interference), all approaches achieve similar error levels, with Root-MUSIC and FBSS-Root-MUSIC combined with UKF providing slightly more stable performance. However, once strong interference is introduced (after the situation switch), Root-MUSIC-based filters quickly diverge, especially ROOT-UKF, leading to significant error accumulation. In contrast, FBSS-Root-MUSIC maintains consistently low error across all filters, with FBSS-Root-UKF achieving the best overall accuracy. This confirms that FBSS spatial smoothing effectively mitigates coherent interference, and its integration with UKF yields the most reliable

tracking performance in realistic scenarios.

Chapter 6

Conclusion and Future Work

6.1 Conclusion

This dissertation proposed and validated a unified vehicular localization framework capable of operating reliably under line-of-sight (LoS), non-line-of-sight (NLoS), and multi-user V2X scenarios. The main conclusions and validated findings are summarized as follows:

- **LoS-based localization performance:** A baseline vehicular localization scheme was established by integrating 2D-MUSIC-based angle-of-arrival estimation with an Unscented Kalman Filter (UKF) for vehicle state tracking. By explicitly modeling vehicle kinematics and measurement uncertainty, the proposed method achieved stable and accurate position estimation without relying on external positioning infrastructure such as GPS. Simulation results demonstrated that sub-meter-level localization accuracy can be maintained under moderate signal-to-noise ratios in mmWave-enabled intersection scenarios.
- **RIS-assisted OTFS localization under NLoS conditions:** To mitigate the loss of angular information caused by blockage and rich multipath propagation, the framework was extended using reconfigurable intelligent surfaces (RIS) combined with orthogonal time frequency space (OTFS) modulation. A low-PAPR (only about 21.5% of the conventional PAPR) pilot structure and MUSIC-based feature extraction enabled robust sensing in the delay–Doppler domain. Quantitative results showed that the proposed RIS-assisted OTFS scheme significantly outperformed conventional OFDM-based localization methods, achieving a reduction in positioning error while maintaining reliable tracking performance under high mobility and rapidly time-varying channels.
- **Scalable multi-user localization capability:** To support dense V2X deployments, a scalable multi-user extension was developed by combining iterative interference cancellation

with an adaptive MUSIC strategy that dynamically selects among conventional MUSIC, FBSS, and Root-MUSIC according to interference conditions and signal-to-noise ratio (SNR) levels. When integrated with UKF-based state fusion, the proposed framework preserved localization accuracy as the number of active users increased. Simulation results indicated that only a marginal degradation in positioning accuracy was observed compared to the single-user case, demonstrating strong robustness against inter-user interference.

Overall, extensive simulations across diverse propagation environments, vehicle dynamics, and user densities confirmed that the proposed framework achieves a favorable trade-off between localization accuracy, robustness, and computational complexity. By jointly leveraging channel structure, adaptive sensing, and mobility-aware filtering, this work provides a practical and extensible foundation for future cooperative and infrastructure-assisted V2X localization systems in scenarios where conventional satellite- or map-based positioning is unreliable or unavailable.

6.2 Future Work

Although the proposed framework has been validated through extensive simulations, several steps are still required for practical deployment. To facilitate a clear path toward real-world realization, we outline a step-by-step roadmap below. For each stage, we explicitly identify the challenges that remain open and the aspects investigated in this dissertation that require further verification or extension.

- **Stage I: Prototype implementation and measurement-driven validation (LoS/NLoS/multi-user).**
  Goal: Build a hardware-in-the-loop prototype and verify the end-to-end localization pipeline under realistic channels and mobility.
  Remaining challenges/open issues:
  (i) bridging the gap between simulated channel models and measurement-driven urban V2X propagation (e.g., non-stationary multipath, spatial consistency, blockage dynamics);
  (ii) sensitivity of 2D angle estimation (MUSIC/Root-MUSIC/FBSS) to array calibration errors, mutual coupling, phase noise, CFO, and imperfect synchronization;
  (iii) robustness of the UKF under model mismatch (e.g., non-constant velocity motion, lane changes, turning intersections) and the impact of delayed or intermittent observations.
- **Stage II: Real-time signal processing and computational feasibility.**
  Goal: Achieve real-time operation under practical latency and compute constraints for vehicular applications.

Remaining challenges/open issues:

(i) reducing the complexity of 2D spectrum search and adaptive mode switching among MUSIC/FBSS/Root-MUSIC while maintaining accuracy;

(ii) designing low-latency multi-user processing (e.g., iterative interference cancellation) with guaranteed convergence and bounded runtime;

(iii) joint scheduling of pilot/data resources in OTFS to balance sensing accuracy, PAPR constraints, and communication throughput.

- **Stage III: Closed-loop RIS control and joint communication–localization optimization.**

  Goal: Move from "static/assumed" RIS configurations to closed-loop, real-time RIS control that supports both sensing and communication.

  Remaining challenges/open issues:

  (i) practical RIS channel acquisition and overhead control (e.g., how frequently the RIS needs to be reconfigured under mobility);

  (ii) robust phase configuration under hardware impairments and limited RIS resolution, and its impact on delay–Doppler feature extraction;

  (iii) developing optimization policies that jointly consider localization error, link reliability, and reconfiguration latency.

- **Stage IV: Network-level scaling and cooperative V2X integration.**

  Goal: Extend the framework to distributed, cooperative operation in dense deployments and future 6G infrastructures.

  Remaining challenges/open issues:

  (i) fusion of multi-agent measurements (V2V/V2I) with consistent uncertainty modeling and outlier rejection under asynchronous reporting;

  (ii) scalable interference management across multiple links and RIS panels, beyond the single-cell setting considered in this dissertation;

  (iii) security, privacy, and reliability issues for cooperative localization, including resilience to malicious interference and spoofing.

Overall, this roadmap highlights that practical realization requires not only algorithmic advances, but also measurement-driven validation, real-time implementation, closed-loop RIS control, and network-level system design. Addressing these open issues will be essential to translate the proposed localization framework into deployable V2X localization services.

Publications

This section summarizes the publications produced during the doctoral study. They are grouped into two categories: papers directly contributing to the content of this dissertation and other external research outputs.

Publications Related to This Dissertation

R1. **Dou Hu**, Jin Nakazato, Javanmardi Ehsan, Kazuki Maruta, Rui Dinis, Manabu Tsukada, "DoA Estimation and Kalman Filter based Multi-Antenna System for Vehicle Position in mmWave Network," *IEEE Open Journal of Vehicular Technology*, 2025.

R2. **Dou Hu**, Jin Nakazato, Kazuki Maruta, Omid Abbassi Aghda, Rui Dinis, Manabu Tsukada, "OTFS-based RIS-assisted Vehicle Positioning and Tracking in V2X Scenario," *IEEE Transactions on Communications*, 2025.

R3. **Dou Hu**, Jin Nakazato, Kazuki Maruta, Rui Dinis, Omid Abbassi Aghda, Manabu Tsukada, "A Low PAPR Layered Multi-User OTFS Modulation," *The 2025 IEEE 101st Vehicular Technology Conference*, Oslo, Norway, 2025. (IEEE VTS Japan Chapter 2025 Young Researcher's Encouragement Award)

R4. **Dou Hu**, Jin Nakazato, Ehsan Javanmardi, Muhammad Asad, Kazuki Maruta, Manabu Tsukada, "A Research of Kalman Filter Enabled Beam Tracking for Multiple Vehicles," *ASPIRE Workshop*, IEICE General Conference, Hiroshima, Japan, 2024.

R5. **Dou Hu**, Pengfei Lin, Manabu Tsukada, "Robust Vehicle Localization Based on Adaptive DOA Estimation and UKF under Varying Interference Conditions," Las Vegas, U.S. *IEEE Consumer Communications & Networking Conference (CCNC)*, Poster, 2026.

Other Research Outputs (Not Directly Related to This Thesis)

O1. Kazuki Maruta, Jin Nakazato, Kengo Suzuki, **Dou Hu**, Ryo Iwaki, Sojin Ozawa, Yuki Sasaki, Hideya So, Manabu Tsukada, "Millimeter-Wave Fast Beam Tracking Enabled by RAN/V2X Cooperation," *ICAIIC*, Osaka, Japan, 2024. (Excellent Paper Award)

O2. Muhammad Asad, Saima Shaukat, **Dou Hu**, Zekun Wang, Ehsan Javanmardi, Jin Nakazato, Manabu Tsukada, "Limitations and Future Aspects of Communication Costs in Federated Learning: A Survey," *Sensors*, vol. 23, no. 17, 2023.

Acknowledgment

Acknowledgment

The completion of this dissertation marks an important milestone in my academic journey, and it would not have been possible without the support, guidance, and encouragement of many individuals and groups. I would like to express my sincere gratitude to all who have accompanied me throughout this work.

First and foremost, I would like to express my deepest appreciation to my advisor, Prof. Tsukada Manabu, for his continuous guidance, valuable insights, and unwavering support throughout this research. His vision in bridging wireless communication and intelligent transportation systems has shaped the direction of this dissertation and profoundly influenced my academic growth. His rigorous attitude toward research and encouragement to explore beyond existing boundaries have significantly benefited me both professionally and personally.

I would also like to extend my gratitude to the faculty and staff of the Tsukada Laboratory, whose expertise and dedication have contributed to a stimulating and supportive research environment. The interdisciplinary nature of this work—integrating communication theory, intelligent sensing, and AI-driven mobility applications—was made possible through the inspiring research culture cultivated within the laboratory. I am also grateful to the lab members Lin Pengfei, Tydus, Ehsan Javanmardi, Alex Orsholits, and Naren Bao, for their generous support, insightful discussions, and assistance not only during the preparation of this Ph.D. dissertation but also in daily life.

Special thanks go to my colleagues and fellow lab members, including Zhang Shangkai, Wu Hanlin, Chi Weiqi, Li Donghui, and many others, for their technical discussions, collaboration, and encouragement throughout the research process. The shared experience of experiments, debugging, paper deadlines, and countless discussions has created memories that I will always treasure.

I would also like to express my sincere appreciation to the members of the academic and conference organizing committees, including The Defense Committee of Prof. Esaki, Prof. Tsukada,

Prof. Maruta, Prof. Dinis, Prof. Sugiura, and Prof. Chiba, for their efforts in coordinating the evaluation and presentation of this work. I am equally grateful to the reviewers, editors, and involved in the revision process, including Prof. Tsukada, Prof. Maruta and Prof.Dinis, who dedicated their time and expertise to carefully reviewing this dissertation. Their constructive comments, insightful suggestions, and rigorous feedback played a crucial role in improving the quality, clarity, and technical depth of this work. The revision process guided by their feedback was instrumental in refining both the presentation and the contributions of this dissertation.

I am also grateful to the institutions and organizations that supported this research by providing access to computational resources, experimental platforms, and opportunities to present this work at conferences. These experiences broadened my perspective and helped refine the direction of this dissertation.

Finally, I would like to express my heartfelt gratitude to my family for their unconditional love and support. Their trust, patience, and encouragement have been the foundation enabling me to pursue long-term academic research, especially during the most demanding phases of this work.

To everyone who contributed in ways both seen and unseen, thank you. This dissertation is as much a reflection of your support as it is of my own efforts.

Dou Hu]

References

[1] A. Shahmansoori, G. E. Garcia, G. Destino, G. Seco-Granados, and H. Wymeersch, "Position and Orientation Estimation Through Millimeter-Wave MIMO in 5G Systems," *IEEE Transactions on Wireless Communications*, vol. 17, no. 3, pp. 1822–1835, 2018.

[2] C. Pan, G. Zhou, K. Zhi, S. Hong, T. Wu, Y. Pan, H. Ren, M. D. Renzo, A. Lee Swindlehurst, R. Zhang, and A. Y. Zhang, "An Overview of Signal Processing Techniques for RIS/IRS-Aided Wireless Systems," *IEEE Journal of Selected Topics in Signal Processing*, vol. 16, no. 5, pp. 883–917, August 2022.

[3] F. Liu, W. Yuan, C. Masouros, and J. Yuan, "Radar-Assisted Predictive Beamforming for Vehicular Links: Communication Served by Sensing," *IEEE Transactions on Wireless Communications*, vol. 19, no. 11, pp. 7704–7719, 2020.

[4] Z. Du, F. Liu, W. Yuan, C. Masouros, Z. Zhang, S. Xia, and G. Caire, "Integrated Sensing and Communications for V2I Networks: Dynamic Predictive Beamforming for Extended Vehicle Targets," *IEEE Transactions on Wireless Communications*, vol. 22, no. 6, pp. 3612–3627, 2023.

[5] D. Hu, J. Nakazato, J. Ehsan, K. Maruta, R. Dinis, and M. Tsukada, "DoA Estimation and Kalman Filter Based Multi-Antenna System for Vehicle Position in mmWave Network," *IEEE Open Journal of Vehicular Technology*, vol. 6, pp. 2761–2775, 2025.

[6] D. Hu, J. Nakazato, K. Maruta, R. Dinis, O. A. Aghda, and M. Tsukada, "OTFS Based RIS-Assisted Vehicle Positioning and Tracking in V2X Scenario," *IEEE Transactions on Communications*, pp. 1–1, 2025.

[7] D. Hu, J. Nakazato, K. Maruta, O. Abbassi, R. Dinis, and M. Tsukada, "A Low PAPR Page-Style Multi-User OTFS Modulation," in *2025 IEEE 101st Vehicular Technology Conference (VTC2025-Spring)*, 2025, pp. 1–6.

[8] D.-J. Yeom, S.-H. Park, J.-R. Kim, and M.-J. Lee, "Performance Analysis of Beamspace MUSIC with Beamforming Angle," in *2014 8th International Conference on Signal Processing and Communication Systems (ICSPCS)*, 2014, pp. 1–5.

[9] L. Hou, J. Wu, and W. Heng, "Millimeter-Wave Channel Estimation Based on 2-D Beamspace MODE Method," *IEEE Access*, vol. 12, pp. 12 478–12 487, 2024.

[10] V. Raghavan, J. Cezanne, S. Subramanian, A. Sampath, and O. Koymen, "Beamforming Tradeoffs for Initial UE Discovery in Millimeter-Wave MIMO Systems," *IEEE Journal of Selected Topics in Signal Processing*, vol. 10, no. 3, pp. 543–559, 2016.

[11] K. Goto, T. Akao, K. Maruta, and C.-J. Ahn, "Reduced Complexity Direction-of-Arrival Estimation for 2D Planar Massive Arrays: A Separation Approach," in *2018 18th International Symposium on Communications and Information Technologies (ISCIT)*, 2018, pp. 48–53.

[12] Z. Guo, X. Wang, and W. Heng, "Millimeter-Wave Channel Estimation Based on 2-D Beamspace MUSIC Method," *IEEE Transactions on Wireless Communications*, vol. 16, no. 8, pp. 5384–5394, 2017.

[13] H.-T. Sheng and W.-R. Wu, *IEEE Transactions on Wireless Communications, title=Blind AoA Estimation With Hybrid Antenna Arrays*, vol. 20, no. 8, pp. 5058–5070, 2021.

[14] R. W. Heath, N. Gonzlez, S. Rangan, W. Roh, and A. M. Sayeed, "An Overview of Signal Processing Techniques for Millimeter Wave MIMO Systems," *IEEE Journal of Selected Topics in Signal Processing*, vol. 10, no. 3, pp. 436–453, 2016.

[15] Z. Marzi, D. Ramasamy, and U. Madhow, "Compressive Channel Estimation and Tracking for Large Arrays in mm-Wave Picocells," *IEEE Journal of Selected Topics in Signal Processing*, vol. 10, no. 3, pp. 514–527, 2016.

[16] J. Talvitie, M. Valkama, G. Destino, and H. Wymeersch, "Novel Algorithms for High-Accuracy Joint Position and Orientation Estimation in 5G mmWave Systems," in *2017 IEEE Globecom Workshops (GC Wkshps)*, 2017, pp. 1–7.

[17] M. Koivisto, M. r. Costa, J. Werner, K. Heiska, J. Talvitie, K. Leppnen, V. Koivunen, and M. Valkama, "Joint Device Positioning and Clock Synchronization in 5G Ultra-Dense Networks," *IEEE Transactions on Wireless Communications*, vol. 16, no. 5, pp. 2866–2881, 2017.

[18] A. Shahmansoori, B. Uguen, G. Destino, G. Seco-Granados, and H. Wymeersch, "「tracking position and orientation through millimeter wave lens mimo in 5g systems」," *IEEE Signal Processing Letters*, vol. 26, no. 8, pp. 1222–1226, 2019.

[19] Y. Lu, M. Koivisto, J. Talvitie, M. Valkama, and E. S. Lohan, "Positioning-Aided 3D Beamforming for Enhanced Communications in mmWave Mobile Networks," *IEEE Access*, vol. 8, pp. 55 513–55 525, 2020.

[20] A. Guerra, F. Guidi, and D. Dardari, "Single-Anchor Localization and Orientation Performance Limits Using Massive Arrays: MIMO vs. Beamforming," *IEEE Transactions on*

Wireless Communications, vol. 17, no. 8, pp. 5241–5255, 2018.

[21] E. Rastorgueva-Foi, M. Costa, M. Koivisto, K. Leppnen, and M. Valkama, "Dynamic Beam Selection for Beam-RSRP Based Direction Finding in mmW 5G Networks," in *2018 International Conference on Indoor Positioning and Indoor Navigation (IPIN)*, 2018, pp. 1–6.

[22] S. Bhardwaj and D.-S. Kim, "Federated Learning-Based Joint Radar-Communication mmWave Beamtracking with Imperfect CSI for V2X Communications," in *2023 Fourteenth International Conference on Ubiquitous and Future Networks (ICUFN)*, 2023, pp. 201–206.

[23] W. Xu, F. Gao, X. Tao, J. Zhang, and A. Alkhateeb, "Computer Vision Aided mmWave Beam Alignment in V2X Communications," *IEEE Transactions on Wireless Communications*, vol. 22, no. 4, pp. 2699–2714, 2023.

[24] L. Yan, X. Fang, Y. Fang, L. Hao, Q. Xue, and C. Xu, "KF-LSTM Based Beam Tracking for UAV-Assisted mmWave HSR Wireless Networks," *IEEE Transactions on Vehicular Technology*, vol. 71, no. 10, pp. 10 796–10 807, 2022.

[25] Z. Du, F. Liu, W. Yuan, C. Masouros, Z. Zhang, S. Xia, and G. Caire, "Integrated Sensing and Communications for V2I Networks: Dynamic Predictive Beamforming for Extended Vehicle Targets," *IEEE Transactions on Wireless Communications*, vol. 22, no. 6, pp. 3612–3627, 2023.

[26] M. Hussain and N. Michelusi, "Learning and Adaptation for Millimeter-Wave Beam Tracking and Training: A Dual Timescale Variational Framework," *IEEE Journal on Selected Areas in Communications*, vol. 40, no. 1, pp. 37–53, 2022.

[27] Y. Sim, S. Sin, J. Cho, K. Kim, S. Moon, and I. Hwang, "Unscented Kalman Filter-based Beam Tracking in NR MIMO System using Hybrid Beamforming," in *2023 International Conference on Artificial Intelligence in Information and Communication (ICAIIC)*, 2023, pp. 650–653.

[28] D. Jang, H.-L. Song, Y.-C. Ko, and H. J. Kim, "Distributed Beam Tracking for Vehicular Communications via UAV-Assisted Cellular Network," *IEEE Transactions on Vehicular Technology*, vol. 72, no. 1, pp. 589–600, 2023.

[29] H.-L. Song and Y.-C. Ko, "Robust and Low Complexity Beam Tracking With Monopulse Signal for UAV Communications," *IEEE Transactions on Vehicular Technology*, vol. 70, no. 4, pp. 3505–3513, 2021.

[30] M. Koivisto, J. Talvitie, E. Rastorgueva-Foi, Y. Lu, and M. Valkama, "Channel Parameter Estimation and TX Positioning With Multi-Beam Fusion in 5G mmWave Networks," *IEEE Transactions on Wireless Communications*, vol. 21, no. 5, pp. 3192–3207, 2022.

[31] K.-H. Lin and K.-H. Liu, "A Novel Beam Alignment Scheme for Mobile Millimeter-Wave

Communications Based on Compressed Sensing Aided-Kalman Filter," *IEEE Open Journal of the Communications Society*, vol. 3, pp. 1515–1527, 2022.

[32] S.-H. Hyun, J. Song, K. Kim, J.-H. Lee, and S.-C. Kim, "Adaptive Beam Design for V2I Communications Using Vehicle Tracking With Extended Kalman Filter," *IEEE Transactions on Vehicular Technology*, vol. 71, no. 1, pp. 489–502, 2022.

[33] S. G. Larew and D. J. Love, "Adaptive Beam Tracking With the Unscented Kalman Filter for Millimeter Wave Communication," *IEEE Signal Processing Letters*, vol. 26, no. 11, pp. 1658–1662, 2019.

[34] P. Zhu, H. Lin, J. Bao, J. Li, and D. Wang, "Beam Tracking for Distributed Millimeter-Wave Massive MIMO Systems Based on the Unscented Kalman Filter," *IEEE Wireless Communications Letters*, vol. 11, no. 4, pp. 712–716, 2022.

[35] F. Liu, P. Zhao, and Z. Wang, "EKF-Based Beam Tracking for mmWave MIMO Systems," *IEEE Communications Letters*, vol. 23, no. 12, pp. 2390–2393, 2019.

[36] L. Chen, S. Zhou, and W. Wang, "MmWave Beam Tracking With Spatial Information Based on Extended Kalman Filter," *IEEE Wireless Communications Letters*, vol. 12, no. 4, pp. 615–619, 2023.

[37] S. Jayaprakasam, X. Ma, J. W. Choi, and S. Kim, "Robust Beam-Tracking for mmWave Mobile Communications," *IEEE Communications Letters*, vol. 21, no. 12, pp. 2654–2657, 2017.

[38] M. H. Dinan and A. Farhang, "RIS-Assisted OTFS Communications: Phase Configuration via Received Energy Maximization," April 2024. [Online]. Available: https://arxiv.org/abs/2404.07759

[39] V. S. Bhat, G. Harshavardhan, and A. Chockalingam, "Input-Output Relation and Performance of RIS-Aided OTFS With Fractional Delay-Doppler," *IEEE Communications Letters*, vol. 27, no. 1, pp. 337–341, October 2023.

[40] A. S. Bora, K. T. Phan, and Y. Hong, "IRS-Assisted High Mobility Communications Using OTFS Modulation," *IEEE Wireless Communications Letters*, vol. 12, no. 2, pp. 376–380, December 2023.

[41] M. Li, S. Zhang, Y. Ge, F. Gao, and P. Fan, "Joint Channel Estimation and Data Detection for Hybrid RIS Aided Millimeter Wave OTFS Systems," *IEEE Transactions on Communications*, vol. 70, no. 10, pp. 6832–6848, August 2022.

[42] C. Xu, L. Xiang, J. An, C. Dong, S. Sugiura, R. G. Maunder, L.-L. Yang, and L. Hanzo, "OTFS-Aided RIS-Assisted SAGIN Systems Outperform Their OFDM Counterparts in Doubly Selective High-Doppler Scenarios," *IEEE Internet of Things Journal*, vol. 10, no. 1, pp. 682–703, September 2023.

[43] M. H. Abid, I. A. Talin, and M. I. Kadir, "Reconfigurable Intelligent Surface-Aided Orthogonal Time Frequency Space and Its Deep Learning-Based Signal Detection," *IEEE Access*, vol. 11, pp. 47 321–47 338, May 2023.

[44] Z. Li, W. Yuan, B. Li, J. Wu, C. You, and F. Meng, "Reconfigurable-Intelligent-Surface-Aided OTFS: Transmission Scheme and Channel Estimation," *IEEE Internet of Things Journal*, vol. 10, no. 22, pp. 19 518–19 532, April 2023.

[45] M. H. Abid, I. A. Talin, and M. I. Kadir, "Wavelet-Aided OTFS for RIS-Assisted High-Mobility Wireless Channels," *IEEE Wireless Communications Letters*, vol. 13, no. 6, pp. 1611–1615, April 2024.

[46] Y. Zhao, Y. Feng, A. M. Ismail, Z. Wang, Y. L. Guan, Y. Guo, and C. Yuen, "2-Bit RIS Prototyping Enhancing Rapid-Response Space-Time Wavefront Manipulation for Wireless Communication: Experimental Studies," *IEEE Open Journal of the Communications Society*, vol. 5, pp. 4885–4901, August 2024.

[47] C. Ozturk, M. F. Keskin, H. Wymeersch, and S. Gezici, "RIS-Aided Near-Field Localization Under Phase-Dependent Amplitude Variations," *IEEE Transactions on Wireless Communications*, vol. 22, no. 8, pp. 5550–5566, January 2023.

[48] Y. Liu, S. Hong, C. Pan, Y. Wang, Y. Pan, and M. Chen, "Cramér-Rao Lower Bound Analysis of Multiple-RIS-Aided mmWave Positioning Systems," in *2022 IEEE 33rd Annual International Symposium on Personal, Indoor and Mobile Radio Communications (PIMRC)*, December 2022, pp. 1110–1115.

[49] A. Famili, T. O. Atalay, A. Stavrou, H. Wang, and J.-M. Park, "OFDRA: Optimal Femtocell Deployment for Accurate Indoor Positioning of RIS-Mounted AVs," *IEEE Journal on Selected Areas in Communications*, vol. 41, no. 12, pp. 3783–3798, October 2023.

[50] D.-R. Emenonye, H. S. Dhillon, and R. M. Buehrer, "RIS-Aided Localization Under Position and Orientation Offsets in the Near and Far Field," *IEEE Transactions on Wireless Communications*, vol. 22, no. 12, pp. 9327–9345, May 2023.

[51] P. Gao, L. Lian, and J. Yu, "Wireless Area Positioning in RIS-Assisted mmWave Systems: Joint Passive and Active Beamforming Design," *IEEE Signal Processing Letters*, vol. 29, pp. 1372–1376, June 2022.

[52] P. Zheng, H. Chen, T. Ballal, M. Valkama, H. Wymeersch, and T. Y. Al-Naffouri, "JrCUP: Joint RIS Calibration and User Positioning for 6G Wireless Systems," *IEEE Transactions on Wireless Communications*, vol. 23, no. 6, pp. 6683–6698, December 2024.

[53] F. Jiang, A. Abrardo, K. Keykhosravi, H. Wymeersch, D. Dardari, and M. Di Renzo, "Two-Timescale Transmission Design and RIS Optimization for Integrated Localization and Communications," *IEEE Transactions on Wireless Communications*, vol. 22, no. 12,

pp. 8587–8602, April 2023.

[54] Y. Zhao, X. Ma, Y. Liang Guan, Y. Liu, A. Mohamed Ismail, X. Liu, S. Yam Yeo, and C. Yuen, "Near-Orthogonal Overlay Communications in LoS Channel Enabled by Novel OAM Beams Without Central Energy Voids: An Experimental Study," *IEEE Internet of Things Journal*, vol. 11, no. 24, pp. 39 697–39 708, September 2024.

[55] Y. Zhao, Y. L. Guan, A. M. Ismail, G. Ju, D. Lin, Y. Lu, and C. Yuen, "Holographic-Inspired Meta-Surfaces Exploiting Vortex Beams for Low-Interference Multipair IoT Communications: From Theory to Prototype," *IEEE Internet of Things Journal*, vol. 11, no. 7, pp. 12 660–12 675, November 2024.

[56] X. Feng, Z. Zhao, Y. Zhao, Z. Zhao, L. Meng, and Y. L. Guan, "OFDM-Based Waveform Design for MIMO DFRC Systems With Reduced Range Sidelobes: A Majorization-Minimization Approach," *IEEE Transactions on Vehicular Technology*, vol. 74, no. 3, pp. 4582–4595, November 2025.

[57] R. Chong, S. Li, J. Yuan, and D. W. K. Ng, "Achievable Rate Upper-Bounds of Uplink Multiuser OTFS Transmissions," *IEEE Wireless Communications Letters*, vol. 11, no. 4, pp. 791–795, 2022.

[58] S. Shahani and N. K. Misra, "Enhanced Data Detection Scheme for Multi Antenna Signal in Wireless Communication Using OTFS Technique," in *2023 IEEE 4th Annual Flagship India Council International Subsections Conference (INDISCON)*, 2023, pp. 1–7.

[59] M. Sun, Q. Zhang, X. Xin, F. Chai, Y. Li, Y. Wang, Y. Zhao, F. Tian, Q. Tian, and Y. Wang, "Interference Cancellation and Iterative Multi-User Detection for Satellite OTFS-NOMA Networks," in *2024 22nd International Conference on Optical Communications and Networks (ICOCN)*, 2024, pp. 1–3.

[60] R. M. Augustine and A. Chockalingam, "Interleaved Time-Frequency Multiple Access Using OTFS Modulation," in *2019 IEEE 90th Vehicular Technology Conference (VTC2019-Fall)*, 2019, pp. 1–5.

[61] H. Zhang, K. Niu, J. Xu, J. Dai, and J. Zhang, "Iterative SIC-Based Multiuser Detection for Uplink Heterogeneous NOMA System," in *2022 IEEE Globecom Workshops (GC Wkshps)*, 2022, pp. 94–99.

[62] Q. Deng, Y. Ge, and Z. Ding, "Jamming Suppression via Resource Hopping in High-Mobility OTFS-SCMA Systems," *IEEE Wireless Communications Letters*, vol. 12, no. 12, pp. 2138–2142, 2023.

[63] S. Yang, H. Liu, Y. Zhou, Z. Ma, and P. Fan, "Joint Precoding Based on Interference Alignment and SVD for MU-MIMO OTFS With MRC Detector," *IEEE Wireless Communications Letters*, vol. 13, no. 10, pp. 2717–2721, 2024.

[64] Y. Ge, Q. Deng, P. C. Ching, and Z. Ding, "OTFS Signaling for Uplink NOMA of Heterogeneous Mobility Users," *IEEE Transactions on Communications*, vol. 69, no. 5, pp. 3147–3161, 2021.

[65] Y. Liu, M. Chen, C. Pan, T. Gong, J. Yuan, and J. Wang, "OTFS vs OFDM: Which is Superior in Multiuser LEO Satellite Communications," 2024. [Online]. Available: https://arxiv.org/abs/2403.02012

[66] Z. Ding, R. Schober, P. Fan, and H. Vincent Poor, "OTFS-NOMA: An Efficient Approach for Exploiting Heterogenous User Mobility Profiles," *IEEE Transactions on Communications*, vol. 67, no. 11, pp. 7950–7965, 2019.

[67] R. Chong, S. Li, W. Yuan, and J. Yuan, "Outage Analysis for OTFS-based Single User and Multi-User Transmissions," in *2022 IEEE International Conference on Communications Workshops (ICC Workshops)*, 2022, pp. 746–751.

[68] J. Feng, H. Q. Ngo, and M. Matthaiou, "Rectangular Pulse-Shaped OTFS with Fractional Delay and Doppler Shift for MU-MIMO Systems," in *2023 IEEE International Conference on Communications Workshops (ICC Workshops)*, 2023, pp. 788–793.

[69] A. Farhang and M. Bayat, "SC-FDMA as a Delay-Doppler Domain Modulation Technique," in *2024 IEEE International Conference on Communications Workshops (ICC Workshops)*, 2024, pp. 69–74.

[70] O. K. Rasheed, G. D. Surabhi, and A. Chockalingam, "Sparse Delay-Doppler Channel Estimation in Rapidly Time-Varying Channels for Multiuser OTFS on the Uplink," in *2020 IEEE 91st Vehicular Technology Conference (VTC2020-Spring)*, 2020, pp. 1–5.

[71] J. Zhao, G. Ren, and L. Sun, "Iterative PAPR Reduction Scheme with Optimized Phase Pre-Distortion Sequence for OTFS Systems," *IEEE Transactions on Green Communications and Networking*, pp. 1–1, 2025.

[72] Z. He, C. Qu, Y. Zuo, X. Yang, K. Xiong, and X. Ling, "Low-Complexity PAPR Reduction in DZT-OTFS System Through Clipping and Logarithmic Rooting Companding," *IEEE Communications Letters*, pp. 1–1, 2025.

[73] T. Ma, Y. Xu, X. Ou, H. Li, D. He, and W. Zhang, "Low-PAPR Pilot Arrangement and Iterative Channel Estimation for OTFS," *IEEE Transactions on Wireless Communications*, pp. 1–1, 2025.

[74] H. I. Hegazy, A. Mohamed, I. Al-Nahhal, and O. A. Dobre, "Low Complexity Super-Resolution OTFS-Assisted ISAC Framework for THz Communication," *IEEE Transactions on Vehicular Technology*, pp. 1–16, 2025.

[75] X. Liu, Y. Yuan, Z. Zhang, Z. Ma, W. P. Tay, and P. Fan, "Customized OTFS Pulse Compression and Waveform Optimization for Enhancing Target Sensing in ISAC Systems,"

IEEE Journal on Selected Areas in Communications, pp. 1–1, 2025.

[76] R. Al Ahsan, A. O. Fapojuwo, and F. M. Ghannouchi, "A New SS-VDS-SLM Technique for PAPR Reduction in High-Mobility Real-time OTSM," *IEEE Transactions on Vehicular Technology*, pp. 1–16, 2025.

[77] H. Paaso and M. Hirvonen, "Angular Resolution Improvement by Using Multi-Radar and FBSS MUSIC DoA Estimation Algorithm," in *2019 IEEE Intelligent Vehicles Symposium (IV)*, 2019, pp. 730–735.

[78] A. Liu, X. Zhang, J. Zhang, and Q. Yang, "Enhanced root-MUSIC for coherent signals with multi-resolution composite arrays," in *2019 IEEE Radar Conference (RadarConf)*, 2019, pp. 1–5.

[79] K. F. Masood, J. Tong, J. Xi, J. Yuan, and Y. Yu, "Inductive Matrix Completion and Root-MUSIC-Based Channel Estimation for Intelligent Reflecting Surface (IRS)-Aided Hybrid MIMO Systems," *IEEE Transactions on Wireless Communications*, vol. 22, no. 11, pp. 7917–7931, 2023.

[80] Q. Chen and X. Xie, "A Technique for Blind Identification of Uplink Signals in Multibeam Smart Antenna," in *2008 Fourth Advanced International Conference on Telecommunications*, 2008, pp. 341–345.

[81] S. Cha, S. Shin, J. Choi, and D. Yeom, "Signal processing techniques for improving angular resolution performance in homodyne FMCW radar," in *2016 International Conference on Control, Automation and Information Sciences (ICCAIS)*, 2016, pp. 1–6.

[82] H. Wang and K. R. Liu, "2-D spatial smoothing for multipath coherent signal separation," *IEEE Transactions on Aerospace and Electronic Systems*, vol. 34, no. 2, pp. 391–405, 1998.

[83] K. Kaneko and A. Sano, "Itetative AOA Estimation of Coherent Signals," in *TENCON 2007 - 2007 IEEE Region 10 Conference*, 2007, pp. 1–4.

[84] H. Yan and H. Fan, "Cyclostationarity based DOA estimation for wideband sources with a conjugate minimum-redundancy linear array," in *Proceedings. (ICASSP '05). IEEE International Conference on Acoustics, Speech, and Signal Processing, 2005.*, vol. 4, 2005, pp. iv/925–iv/928 Vol. 4.

[85] X. Dihua, C. Jianwen, and W. You, "A Novel Subspace Coherent Signal Processing Algorithm For High-Resolution DOA Estimation," in *2006 International Symposium on Intelligent Signal Processing and Communications*, 2006, pp. 653–656.

[86] J. Thompson, P. Grant, and B. Mulgrew, "Performance of spatial smoothing algorithms for correlated sources," *IEEE Transactions on Signal Processing*, vol. 44, no. 4, pp. 1040–1046, 1996.

[87] W. Li, X. Xu, X. Huang, and Y. Yang, "Direction-of-Arrival Estimation for Coherent Sig-

nals Exploiting Moving Coprime Array," *IEEE Signal Processing Letters*, vol. 30, pp. 304–308, 2023.

[88] Z. Liu, B. Ma, J. Liu, K. Yang, and Y. Wang, "Joint DOA-Range Estimation for Coherent Signals Exploiting Moving Time-Modulated Frequency Diverse Coprime Array," *IEEE Signal Processing Letters*, vol. 32, pp. 3186–3190, 2025.

[89] S. E. Sorkhabi and K. Rambabu, "Multi-Target DoA Estimation with mmWave MIMO Radar using Limited Number of Sensors," *IEEE Transactions on Vehicular Technology*, pp. 1–13, 2025.

[90] S. Ozawa, Y. Sasaki, J. Nakazato, and K. Maruta, "Broad-Range Null-Steering Incorporated with Beam Tracking for Millimeter-Wave V2X," in *2025 IEEE 22nd Consumer Communications & Networking Conference (CCNC)*, 2025, pp. 1–2.

[91] S. Sin, Y. Sim, J. Cho, K. Kim, S. Moon, and I. Hwang, "Unscented Kalman Filter-based Beam Tracking in NR MIMO System using Hybrid Beamforming," in *2023 Fourteenth International Conference on Ubiquitous and Future Networks (ICUFN)*, 2023, pp. 277–282.

[92] F. Guo, F. R. Yu, H. Zhang, X. Li, H. Ji, and V. C. M. Leung, "Enabling Massive IoT Toward 6G: A Comprehensive Survey," *IEEE Internet of Things Journal*, vol. 8, no. 15, pp. 11 891–11 915, March 2021.

[93] D. C. Nguyen, M. Ding, P. N. Pathirana, A. Seneviratne, J. Li, D. Niyato, O. Dobre, and H. V. Poor, "6G internet of things: A comprehensive survey," *IEEE Internet of Things Journal*, vol. 9, no. 1, pp. 359–383, August 2022.

[94] C. Xu, N. Ishikawa, R. Rajashekar, S. Sugiura, R. G. Maunder, Z. Wang, L.-L. Yang, and L. Hanzo, "Sixty Years of Coherent Versus Non-Coherent Tradeoffs and the Road From 5G to Wireless Futures," *IEEE Access*, vol. 7, pp. 178 246–178 299, December 2019.

[95] L. Zhao, C. Wang, K. Zhao, D. Tarchi, S. Wan, and N. Kumar, "INTERLINK: A Digital Twin-Assisted Storage Strategy for Satellite-Terrestrial Networks," *IEEE Transactions on Aerospace and Electronic Systems*, vol. 58, no. 5, pp. 3746–3759, April 2022.

[96] F. Liu, Y. Cui, C. Masouros, J. Xu, T. X. Han, Y. C. Eldar, and S. Buzzi, "Integrated Sensing and Communications: Toward Dual-Functional Wireless Networks for 6G and Beyond," *IEEE Journal on Selected Areas in Communications*, vol. 40, no. 6, pp. 1728–1767, March 2022.

[97] X. Meng, F. Liu, W. Yuan, and Q. Zhang, "Sensing Assisted Predictive Beamforming for V2I Networks: Tracking on the Complicated Road : (Invited Paper)," in *2022 IEEE 23rd International Workshop on Signal Processing Advances in Wireless Communication (SPAWC)*, July 2022, pp. 1–5.

[98] R. Hadani, S. Rakib, M. Tsatsanis, A. Monk, A. J. Goldsmith, A. F. Molisch, and R. Calderbank, "Orthogonal Time Frequency Space Modulation," in *2017 IEEE Wireless Communications and Networking Conference (WCNC)*, May 2017, pp. 1–6.

[99] R. J. Mailloux, *Phased array antenna handbook*. Artech house, 2017.

[100] J. Wang, S. Gong, Q. Wu, and S. Ma, "RIS-Aided MIMO Systems With Hardware Impairments: Robust Beamforming Design and Analysis," *IEEE Transactions on Wireless Communications*, vol. 22, no. 10, pp. 6914–6929, February 2023.

[101] Y. Hong, T. Thaj, and E. Viterbo, *Delay-Doppler Communications: Principles and Applications*. Academic Press, 2022.

[102] A. Thomas, K. Deka, S. Sharma, and N. Rajamohan, "IRS-Assisted OTFS System: Design and Analysis," *IEEE Transactions on Vehicular Technology*, vol. 72, no. 3, pp. 3345–3358, February 2023.

[103] K. Goto, T. Akao, K. Maruta, and C.-J. Ahn, "Reduced Complexity Direction-of-Arrival Estimation for 2D Planar Massive Arrays: A Separation Approach," in *2018 18th International Symposium on Communications and Information Technologies (ISCIT)*, December 2018, pp. 48–53.

[104] O. A. Aghda, M. J. Omidi, and H. Saeedi-Sourck, "Low-PAPR Joint Channel Estimation and Data Detection in ZP-OTFS System," *IEEE Transactions on Vehicular Technology*, pp. 1–5, July 2024.

[105] T. Thaj and E. Viterbo, "Low Complexity Iterative Rake Decision Feedback Equalizer for Zero-Padded OTFS Systems," *IEEE Transactions on Vehicular Technology*, vol. 69, no. 12, pp. 15 606–15 622, December 2020.

[106] D. Hu, J. Nakazato, K. Maruta, O. Abbassi, R. Dinis, and M. Tsukada, "A Low PAPR Page-Style Multi-User OTFS Modulation," in *2025 IEEE 101st Vehicular Technology Conference (VTC2025-Spring)*, 2025, pp. 1–6.

[107] O. A. Aghda, M. J. Omidi, and H. Saeedi-Sourck, "Low-PAPR Joint Channel Estimation and Data Detection in ZP-OTFS System," *IEEE Transactions on Vehicular Technology*, vol. 73, no. 12, pp. 19 821–19 825, 2024.